2013-01-31

Using the MDA-MB-231/EGFP-Luc2 breast cancer model to explore novel treatments for osteolytic metastases.

Aghaei, Mehrnoosh

UNIVERSITY OF CALGARY

Using the MDA-MB-231/EGFP-Luc2 breast cancer model to explore novel treatments for osteolytic metastases.

by

Mehrnoosh Aghaei

A THESIS

SUBMITTED TO THE FACULTY OF GRADUATE STUDIES

IN PARTIAL FULFILMENT OF THE REQUIREMENTS FOR THE

DEGREE OF MASTERS OF SCIENCE

DEPARTMENT OF MEDICAL SCIENCE

CALGARY, ALBERTA

January 2013

Abstract

The ability to recruit and expand new blood vessels is an essential component of tumour growth. Hence, the main goal of this study was to determine whether we could prevent the growth of bone metastases by blocking angiogenesis via the use of the vascular disrupting agent (VDA), DMXAA, either alone, or used in combination with the pan-PI3K inhibitor, GDC-0941. DMXAA, an agent of the flavonoid class, has been shown to disrupt the tumour vasculature in a number of model systems by selectively inducing apoptosis in tumour vascular endothelial cells. Since the PI3K/Akt pathway has been shown to increase cell survival, growth, and proliferation, we hypothesized that by inhibiting a major anti-apoptotic mechanism, a PI3K inhibitor, we would be able to increase the anti-vascular effects of a VDA within bone metastasis xenografts. Contrary to what we expected, DMXAA, either alone or in combination with GDC-0941, had no statistically significant on bioluminescence of established metastases while bioluminescence of subcutaneous tumours was severely affected. Our studies provide a possible explanation for the failure of DMXAA in human clinical trials.

Acknowledgements

My MSc studies would have not gone far without the invaluable support from a number of individuals who I am very grateful for.

Most importantly, I would like to thank and acknowledge my supervisor Dr. Frank Jirik for giving me opportunity to do research. I am very grateful for all of his support, guidance, and encouragements. I have gained enormous amount of valuable information from him and I will always have a great respect for him. His geniuses mind and passion for science has always been inspiring and admirable.

I would like to thank my committee members Dr. Steve Boyd and Dr. Shirin Bonni. I am very grateful for their supervision, kindness, and support. I will always appreciate their time and helpfulness.

I am very appreciative for having a great support from all of the the Jirik lab's member. They have been very kind and supportive throughout the years I was in the lab. I would like to send a special thanks to Jennifer Hahn who has been there for me as a wonderful friend and an amazing guide throughout my master's program. I really respect her work ethics and happy to had the privilege to work alongside her. I would like to thank Michelle Villemaire for her helpfulness, support, and friendship that help me to get through some of the challenging days in my maters. I also like to thank Dr. Gary Martin and Charlene Downey for their advice and help throughout my experiments. They are

both an outstanding scientists and I really respect the amount of information and knowledge they have.

I would like to thank Molly from Biohazard Facility University of Calgary Animal Research Center for providing care to my experimental mice.

My deepest appreciation and gratefulness goes to my parents, Mehrandokht Koravand and Nasrollah Aghaei, my brother, Amir Aghaei, and nephew, Ariya Kawamura,for giving me their unconditional love and support. I am thankful for my parents sacrifice to immigrate to Canada so I could have a better education and life. Thanks to all my special friends Ryan, Andrea, and Mira for encouraging me and believing in me. My family and friends have always been there for me to cheer me up when I needed some lifting up.

Dedication

This thesis is dedicated to my family and friends who have given me a great support, love and encouragement along the way. With special thanks to my wonderful parents Mehrandokht Koravand and Nasrollah Aghaei.

Table of Contents

List of Figures and Illustrations

List of Symbols, Abbreviations and Nomenclature

Symbol	Definition
ER	Estrogen receptor
PR	Progesterone receptor
HER2/neu	Human epidermal growth factor receptor 2
RANKL	Receptor activator of NFº B ligand
M-CSF	Macrophage colony-stimulating factor
OPG	Osteoprotegerin
PTHrP	Parathyroid hormone-related protein
IL	Interleukins
TGF-²	Transforming growth factor-²
IGF1	Insulin-like growth factor 1
MAPK	Mitogen-activated protein kinases
PI3K	Phosphatidylinositol 3-kinases
NFº B	Nuclear factor kappa-light-chain-enhancer of activated B
TRAF 6	Tumour necrosis factor receptor-associated cytoplasmic factor 6
EGFR	Epidermal growth factor receptor
IGF-1R	Insulin-like growth factor (IGF)-1 receptor
VEGF	Vascular endothelial growth factor
PIP3	Phosphatidylinositol-3,4,5-trisphosphate
FGFs	Fibroblast growth factors
PDGF	Platelet-derived growth factor
EGF	Epidermal growth factor
VDA	Vascular disrupting agent
ASA404	5,6-dimethylxanthenone-4-acetic acid
NSCLC	Non-small cell lung cancer
CP	Cyclophosphamide
TNF-±	Tumour necrosis factor-±
EGFP	Enhanced green fluorescent protein
Luc2	Luciferase-2
CMV	Cytomegalovirus
FACS	Fluorescence-activated cell sorting
DMEM	Dulbecco’s modified Eagle’s medium
FBS	Fetal bovine serum
PTEN	Phosphatase and tensin homolog
ATCC	American Type Culture Collection
IC	Intracardiac
i.p.	Intraperitoneal
BLI	Bioluminescence imaging
NBF	Neutral buffered formalin
PFA	

	Paraformaldehyde
µCT	Micro-computed tomography
ROI	Region of interest
PVDF	Polyvinylidene difluoride
HRP	Horseradish peroxidase
DMSO	Dimethyl sulfoxide
EDTA	Ethylenediaminetetraacetic acid
PTEN	Phosphatase and tensin homolog
T	Tumour area
N	Necrosis
H	Hemorrhage
GP	Growth plate
TB	Trabecular bone
CB	Cortical bone
mTOR	Mammalian target of rapamycin
mTORC2	Mammalian target of rapamycin complex 2
DAMPs	Damage associated molecular pattern molecules
HMGB1	High mobility group protein B1
TLR4	Toll-like receptor 4
Iba1	Ionized calcium binding adaptor molecule 1
M	Macrophages
NO	Nitric oxide
iNOS	Inducible nitric oxide synthase
PCR	Polymerase chain reaction

Epigraph

The larger the island of knowledge, the longer the shoreline of wonder.

Ralph W.Sockman

Chapter One: Introduction

1.1 Breast cancer

Breast cancer is one of the most common malignancies and a leading cause of cancer death among woman. Worldwide, breast cancer is one of the most frequently diagnosed cancers in the female population and accounts for about 23% of total cancer cases [1]. Breast cancer is an adenocarcinoma, a cancer originating in glandular tissues, which can occur primarily in two forms: (1) ductal or (2) lobular carcinoma; depending if malignancy develops in breast ducts or lobules, respectively [2]. Although breast cancer is often referred to as a single disease, there are various types of breast cancer based on molecular and genomic factors [3]. Biomarkers are used to categorize breast cancer into different sub-types, and include the presence or absence of proteins such as the estrogen receptor (ER), progesterone receptor (PR), and human epidermal growth factor receptor 2 (HER2/neu). These receptors control a variety of cell functions, such as cell growth and survival [4]. The four most studied breast cancer molecular subtype include luminal A, luminal B, triple negative/basal-like and HER2 type [5, 6]. Luminal A tumours tend to be HER2-/ ER+ and/or PR+, luminal B tumours tend to be HER2+/ ER+ and/or PR+, triple negative tumours tend to be HER2-/ER-/PR-, and HER2 type tumours tend to be ER-/PR- [7-9]. The differences in gene expression are reflected in differences in tumour cell biology and clinical outcomes [10]. There are various effective treatments available for hormone-receptor-positive or HER2/neu-positive tumours since the presence of receptors provide targets for treatment. However, about 10-15% of breast cancers are of the triple negative sub-type that do not express ER, PR, or HER2/neu receptors [11-13]. Triple

negative breast cancer tends to be the most aggressive type of breast cancer. This sub-type of breast cancer is more likely to metastasize and hence carries a poorer prognosis as compared to the hormone receptor-positive breast cancer sub-types [12]. More research is required to identify ways to target the triple negative subtype of breast cancer.

1.1.1 MDA-MB-231 breast cancer cell line

MDA-MB-231 is a triple negative breast cancer cell line derived from a malignant pleural effusion [11]. When introduced into mice this line is very invasive and aggressive as compared to most breast cancer cell lines such as estrogen receptor-positive breast cancer cells [12, 14]. MDA-MB-231 cells tend to grow rapidly and when injected into animals and have a propensity for metastasis. This cell line frequently metastasizes to bone, making it an important preclinical model system for studying the prevention and treatment of bone metastases [14].

1.2 Bone metastases

Approximately 50% to 70% of patients with advanced breast cancer develop bone metastases [15], and these are commonly osteolytic [16]. Studies have also shown that there is a significant decrease in the 5 year survival rate (as low as a 20%) in breast cancer patients with bone metastases [17]. In addition, the complications arising from bone metastases can also lead to a decrease in the patient's quality of life. Patients with bone metastases often have an increase in bone fragility due to sclerotic and/or lytic lesions that can lead to: severe bone pain, pathological fractures, hypercalcemia, and

spinal cord compression [18, 19]. This disease can present in variety of way, ranging from asymptomatic fractures to disabling long bone fractures that is very difficult to treat. Spinal compression due to vertebral collapse remains the most devastating complication of bone metastases [19]. Treatment for the bone metastases includes supportive care with analgesics, radiotherapy, surgery for fractures, and bone-targeting drugs such as bisphosphonates and denosumab [19]. Bisphosphonates have a long establish role in treatment of bone metastases due to their ability to inhibit osteoclast activity that consequently leads to a reduction in bone resorption and an alteration the bone microenvironment rendering it less supportive for tumour growth. Zoledronic acid, disodium pamidronate, ibandronic acid and sodium clodronate are four types of bisphosphonates currently being used in clinical settings. Zoledronic acid's acitivity is broad and is therefore used for all type of malignancies, while disodium pamidronate and sodium clodronate are mainly used for breast cancer and multiple myeloma. Ibandronic acid is specific for and used in breast cancer cases only [20]. There are also more recent biological drugs currently used that are being used as a prevention drugs for bone metastases such as denosumab, a human monoclonal antibody that inhibits RANKL [20]. However, there remains a great need for improvements in the treatment and prevention of bone metastases. One of the main goals of this study was to determine whether we could prevent and/or reduce osteolysis by interfering with osteoclast activation and differentiation, as well as by targeting the tumour vasculature.

1.3 Osteoclast biology

Since osteoclasts are one of the main players in osteolytic metastases it is important to understand their biology and role in the tumour microenvironment. Osteoclasts are bone cells that play a key role in bone resorption. Bone resorption is a natural event as our skeleton is constantly undergoing remodeling. Even in adulthood it is estimated that 10% of bone is renewed each year [21]. However, there is a balance in bone remodelling between the activities of osteoclasts and osteoblast. In the presence of metastatic breast cancer cells, however, bone destruction is considerably accelerated, with and osteoclasts being largely responsible for the generation of osteolytic metastatic lesions [22].

1.3.1 Osteoclast differentiation, activation and regulation

Osteoclasts are derived from precursor cells in the monocyte-macrophage lineage. Upon multiple interactions with osteoblasts or their stromal cell precursors, the earliest precursor, granulocyte-macrophage colony-forming units will commit and differentiate to large multinucleated osteoclasts [23]. Osteoblasts and/or their stromal cell precursors express two key osteoclastogenic cytokines; receptor activator of nuclear factor kappa-light-chain-enhancer of activated B cells (NFº B) ligand (RANKL), and macrophage colony-stimulating factor (M-CSF). Osteoclast differentiation is thus largely dependent upon direct binding of these osteoblast membrane bound cytokines to their cognate receptors located on osteoclast precursor's surface [24, 25]. Once the multinuclear osteoclasts are activated, they bind to the bone matrix via integrins and secrete acid and enzymes, principally cathepsin K, that degrade the bone matrix (Fig 1.2.1-1) [3].

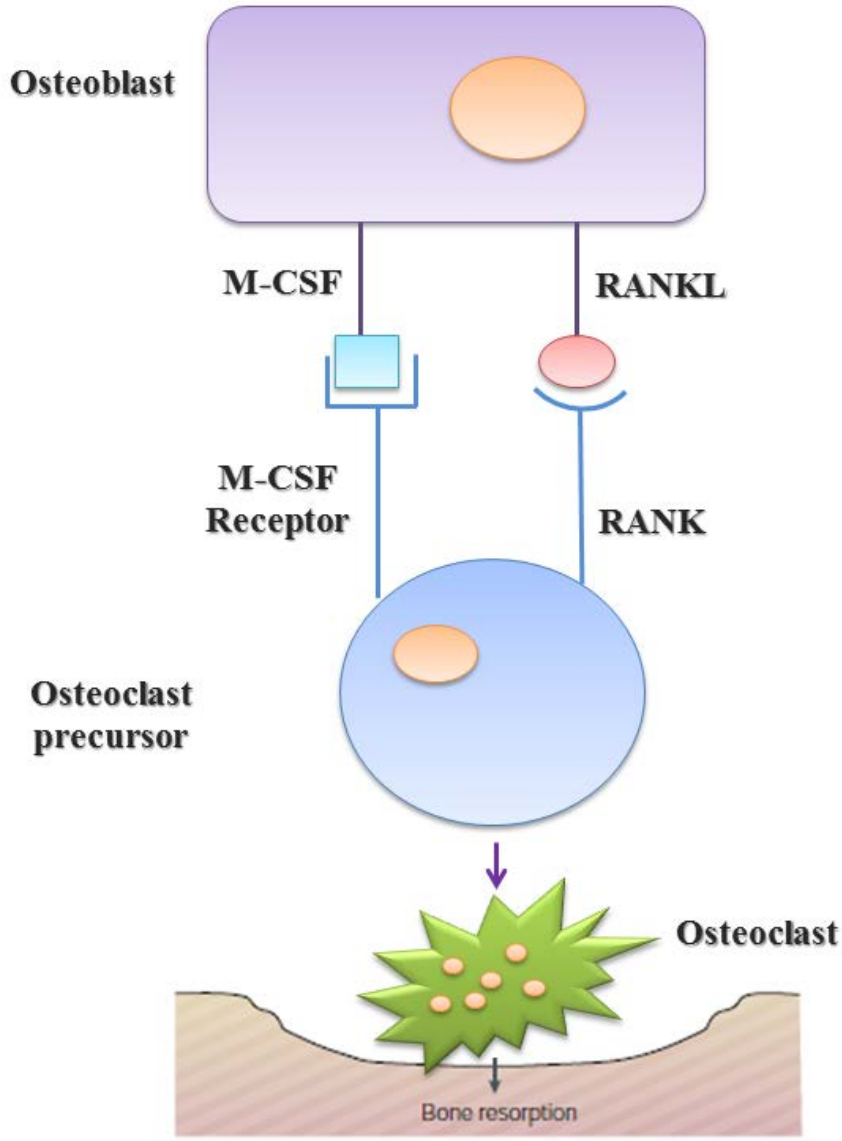

Figure 1.2.1-1 Osteoclasts differentation.

Osteoblasts express two key osteoclastogenic cytokines, RANKL and M-CSF, that bind to receptors expressed on the osteoclast thus initiating osteoclast differentiation and activation. Activated osteoclasts bind to the bone matrix via integrin proteins and secrete acid and lysosomal enzymes to cause bone resorption.

Osteoblasts can also negatively regulate osteoclast activity by producing osteoprotegerin (OPG). This factor acts to antagonize osteoclastogenesis. OPG competes as a receptor with the RANK receptor and binds to RANKL. This inhibits the binding of RANKL to the RANK receptor, thus, preventing RANK stimulation of osteoclasts [26].

1.3.2 The vicious cycle

Osteolysis is caused by tumour cell stimulation of osteoclast proliferation, differentiation, and activity rather than by the direct effect of cancer cells on the bone [27]. Thus, in the tumour microenvironment, tumour cells and stromal cells work together to promote bone destruction and tumour growth. Once the tumour cells find their way to the bone and start growing, they release factors such as parathyroid hormone-related protein (PTHrP), interleukins (IL)-1, IL-6, IL-11 and IL-18 that cause the recruitment and activation of osteoblasts and osteoclasts [18]. PTHrP, one of the main factors activating osteoblasts to produce RANKL, also down-regulates OPG, a negative regulator of the RANK signalling pathway. Release of RANKL from osteoblasts then activates osteoclast precursors as was explained in section 1.2.1. As activated osteoclasts are involved in bone resorption, this process leads to the release of latent transforming growth factor-^{2} (TGF-^{2}) and insulin-like growth factor 1 (IGF1) from the bone matrix. These growth factors, released during bone resorption, then stimulate cancer cell proliferation and promote the production of

PTHrP, resulting in a positive feedback loop also known as the “vicious cycle” (Fig 1.2.2-1) [18].

1.3.3 Osteoclast signalling pathways

A variety of signalling pathways, including moelcules such as the mitogen-activated protein kinases (MAPK), phosphatidylinositol 3-kinases (PI3K), and NFº B that are activated as a consequence of RANK and M-CSF receptor activation. As mentioned before, these pathways are mainly involved in osteoclast differentiation, proliferation, and survival. Upon binding of RANKL to the RANK receptor, tumour necrosis factor receptor-associated cytoplasmic factor 6 (TRAF 6) is recruited and binds to the cytoplasmic domain of the RANK receptor. Binding of TRAF 6 is the initial step in RANK signalling. TRAF 6 acts as an adaptor to assemble signalling proteins that initiate the MAPK signalling pathway (involved in osteoclast differentiation) and the NFº B signalling pathway (involved in osteoclast differentiation and survival) [28]. TRAF 6 also initiates PI3K signalling, a key signalling pathway involved in osteoclast migration and survival. Stromal cell-derived M-CSF is a second key growth factor involved in osteoclast proliferation and survival. Critical pathways downstream of the M-CSF receptor include the PI3K/Akt pathway, as well the MAP kinase signalling pathway (Fig 1.2.3-1) [4,7].

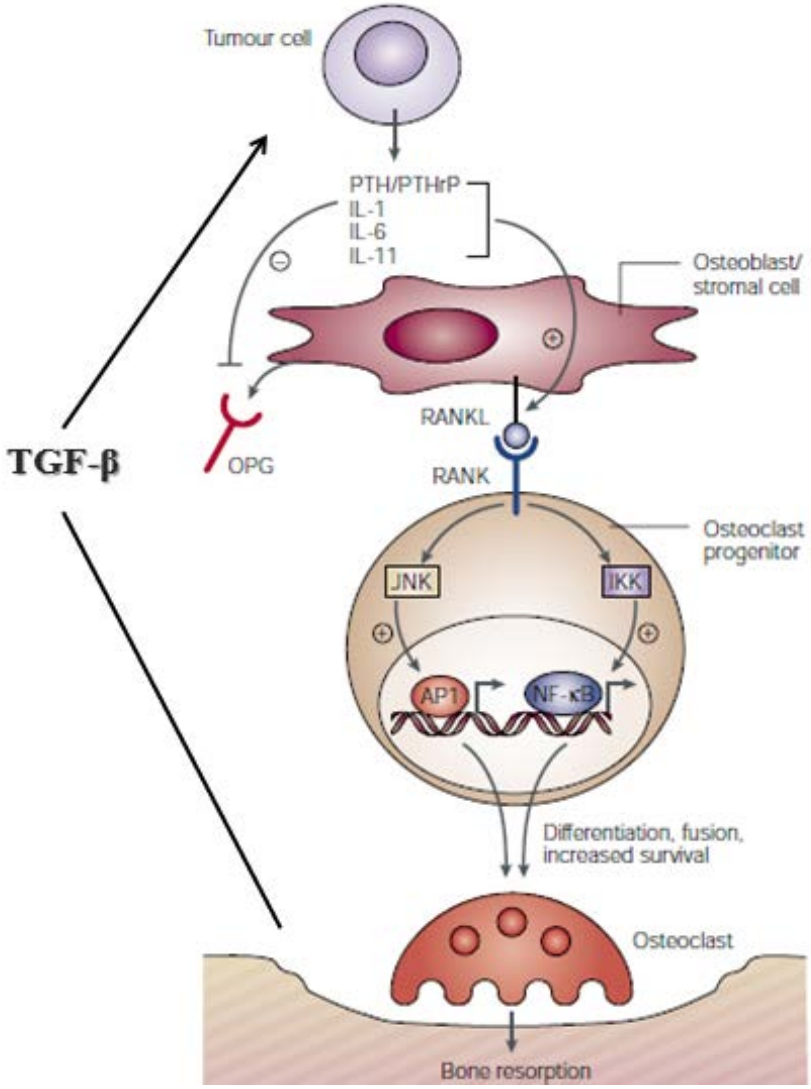

Figure 1.2.2-1 The vicious cycle.

Osteolysis is caused by tumour stimulation of osteoblast and osteoclast activity which then stimulate further tumour growth. This continuous circular stimulation is known as the “vicious cycle”. Once the tumour cells find their way to the bone and start growing, they release factors such as parathyroid hormone-related protein (PTHrP). PTHrP activates osteoblasts to produce RANKL and down-regulates OPG, a negative regulator of RANK signalling. Release RANKL from osteoblasts will activate osteoclasts precursors. Bone resorption causes release of latent factors from the bone matrix, thus stimulating cancer cell proliferation. This figure was printed from (Mundy GR, 2002), with permission from Nature Review Cancer.

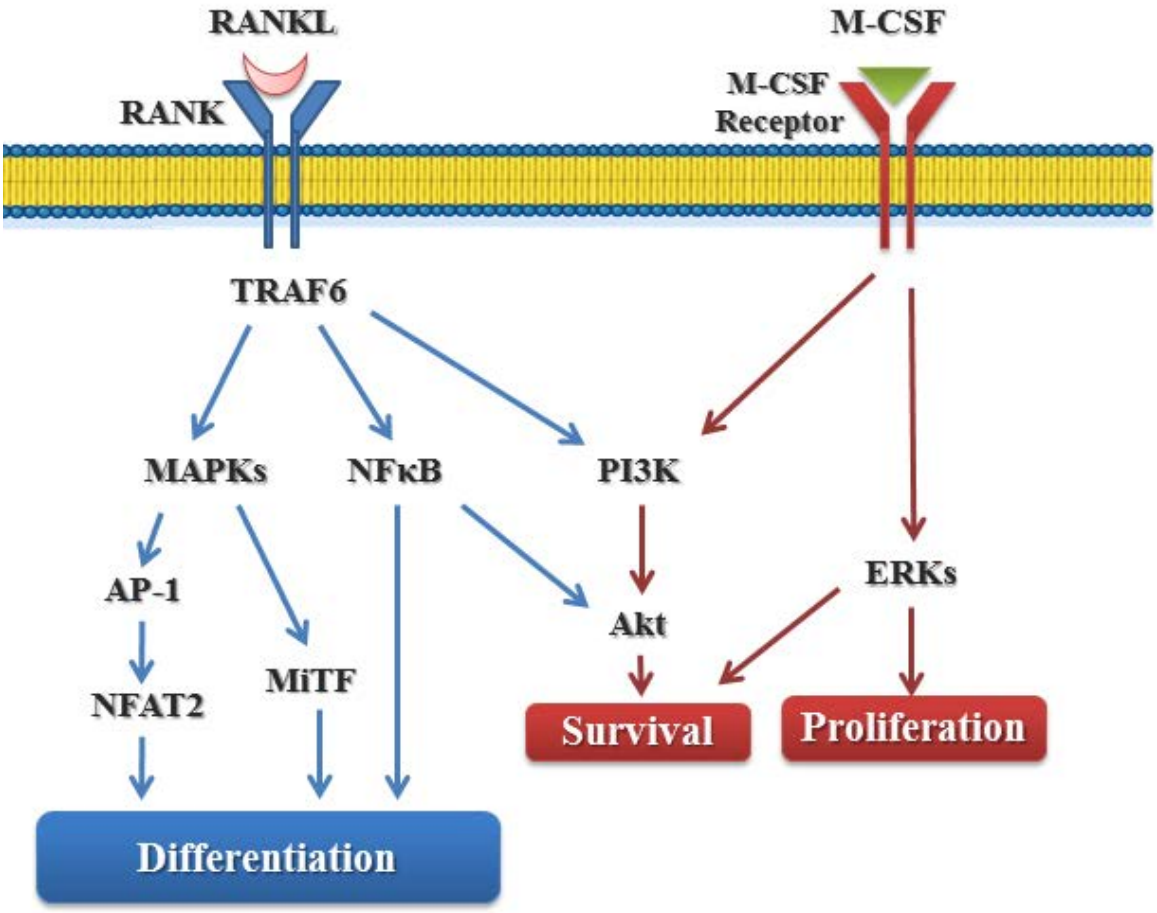

Figure 1.2.3-1 Major signalling pathway activated via osteoclasts' RANK and M-CSF receptors.

Upon binding of RANKL to the RANK, tumor necrosis factor receptor-associated cytoplasmic factor 6 (TRAF 6) is recruited and binds to the cytoplasmic domain of RANK. TRAF 6 acts as an adaptor to assemble signalling proteins that initiates several signalling pathways involved in osteoclast differentiation and survival. M-CSF is second cytokine that is involved in osteoclasts proliferation and survival.

1.3.4 Phosphoinositide 3-kinase (PI3K) pathway

As already mentioned one of the critical signaling pathways activated downstream of both RANK and M-CSF receptors in osteoclasts is the PI3K/Akt signalling pathway [4]. A wide variety of other ligand-triggered receptors have been identified to activate the PI3K signalling cascade, including epidermal growth factor receptor (EGFR), other members of the human EGFR (HER) family, insulin-like growth factor (IGF)-1 receptor (IGF-1R), vascular endothelial growth factor (VEGF), and platelet derived growth factor; interleukins, cytokines, and ligands for G-protein coupled receptors [29-32]. The PI3K/Akt pathway contributes mainly in enhancing cell survival, metabolism, proliferation, and growth [33, 34]. Activation of PI3K is a common event in human cancer including osteolytic metastases, thus, targeting this kinase was one focus of our study [35]. Although the PI3K have been grouped into three classes (I-III) in this study our focus is on class I PI3Ks. Class I PI3Ks are further subdivided into two subfamilies, depending on the receptor to which they are coupled. Class IA PI3Ks are heterodimers composed of an adaptor/regulatory subunit (p85α, P85β, or p55[3]) and a p110 catalytic subunit (p110α, p110β, p110δ or p110 [3]). The adaptors act to localize PI3K to the plasma membrane via the interaction of their SH2 domains with phosphotyrosine residues on activated receptors. The p110 catalytic subunit generates the secondary messenger phosphatidylinositol-3,4,5-trisphosphate (PIP3) which goes on via subsequent step to activate Akt-mediated signalling (Fig 1.2.5-1) [36].

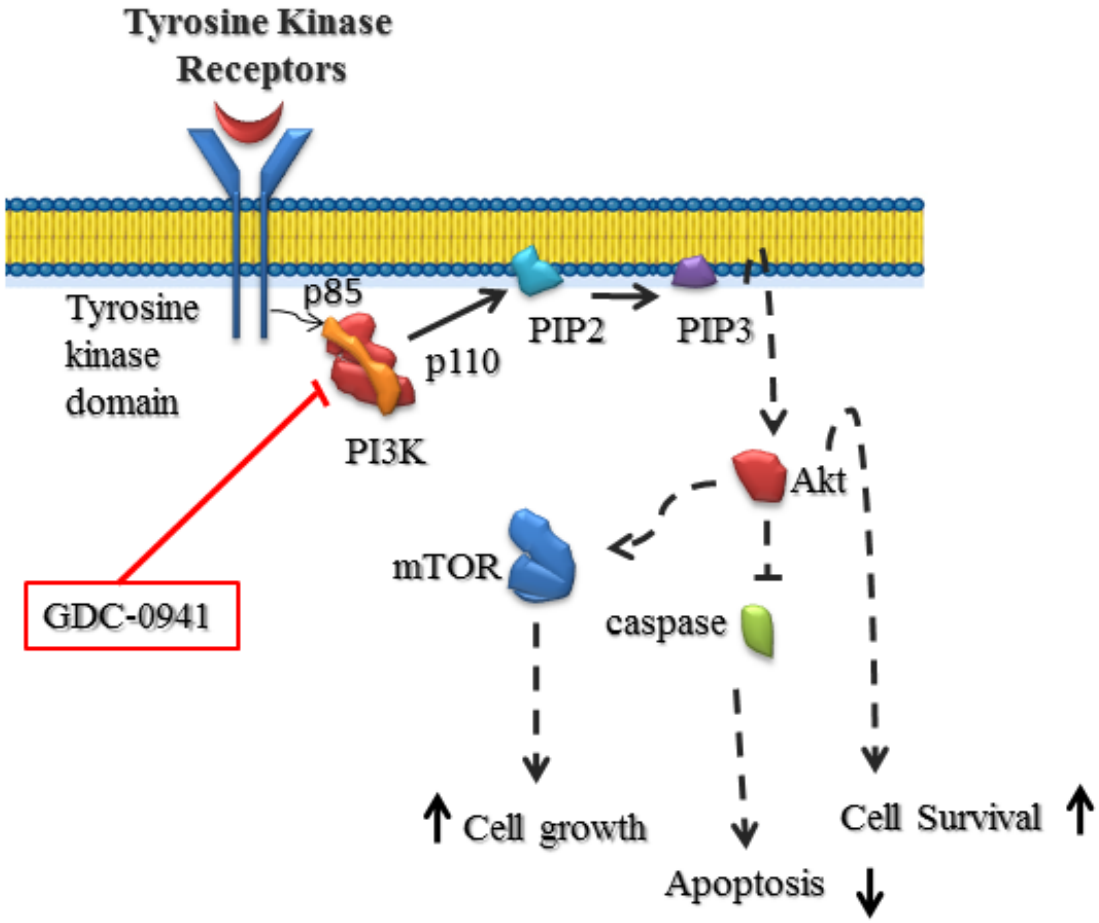

Figure 1.2.5-1 PI3K signalling pathway.

A number of tyrosine kinases receptor and growth factors including EGFR, other members of the human EGFR (HER) family, RANK, M-CSF receptor, IGF receptor (IGF-1R), VEGF, and platelet derived growth factor have been identified that activate the PI3K signalling cascade. This anti-apoptotic signalling pathway contributes mainly in enhancing cell survival, metabolism, proliferation, and growth. Pan-PI3K inhibitors such as GDC-0941 target PI3K/Akt signalling pathway. GDC-0941 binds to the PI3K catalytic subunit in an ATP-competitive manner and inhibits production of secondary messenger PIP3 necessary for activation of the PI3K/Akt signalling pathway.

1.3.5 Pan-PI3K inhibitor, GDC-0941

In our study we used the Pan-PI3K inhibitor, GDC-0941, to target the PI3K/Akt pathway. This drug is currently in phase II of non-small cell lung cancer and breast cancer (clinicaltrails.gov.ca). GDC-0941 targets the ±, ², and ´ isoforms of the p110 catalytic subunit of class IA PI3Ks [37]. This drug selectively binds to the PI3K catalytic subunit in an ATP-competitive manner, thereby inhibiting the production of the secondary messenger, PIP3, and activation of the PI3K/Akt signalling pathway (Fig 1.2.5-1) [37]. The purpose of using this inhibitor was to inhibit PI3K/Akt signalling in osteoclasts and hopefully halting the vicious cycle of metastasis-induced osteolysis. Also inhibition of the PI3K/Akt pathway, a major anti-apoptotic mechanism, might decrease endothelial cell survival, thus enhancing the effect of a vascular disrupting agent that we also evaluated for its effect on MDA-MB-231 tumours.

1.4 Angiogenesis

Angiogenesis is a physiological process that involves the formation of new vasculature from pre-existing blood vessels. This phenomenon is both normal and vital for growth and development as well as for wound healing. However, angiogenesis is also a fundamental step for the transition of a latent tumour state to a malignant one [38].

1.4.1 Tumour angiogenesis

The ability to recruit and expand new blood vessels is an essential component of tumour growth [39]. Thus, in the next part of our study we targeted the tumour vasculature as a second method to halt the growth of osteolytic metastases. Most tumours require the initiation of angiogenesis to sustain tumour growth, survival and metastasis. In normal tissue there is a fine equilibrium between pro-angiogenic factors such as vascular endothelial growth factor (VEGF), fibroblast growth factors (FGFs), platelet-derived growth factor (PDGF), epidermal growth factor (EGF), and anti-angiogenic factors and proteins such as angiostatin, endostatin, tumstatin and thrombospondin-1 that maintain normal blood vessel growth (Fig 1.4.1-1) [40-42]. However, in the tumour, the disruption of the delicate balance between pro-angiogenic and anti-angiogenic factors, creates and sustains a growing vascular network with different characteristics from the normal vasculature. For example, the tumour vasculature inhibits a disorganized structure, increased vascular permeability and intermittent blood flow compared to the normal vasculature [41]. Also, increased tumour vascular permeability and intermittent blood flow creates high interstitial fluid pressure within the tumour which acts as a barrier for drug and oxygen delivery [43].

1.4.2 Potential therapies to target tumour vasculature

Because the growth and survival of tumours is crucially dependent on a functioning blood supply, strategies that specifically target the vasculature to deprive tumours of vital nutrients provide an attractive approach for cancer therapy [44]. Currently, there are two strategic approaches to target the tumour blood vasculature: (1) an anti-angiogenic

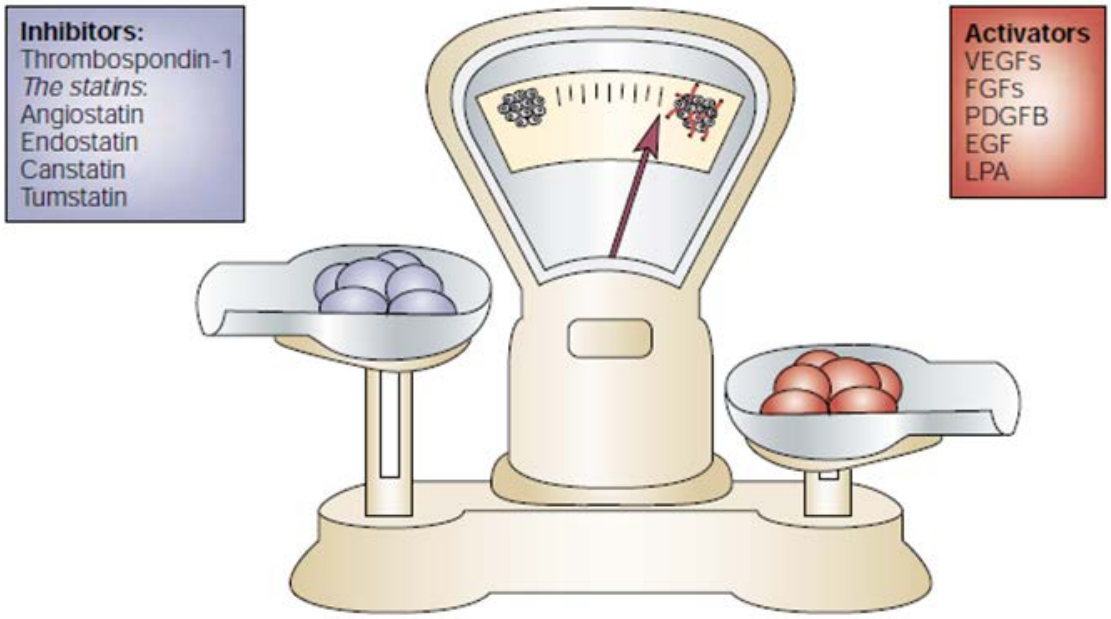

Figure 1.4.1-1 The angiogeneic equlibrium balance.

This images shows the disruption of the delicate balance between pro-angiogenic and anti-angiogenic factors that occur in presence of tumour. In normal tissue there is a fine equilibrium between pro-angiogenic factors such as VEGF, FGFs, PDGFB, EGF and LAP and anti-angiogenic factors and proteins such as angiostatin, endostain, tumstatin and thrombospondin-1 that maintain normal blood vessel growth. However, in the presence of tumor this equilibrium will shift toward pro-angiogenic factor and favour formation of a growing vascular network that are necessary for tumour survival. This figure was printed from (Bergers G and Benjamin LE, 2003), with permission from Nature Review Cancer.

approach using targets such as anti-VEGF and anti-VEGF receptor 2 monoclonal antibodies which act mainly to prevent angiogenesis, and (2) vascular disrupting agents that target endothelial cells [45-48].

1.4.2.1 Anti-angiogenic approach

While numerous pro-angiogenic factors involved in tumour angiogenesis have been characterized, VEGF has been identified as the predominant regulator of tumour angiogenesis [49]. The VEGF ligand is the only angiogenic factor known to be present at all stages of tumour development [50]. There are several important cellular signalling pathways that VEGF triggers in endothelial cells. VEGF binding to VEGF receptors lead to receptors dimerization and activation of various signalling cascades required for angiogenesis, including the PI3K/Akt pathway, which leads to endothelial cell survival; the p38 MAPK pathway, which promotes endothelial cell migration; and the Ras/Raf pathway, which induces endothelial cell proliferation [47, 51]. All these pathways are involved in promoting angiogenesis. An understanding the VEGF mechanism led to the development of anti-angiogenic approaches to target the tumour vasculature. This approach has made use of various inhibitors in hopes of preventing angiogenesis and thereby halting tumour growth, such as Bevacizumab (a humanized monoclonal antibody against VEGF-A), DC101 (a monoclonal antibody against VEGF receptor-2), and TSU68 (an anti-angiogenic receptor tyrosine kinase inhibitor that targets multiple receptors: VEGFR2, PDGFR, and FGFR) [45-48, 52]. It is believed that anti-VEGF or anti-

VEGFR inhibitors target VEGF signalling pathways and prevent the formation of new blood vessels which are necessary for tumour growth and metastases.

1.4.2.2 Vascular disrupting approach

The vascular disrupting approach represents a completely different method of targeting the tumour vasculature. Vascular disrupting agents (VDAs) supress tumour growth through the induction of a vasculature collapse which then leads to the development of hypoxia and eventually tumour necrosis [53]. Small molecule VDAs are sub-divided into two groups: synthetic flavonoids and tubulin-binding agents [54]. Synthetic flavonoids work by activating local cytokine production [48]. An example of a synthetic flavonoid is 5,6-dimethylxanthenone-4-acetic acid [DMXAA] also known as ASA [54]. Tubulin-binding VDAs, in contrast, mainly bind to the colchicine binding site of the ^{2}-tubulin monomer and cause tubulin destabilization within proliferating endothelial cells in the tumour vessels, as result of a rapid depolymerization of microtubules [55]. ABT-75 and NPI-2358 are examples of tubulin-binding VDAs that are being used in clinical trials [56, 57].

In our study we used the vascular disrupting agent, DMXAA, to determine whether we were able to prevent the growth of bone metastases.

1.4.3 Vascular disrupting agent, DMXAA

DMXAA is the most advanced vascular disrupting agent (VDA) in clinical trials. Currently this drug is in phase III clinical trials for non-small cell lung cancer (NSCLC)

[53, 58]. This agent showed promising effects in preclinical rodent tumour studies where it led to induction of hemorrhagic necrosis and growth delay [59, 60]. DMXAA was also shown to enhance tumour death by 10 to 500-fold when given in combination with chemotherapeutic drugs such as cisplatin or cyclophosphamide (CP), as compared to chemotherapy alone [61].

1.4.3.1 DMXAA mechanism of action

DMXAA has a dual mechanism of action against the tumour vasculature; both direct and indirect [62]. In the direct mechanism, DMXAA disrupts the tumour vessels by selectively inducing apoptosis of endothelial cells. It does this by targetting the distinctive properties of unstable vessels present in tumour. While the exact mechanism by which DMXAA directly targets endothelial cells is not understood, the death of tumour endothelial cells leads to the rupture of vessels, exposure of the basement membrane, and extravasation of erythrocytes into the surrounding tissue. Basement membrane exposure leads to the accumulation of platelets and hence vessel thrombosis (Fig 1.4.3-1) [48, 63].

In the indirect mechanism, DMXAA, disrupts the tumour vasculature by activating cells of the innate immune system (e.g. principally macrophages), causing them to release a variety of pro-inflammatory cytokines and chemokines, including tumour necrosis factor-± (TNF-±), interferon-induced protein-10 as well as nitric oxide (NO) [64-66]. However, the major contributor of the indirect effect of DMXAA appears to be TNF-±, a cytokine

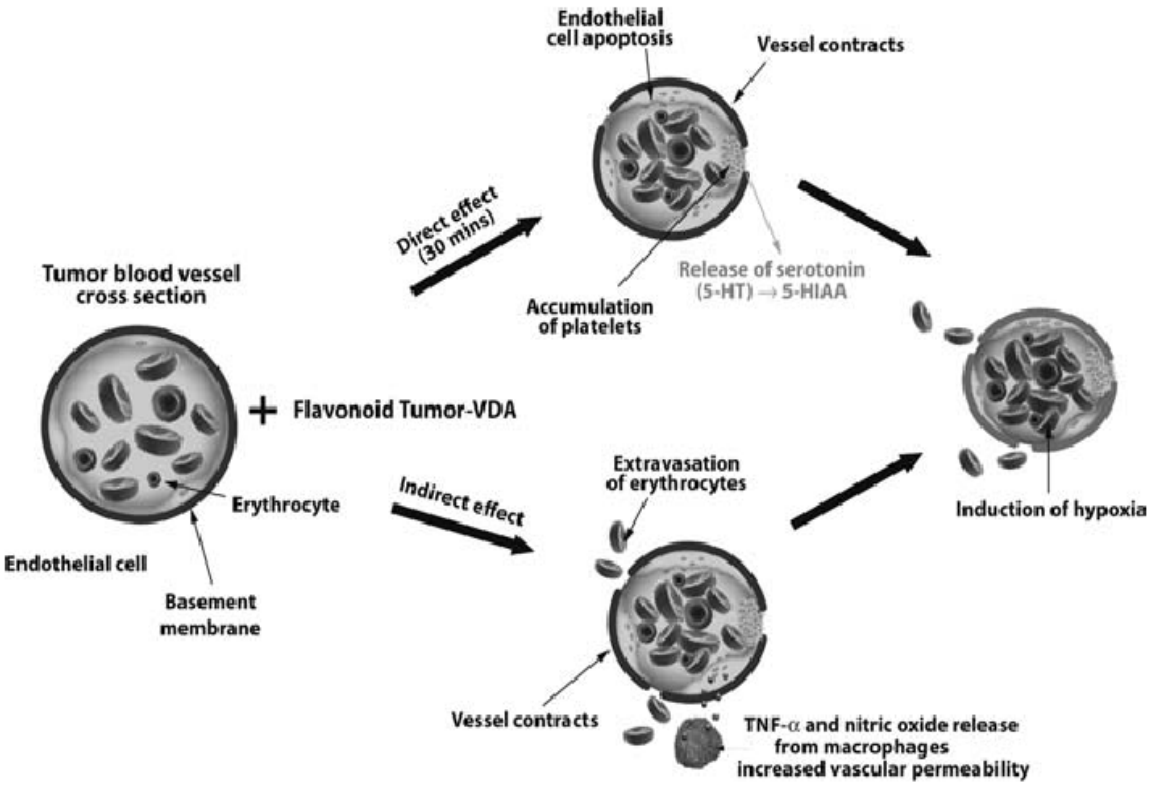

Figure 1.4.3-1 DMXAA dual mechanism of action.

This drug has both indirect and direct mechanisms of action. In the direct mechanism, DMXAA disrupts tumour vasculature by selectively inducing apoptosis in tumour endothelial cells. This drug also targets the vasculature through indirect mechanism mediated by DMXAA-activated macrophages. This figure was printed from (McKeage MJ and Baguley BC, 2010), with permission from Cancer.

that is capable of inducing vascular collapse, increased vascular permeability, vessel thrombosis, and hence, reduced tumour vasculature blood flow (Fig 1.4.3-1) [54, 67-70].

1.5 Thesis goal, hypothesis, and approach

Based on supporting literature, we decided to use DMXAA and GDC-0941, either alone, or in combination to determine whether we could tigger the death of osteolytic metastases in the MDA-MB-231 preclinical model system. The human breast cancer cell line MDA-MB-231, derived from a malignant pleural effusion, was used in our study. MDA-MB-231 cells show a gene expression profile typical of poor prognosis human breast cancer subtype : the triple-negative variant [14]; This line also tends to be very aggressive and readily metastasize to the bone when induced via the intracardiac route. These features make the MDA-MB-231 an ideal model system for the study of bone metastases [14]. The cells we used had been previously transfected with a dual reporter, enhanced green fluorescent protein-luciferase 2 (EGFP-Luc2), in order to allow monitoring of tumour progression in live mice [71]. To generate bone metastases we injected MDA-MB-231/EGFP-Luc2 cells directly into the left cardiac ventricles of nude mice [71]. Upon successful injection, cells enter directly into the arterial circulation and some of these localize to the bone to form metastases. We then targeted the PI3K pathway with GDC-0941, since this pathway is known to be involved in metastatic progression and osteoclast fuction. We also targeted the tumour vasculature with DMXAA to determine whether this agent was able to disrupt blood vessels within of MDA-MB-231/EGFP-Luc2 derived bone metastases and subcutanous tumours.

Hypotheses: Inhibiting the PI3K/Akt pathway, a major anti-apoptotic mechanism, with the PI3K inhibitor, GDC-0941, would limit osteoclast-induced osteolysis, and secondly increase the anti-vascular effect of the VDA, DMXAA, enhancing the ability of this drug to cause necrosis of bone metastases.

Aims are as follows:

Aim 1: Examine the effect of GDC-0941 on the growth of osteolytic metastases using the MDA-MB-231 breast cancer metastases model.

Aim 2: Compare therapeutic effect of DMXAA on MDA-MB-231 breast cancer cell line-induced osteolytic metastases vs. subcutaneous tumours.

Aim 3: Examine the effect of DMXAA, both alone and in combination with GDC-0941, on the survival of osteolytic metastases.

Chapter Two: Material and Methods

2.1 Cell Culture

The human breast cancer cell line MDA-MB-231 was kindly provided by Dr. T. Guise (University of Virginia, Charlottesville). This cell line was stably transfected by Alla Bondareva in labratory of Dr. Frank Jirik with a dual reporter system, consisting of an enhanced green fluorescent protein (EGFP)-luciferase-2 (Luc2) fusion protein under the control of the cytomegalovirus promoter (CMV) promoter [71]. After selection in G418 (neomycin resistance), the transfected cells were sorted by fluorescence-activated cell sorting (FACS) gating on the cells showing high EGFP expression [71]. Polyclonal mixture of FACS-sorted cells expressing EGFP-Luc2 were expanded and frozen back in multiple aliquots for the use in experiments. MDA-MB-231/EGFP-Luc2 cells were cultured in Dulbecco's modified Eagle's medium (DMEM; Invitrogen, Grand Island, NY) supplemented with 10% fetal bovine serum (FBS), 100 U/ml penicillin, 100 µg/ml streptomycin and 0.8 mg/ml geneticin (Invitrogen) at 37 ^{o}C in a 5% CO_2 humidified atmosphere, and routinely passaged every 2-3 days. Phosphatase and tensin homolog (PTEN)-deficient NCI-H1299 (here after referred to as H1299) cells purchased from American Type Culture Collection (ATCC) were cultured in RPMI 1640 (Invitrogen, Grand Island, NY) supplemented with 10% FBS, 100 U/ml penicillin, 100 µg/ml streptomycin and 0.8 mg/ml geneticin (Invitrogen) at 37 ^{o}C in a 5% CO_2 humidified atmosphere, and routinely passaged every 2-3 days. Both cell lines were confirmed to be

free of pathogenic murine viruses and *Mycoplasma spp* by PCR testing at Charles River Laboratories (Wilmington, MA).

2.2 Mice

All animal studies were approved by the University of Calgary Animal Care Committee under protocol number M08112. Athymic nude (NIH-III) female mice (4-5 weeks old) were purchased from Charles River Laboratories (St. Constant, QC). Athymic mice were housed in a viral antibody-free environment in the biohazard area of the University of Calgary Animal Resources Center. All mice were maintained on standard mouse chow (Pico-Vac Lab Mouse Diet #5062), and housed in a barrier facility in accordance with Canadian Council on Animal Care guidelines.

2.2.1 Bone metastases model

Metastatic tumours were generated in athymic nude mice by intracardiac (IC) injection of 2 x10^5 MDA-MB-231/EGFP-Luc2 cells in 100 μl PBS into the left ventricle. Mice were anesthetized with 100 mg/kg ketamine and 6 mg/kg xylazine via intraperitoneal (i.p.) injection. Successful intracardiac injections were confirmed by carrying out immediate whole-body-bioluminescence imaging (BLI) to confirm systemic distribution of the cells. Mice were then randomly assigned to different experimental groups. The luciferase reporter, constitutively expressed by the cells, allowed us to monitor not only successful intracardiac injections, but also sites of developing metastases as well changes in the rate of growth, or regression of bone metastases following treatment. Tumour growth was

monitored once a week by bioluminescence imaging (BLI) (IVIS-Lumina, Caliper Life Sciences) (Fig 2.2-1). The following describes the four experimental groups that were used in each aim, respectively:

Group one mice, used to determine effect of GDC-0941 on metastases, were imaged on day 7, 14, and 21 using BLI. Once tumours were established on day 14, mice were divided into two sub-groups: (1) a control group (N=5 mice, N=4 tumour-bearing legs) were given 100 µl of vehicle (DMSO-Tween 20) daily via gavage from day 14 to 21; (2) a drug treated group (N=4 mice, N=6 tumour-bearing legs) which were treated with 100 µL of GDC-0941 (75 mg/kg) + vehicle daily by gavage from days 14 to 21. Both groups were scanned for bioluminescent signals on days 17 and 21 to monitor sites of soft tissue metastases and changes in the rate of growth or regression of bone metastases following treatment. On day 21 both groups were sacrificed. At necropsy limbs and organs were collected to confirm sites of metastases via BLI ex *vivo*. Organs from control and treated mice were then stored in 10% neutral buffered formalin (NBF) at room temperature. Limbs were stored in 4% paraformaldehyde (PFA) at 4 ºC for micro-computed tomography (µCT) analysis and histology.

Group two mice, used to assess effect of DMXAA on bone metastases, were imaged on days 7, 14, and 21 to monitor tumour growth. On day 21, mice were divided into two sub-groups: (1) a control group (N=10 mice, N=10 tumour-bearing legs) which were treated with a one-time i.p. injection of vehicle (DMSO) on day 21; (2) a drug treated group (N=9 mice, N=14 tumour-bearing legs) treated with a one-time i.p. injection of DMXAA (25 mg/kg) + vehicle on day 21. Soft tissue metastases, and changes in the rate of growth or regression of bone metastases were monitored by

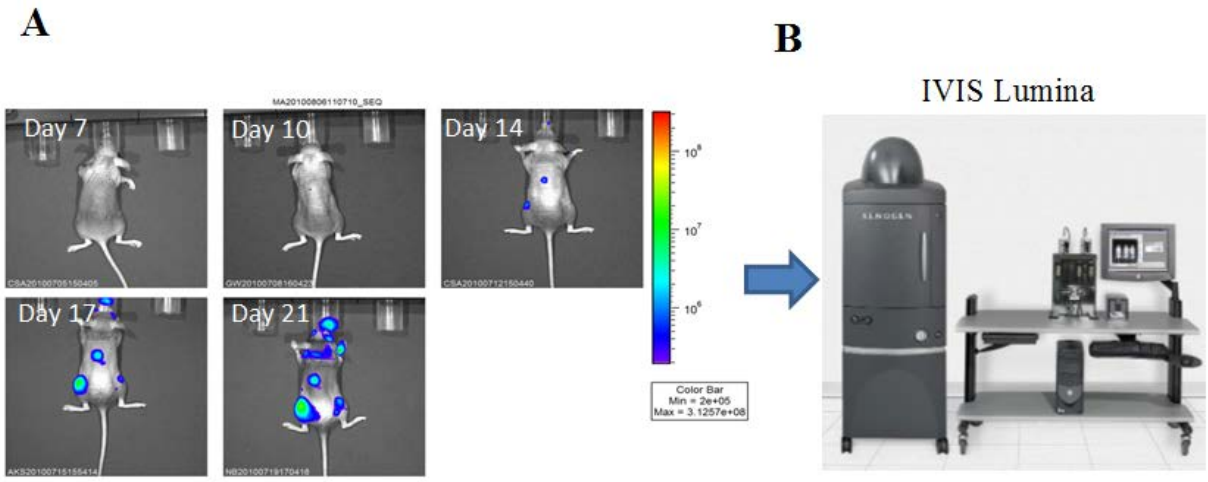

Figure 2.2-1 Monitoring tumour growth *in vivo* using bioluminescence imaging.

(A) Representative images of a mouse in a dorsal position scanned on days 7, 10, 14, 17, and 21 post-intracardiac injection of MDA-MB-231/EGFP-Luc2 cells. (B) IVIS Lumina instrument used for 2D bioluminescence imaging (BLI), with light emission measured in absolute units (photon/sec).

bioluminescence imaging at 6, 24, 48, 72, 96, and 120 hours post-treatment. Mice were sacrificed at the 120 hr time point and the limbs from the control and treated group were stored in 4% PFA at 4 ºC for histology.

Group three mice, used to assess effect of combination DMXAA+GDC-0941 therapy on bone metastases, were imaged on days 7, 14, and 19 to monitor tumour growth. On day 19, mice (N=9 mice, N=10 tumour-bearing legs) were treated with daily gavages of GDC-0941 (75 mg/kg) from days 19-25 and a one-time i.p. injection of DMXAA (25 mg/kg) on day 21. This group was then compared to the control group (group 2 mice from DMXAA study). Soft tissue metastases and changes in the rate of growth or regression of bone metastases were monitored by bioluminescence 6, 24, 48, 72, 96, and 120 hours post-treatment. After the last scan, mice were sacrificed and the limbs from the control and treated groups were placed in 4% PFA at 4 ºC for histological analysis.

Group four mice, used to assess effect of 24 hrs DMXAA therapy on bone metastases, were subjected to BLI on days 7, 14, and 21 to monitor tumour responses. The same steps as group two were followed for group four. However, soft tissue metastases and changes in the rate of growth or regression of bone metastases were monitored by BLI at 6 and 24 hrs post-treatment (N=15 mice, N=20 legs). Mice (N=6 mice, N=12 legs) were sacrificed at the 24 hr time point post-DMXAA treatment and limbs collected in 4% PFA at 4 ºC for histology.

2.2.2 Subcutaneous H1299 (NSCLC) tumours

Subcutaneous tumours were generated by injecting single cell suspensions of 2 x10^6 NCI-H1299 cells in 100 µl of PBS in the right posterior flank of NIH-III mice (N=6). Approximately 40 days later mice with subcutaneous tumours (~1 cm^3) were divided into two groups: (1) a control group that was gavaged with 100 µl of vehicle (DMSO/Tween20); and (2) a drug treated group that were gavaged with 100 µl of 75 mg/kg GDC-0941. After 6 hrs, the mice were sacrificed and tumour lysates were prepared.

2.2.3 Subcutaneous MDA-MB-231/EGFP-Luc2 tumours

Subcutaneous tumours were generated by injecting single cell suspensions of 2 x10^6 MDA-MB-231-EGFP-Luc2 cells in 100 µl of PBS in both the right and left posterior flanks of NIH-III mice (N=18 tumours). Tumour growth was monitored once a week via BLI. Approximately 30 days later, when tumours were established, mice were divided into two groups: (1) a control group (N=8 tumours) that were treated with a one-time i.p. injection of vehicle (DMSO); (2) a drug treated group (N=10 tumours) that were treated with a one-time i.p. injection of DMXAA (25 mg/kg) in DMSO. Mice were imaged for bioluminescence at 6 and 24 hours post-treatment and then sacrificed. The tumours from the control and treated groups were collected and put in 10% NBF at room temperature for histological analysis.

2.3 Bioluminescence imaging

BLI was performed as previously described [71]. Briefly, prior to imaging, each mouse received an i.p. injection of 200 µl of 150 µg/ml *D*-luciferin (Gold Bio Technology; St. Louis, MO) in PBS. Mice were then were anesthetized with 1.5-2% isofluorane for 10-12 min. The luciferase expressed by the tumour cells cleaves the *D*-luciferin substrate causing an oxidation reaction to occur that produces photons of light that can be detected by the bioluminscence imager. The imaging process must occur within 10-20 min after injection of luciferin because once luciferin is oxidized it becomes inactive. Anesthesia with 1.5-2% isofluorane was maintained when the animals were placed onto the warmed stage of the IVIS light-tight chamber during the scanning. Each mouse was scanned in both dorsal and ventral positions. Bioluminscence images were collected and photon emission rates quantified for the legs and the whole body in order to evaluate tumour growth. Whole-body-bioluminescence was quantified using both dorsal and ventral positions and knee bioluminescence was quantified using only the ventral position. In order to measure whole-body-bioluminescence, the region of interest (ROI) with width of 100 (pix) and height of 200 (pix) was measured from dorsal and ventral positions. The values were added and used to evaluate whole-body tumour growth rates. To measure knee bioluminescence, the ROI with width of 25 (pix) and height of 25 (pix) was used for each knee in the ventral position. Lastly, to measure subcutaneous tumour bioluminescence an ROI with width of 30 (pix) and height of 30 (pix) was used for each tumour in the dorsal position. The bioluminescence values from the knees were used as a measure of tumour growth rate. Total flux values were then baseline corrected and

graphed using GraphPad Prism 4.0 Software. There are several limitations for usage of BLI in this study that need to be considered, such as changes in bioluminescence due to slight differences in the positioning of the limbs within the detection chamber, the fact that instrument used only gives a two-dimensional image that does not take into account the depth of the tumour, and the likelihood that bioluminescence signals increase once the tumour has eroded through the cortical bone.

2.4 Western blotting

2.4.1 Confirming GDC-0941 activity in vitro

MDA-MB-231/EGFP-Luc2 cells were grown on tissue culture plates. Once the cells reached 80% confluency, the cells were serum starved for 12 hrs and treated with different concentrations of GDC-0941 (50 nM, 150 nM, 300 nM and 500 nM) for one hour, and then 50 ng/ml insulin-like growth factor 1 (IGF-1) (cat# 240-B R&D System) was added for 5 min prior to cell lysis (between 5 and 10 min is the optimal time to detect AKT phosphorylation). Cells alone and cells stimulated only with 50 ng/ml IGF were used as controls. After treatment, cells were lysed in 0.3 ml of lysis buffer (10 mM Tris pH 7.4, 150 mM NaCl, 5 mM EDTA, 1% Triton x100) containing a cocktail of protease and phosphatase inhibitors (Roche). A standard BSA curve was used to quantify lysate concentrations to allow loading of equal amounts of total protein from each sample on the gel. Lysates (30 µg/lane) were loaded on 10% polyacrylamide gels, separated by electrophoresis, blotted on a polyvinylidene difluoride (PVDF) filter membrane, blocked with 5% skim milk for 1 hr, and immunoblotted with the following antibodies: 1:750

dilution of mouse monoclonal anti-phospho-AKT (S473) as a primary antibody (Cell Signalling cat# 4051S) followed by a 1:5000 dilution of an anti-mouse IgG horseradish peroxidase (HRP)-linked secondary antibody (Cell Signalling cat#7076); 1:1000 dilution of rabbit monoclonal anti-AKT (detects both phosphorylated and un- phosphorylated AKT) as a primary antibody (Cell Signalling cat # 4691S) followed by a 1:5000 dilution of an anti-rabbit IgG HRP-linked secondary antibody (Cell Signalling cat# 7074); and 1:1000 dilution of a rabbit anti-actin (I-19) sc-1616 antibody (Santa Cruz). HRP-conjugated secondary antibodies were used for chemiluminescence imaging of the membrane.

2.4.2 Confirming GDC-0941 activity in vivo

In order to confirm inhibition of the PI3K signalling pathway with GDC-0941 *in vivo*, we generated athymic nude (NIH-III) female mice (4-5 weeks old) with subcutaneous H1299 non-small-cell lung carcinoma (NSCLC) tumours. Due to PTEN deficiency, this cell line has a high level of PI3K pathway activation. Once subcutaneous tumours were generated, mice were treated with GDC-0941 or vehicle as described in section 2.2.2. Tumours were dissected 6 hrs post-treatment and lysates prepared. Samples were homogenized and centrifuged for 15 min at 13,000 rpm. Lysates (30μg/lane) were immunoblotted with the following antibodies: (a) monoclonal anti-phospho-AKT (S473) and (b) monoclonal anti-AKT to assess total AKT levels.

2.4.3 Densitometry

Normalized phospho-AKT values were obtained as follows: AKT levels were initially normalized to the ² -actin levels. Phospho-AKT levels were then normalized to the levels of “normalized” AKT values. Normalized values from phospho-AKT were then graphed and statistical analyses carried out using the 2-tailed unpaired T test in GraphPad Prism 4.0 Software.

2.5 MTT assay

The MTT [3-(4,5-dimethylthiazol-2-yl)-2,5-diphenyltetrazolium bromide] assay was used as a measure of viable cell numbers. In this colorimetric assay the mitochondria of live cells convert MTT to formazan dyes, giving a purple color that can be measured at 550 nm and 620 nm to assess viable cell numbers. MDA-MB-231/EGFP-Luc2 cells were plated in triplicate at 4000 cells per well in 96 well plates and 2 µl of various drug concentrations (50 nM, 150 nM, 300 nM, 500 nM, and 1000 nM) were added for 24, 48, and 72 hrs. After, incubation media were removed and replaced with 200 µL of fresh media containing MTT (final concentration, 250 µg/mL). Plates were then incubated for 3-4 hrs. After incubation, the media from each well was removed and replaced with 200 µl of dimethyl sulfoxide (DMSO) to solubilize the MTT tetrazolium crystal [72]. Lastly, the optical density was measured at 550 nm and 620 nm using a *Labsystems Multiskan* Plus Plate Reader (Fisher Scientific, USA). The absorbance values at 550 nm were subtracted from the value of 620 nm to assess viable cell numbers. This experiment was

done three times and each time it was carried out in triplicates. Triplicate wells were averaged from each experiment and plotted in GraphPad Prism 4.0 Software for statistical analysis using a one-way ANOVA, Newman-Keuls test (GraphPad Software Inc., San Diego, CA).

2.6 Micro-computed tomography analysis

Micro-computed tomography analysis (μCT) was used to measure bone loss resulting from osteolytic metastases. μCT utilizes an x-ray source that illuminates an object while a planar x-ray detector collects and magnifies a projection image of that object. X-rays hit the object at various angles as the object is rotated, so as to allow the computer program to create a stack of virtual cross section slices of the object. Cross sectional slices can then be viewed individually to look within the object or they can be combined to create a 3D representation. In this study, μCT allowed us to measure bone mineral content and to view lesions caused by bone metastases. Legs were dissected and placed in a 4% PFA fixing solution at 4 ºC before scanning. Scanning was completed within the next 24 hours after harvesting. Before scanning, legs were cleaned with PBS and placed into an airtight cylinder sample holder in the μ-CT scanner (VivaCT 40, Scanco Medical AG, *Brüttisellen*, Switzerland). A maximum of 6 legs were placed in the cylinder sample holder and the whole leg was scanned. Serial tomographic slices were acquired in 10 μm increments at 70 kV, 114 μA and 250 ms. The resulting segmented images were analyzed using direct 3-D measurement techniques and maximal spheres were done on a 2.5 mm

region of the distal femur and proximal tibial growth plates (Image Processing Language, v5.05a) [3].

2.7 Histopathology and immunohistochemistry

Limbs obtained from control and treated mice were put into 4% PFA and stored at 4 ºC. PFA was refreshed after 24 hrs and left in for another week. Limbs were decalcified in 14% ethylenediaminetetraacetic acid (EDTA) solution for a minimum of 24 hrs (with 14 consecutive changes). The decalcified limbs were then embedded in a 50:50 paraffin wax block and sectioned at 4-5 µm. Every 5^{th} section was stained for Masson's Trichrome stain (consists of hematoxylin (blue), fast green (green), and safranin-O (red) stains), or hematoxylin & eosin (H&E) stain.

2.8 Statistical analyses

All graphs were plotted as mean ±SEM. Statistical analysis were performed using the 2-tailed unpaired T test and either a two-way or one-way ANOVA with GraphPad Prism 4.0 (GraphPad Software Inc.,San Diego, CA). Values of $P < 0.05$ were considered statistically significant. *P* values of < 0.05, < 0.01, and < 0.001, were indicated by (*), (**), and (***), respectively.

Chapter Three: Examining the effect of GDC-0941 on the growth of osteolytic metastases.

3.1 Aim

This chapter concerns a study of the effect of the pan-PI3K inhibitor, GDC-0941, on the growth of established osteolytic bone metastases due to the MDA-MB-231/EGFP-Luc2 breast cancer cell line.

3.2 Background and hypothesis

The PI3K/AKT signalling pathway is one of the critical signals downstream of both the RANK and M-CSF receptors that are involved in osteoclast differentiation and activation [18, 73]. This pathway also enhances cell survival, metabolism, proliferation, and migration [30]. Inhibition of the PI3K/AKT pathway in osteoclasts has been shown to lead to inhibition of bone resorption *in vitro* and *in vivo* by interfering with osteoclast migration, and interruption of ruffled boarder formation [74]. *In vitro* studies also showed that inhibition of PI3K increased osteoclasts apoptosis [75]. In addition, the PI3K/AKT pathway has been shown to be involved in the growth and/or invasiveness of various cancers such as breast, prostate, thyroid and ovarian cancer [76]. Since this pathway plays a major role both in cancer cells and osteoclasts, it was rational to target this pathway with a pan-PI3K inhibitor to study the effect of its inhibition on osteolytic metastases. GDC-0941 selectively binds to the ±, ², and ´ isoforms of the p110 catalytic subunit of class IA PI3Ks in an ATP-competitive manner, thus preventing activation of

the PI3K/AKT signalling pathway [37]. We predicted that inhibition of this pathway with GDC-0941 would halt osteoclast activation and differentiation and/or decrease survival, growth, and proliferation of bone metastases due to the MDA-MB-231/EGFP-Luc2 cell line. However, it was important to note that there was the possibility that GDC-0941 might not show any significant effect on the growth of the MDA-MB-231/EGFP-Luc2 cells. This was due to the low basal level of PI3K pathway activity exhibited by in these cells [77]. In addition, MDA-MB-231/EGFP-Luc2 cells have also been shown to be resistant to PI3K inhibitors in literature [77]. Thus, the main rationale for using this drug on osteolytic metastases was to explore the potential for GDC-0941 to target osteoclasts and thus decrease osteolytic damage. μCT was used not only to obtain 3D images of osteolysis but also for the quantification of tumour-induced bone loss. Using μCT, it is possible to measure trabecular and cortical bone volume, connectivity, and spherical areas for both the tibia and femur in order to quantify bone loss.

3.3 Results

3.3.1 Confirming GDC-0941 activity

Before using GDC-0941 we wanted to confirm that this drug inhibits the PI3K signalling pathway by decreasing the levels of phospho-AKT, a key protein located downstream of the PI3K activation.

3.3.1.1 In vitro studies

In order to confirm that GDC-0941 that was purchased (AXON) was active and able to inhibit the PI3K/AKT pathway *in vitro*, MDA-MB-231/EGFP-Luc2 cells were grown on a 6-well plates and treated with the indicated drug concentrations for one hour (Fig 3.3-1 A). Because MDA-MB-231/EGFP-Luc2 cells demonstrate a low basal level of PI3K pathway activity [77] they were also stimulated for 5 min with IGF-1 to activate this pathway prior to GDC-0941 addition. In this experiment cells alone and cells stimulated with IGF-1 were used as controls. The low level of PI3K pathway activity of MBA-MB-231/EGFP-LUC2 cells can be viewed by the faint phospho-AKT band in lysates from cells that were not stimulated with IGF-1 (lane 5, Fig 3.3-1 A). Upon treatment with IGF-1, phospho-AKT levels increased significantly (lane 6, Fig 3.3-1 A, B). However, the addition of GDC-0941 inhibited the IGF-1-induced increase in phospho-AKT in a dose-dependent manner (lane 1-4, Fig 3.3-1 A). Phospho-AKT in cells exposed to 500 nM GDC-0941 were greatly supressed (Fig 3.3-1 B). AKT immunoblotting proved that there was no change in the expression levels of total AKT protein during the time course of the experiment.

A

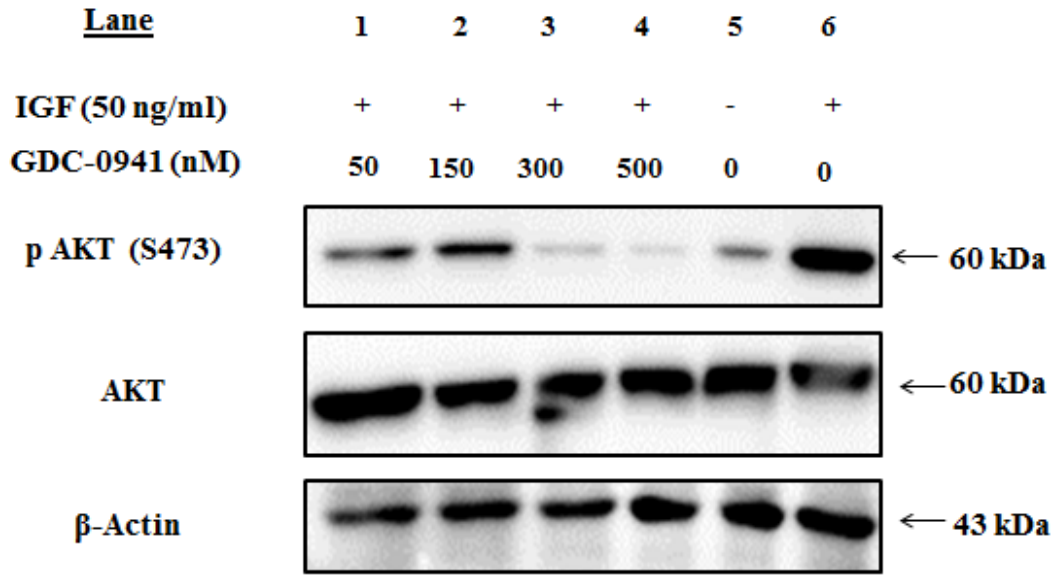

B

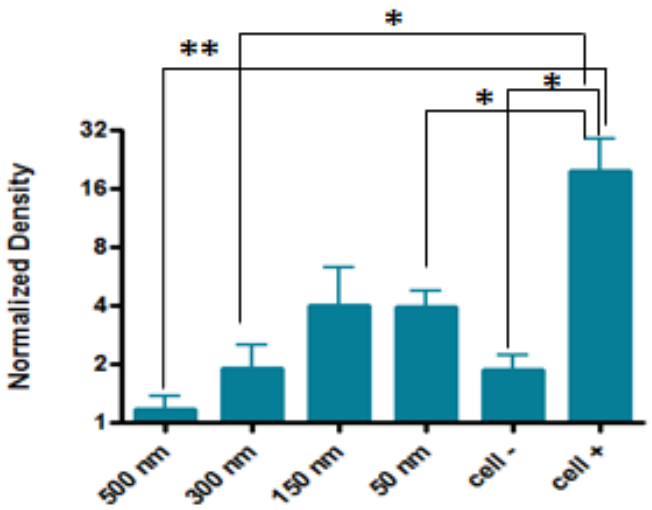

Figure 3.3-1 GDC-0941 inhibits the PI3K/AKT pathway *in vitro*.

(A) Imunoblotting of lysates prepared from MDA-MB-231/EGFP-Luc2 cells treated with various concentrations of GDC-0941 in combination with IGF-1 followed by detection of phospho-AKT and total AKT protein expression. (B) Densitometry for phospho-AKT normalized to AKT levels that had also been normalized to ² -actin levels. Data are the mean ± SEM n=3. Statistical analyses were carried out using the 2-tailed unpaired T test, * $p<0.05$ and ** $p<0.01$.

3.3.1.2 In vivo studies

To measure that inhibition of the PI3K signalling pathway was also occurring with GDC-0941 *in vivo*, we generated subcutaneous H1299 tumours in athymic nude (NIH-III) female mice, and then treated them with GDC-0941, or vehicle control by gavage. The reason we used H1299 instead of MDA-MB-231/EGFP-Luc2 cell line to confirm that GDC-0941 works *in vivo* is because H1299, being deficient in PTEN, has high PI3K signalling pathway activity [78]. PTEN is a negative regulator of PI3K. Thus, if GDC-0941 was able to inhibit the high levels of PI3K signalling in H1299, it would likely be able to inhibit PI3K in mouse tissues (e.g. osteoclasts). After 6 hours the H1299 tumours were dissected, and lysates were prepared from these tumours for immunoblotting for phospho-AKT, total AKT, and ²-actin levels expression. In Figure 3.3-2 A, lanes 1-3 each represent an individual mouse (with subcutaneous H1299 tumour) that was gavage treated with 100 µl of 75 mg /kg GDC-0941 for 6 hrs. In lanes 1-3, the phospho-AKT bands were very faint, representing a lower level of activated AKT present in the lysates. The levels of phospho-AKT were significantly lower in lanes 1-3 owing to GDC-0941 inhibition of the PI3K pathway (Fig 3.3-2 B). Lanes 4-6 represent negative controls and each lane represents a tumour from one mouse that was treated with vehicle control (Fig 3.3-2 A). In these lanes a dark band for phospho-AKT represents a high level of PI3K signalling pathway expression in the H1299 cell line that were not treated with GDC-0941.

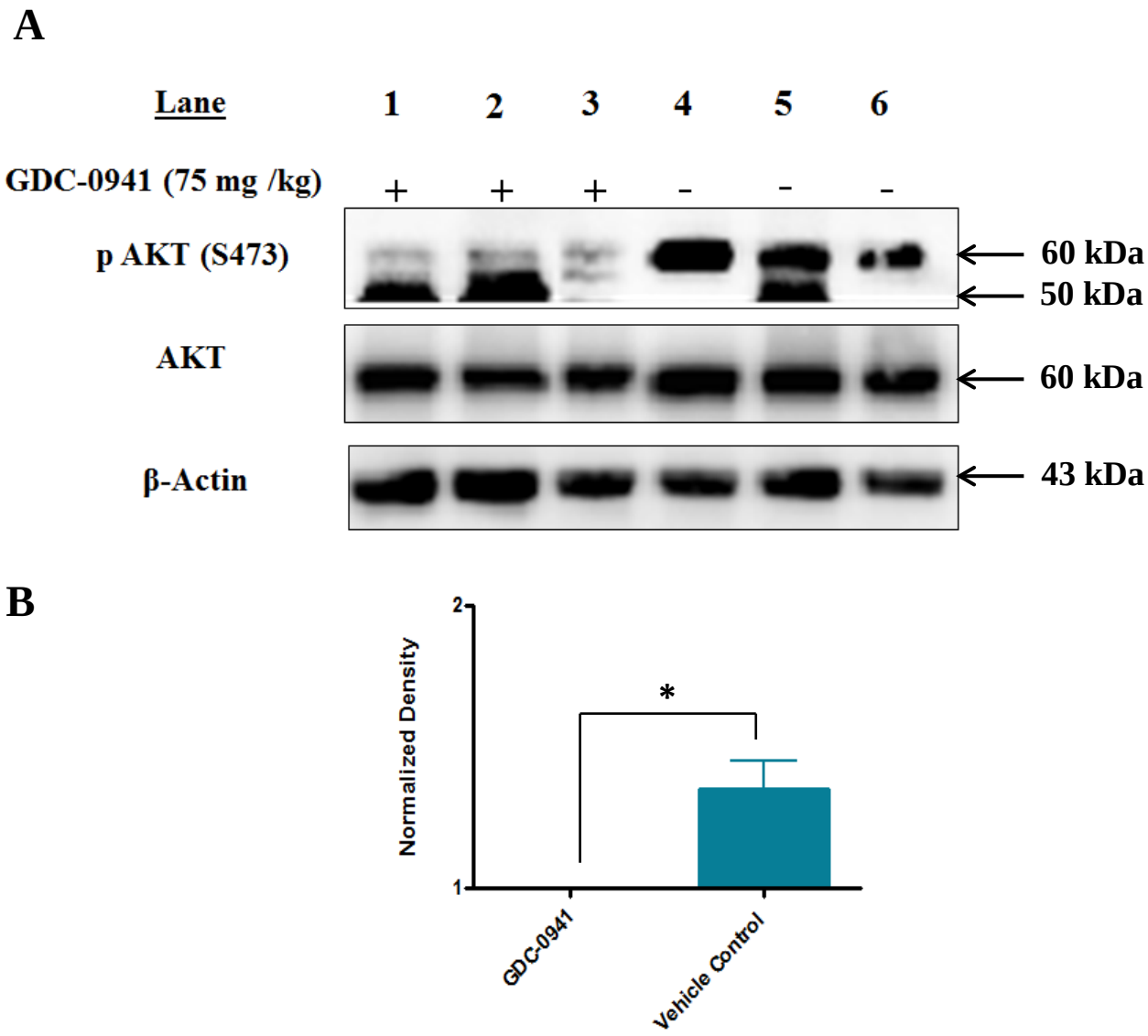

Figure 3.3-2 GDC-0941inhibit the PI3K/Akt pathway *in vivo*.

(A) Immunoblotting of lysates prepared from subcutaneously grown H1299 tumours treated with GDC-0941 or vehicle control for phospho-AKT and total AKT protein determinations. The variable appearance of the dark bands under the phospho-AKT band was most likely due to variable contamination of the lysate with mouse IgG from mouse plasma in the blood in the tumours. In other words, the secondary antibody used to detect the mouse monoclonal anti-phospho-AKT was also detecting endogenous mouse IgG heavy chains. (B) Densitometry for phospho-AKT normalized to AKT levels that had also been normalized to ²-actin levels. Data are the mean ± SEM n=6 mice group. Statistical analyses were carried out using the 2-tailed unpaired T test, * $p<0.05$.

3.3.2 Examining the effect of GDC-0941 on cell proliferation in vitro

We used the MTT assay to test if GDC-0941 had any effect on MDA-MB-231/EGFP-Luc2 cell viability and proliferation. In this experiment MDA-MB-231/EGFP-Luc2 cells were plated in 96-well plates, various drug concentrations added and the cells assessed for viable cell numbers 24, 48, and 72 hrs later. Despite the confirmation that GDC-0941 inhibits the PI3K signalling pathway both *in vivo* (Fig 3.3-1) and *in vitro* (Fig 3.3-2) growth at 48 hrs, GDC-0941 had no detectable effect on MDA-MB-231/EGFP-Luc2 cells (Fig 3.3-3). Similar results were seen after 24 and 72 hrs in the MTT assay (data not shown).

3.3.3 Studying the effect of GDC-0941 on osteolytic metastases

Next, we evaluated the therapeutic effect of GDC-0941 on an osteolytic metastasis model generated using the MDA-MB-231/EGFP-Luc2 breast cancer line. Bioluminescence imaging (BLI) was carried out to monitor metastases *in vivo* looking specifically for changes in the rate of growth of bone metastases following GDC-0941 treatment. In addition, μCT was carried out to study the effects of GDC-0941 on bone destruction. Immunohistochemistry was carried out to study the effects of GDC-0941 on tumour morphology.

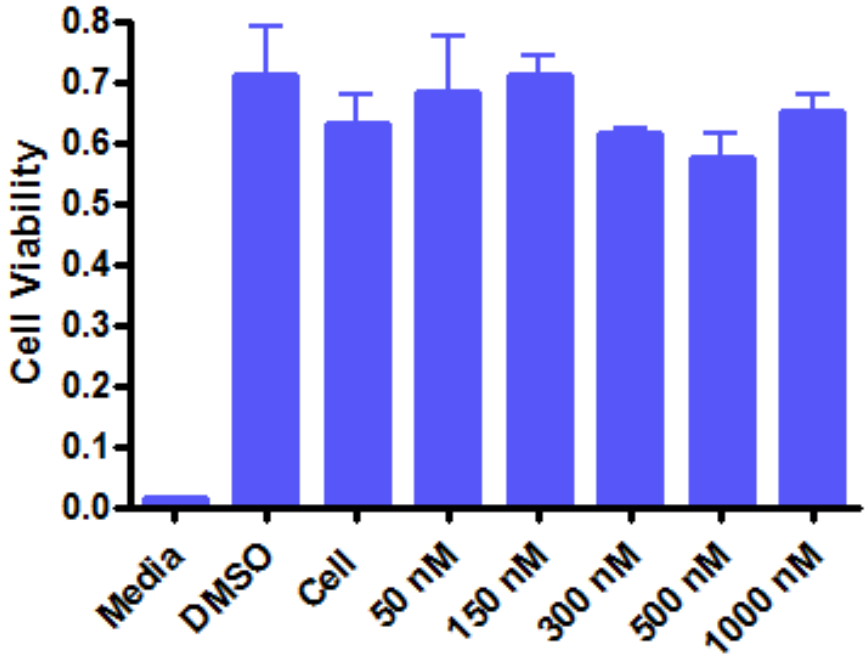

Figure 3.3-3 GDC-0941does not affect MDA-MB-231/EGFP-Luc2 cell proliferation *in vitro*.

MTT assay was used to evaluate the effect of GDC-0941 on the MDA-MB-231/EGFP-Luc2 cell line. MDA-MB-231/EGFP-Luc2 cells were treated with various concentrations (50 nM, 150 nM, 300 nM, 500 nM, and 1000 nM) of GDC-0941 for 48 hours. Controls for these experiments were media alone, cells alone, and cells with DMSO. Data are the mean ± SEM n=3; each experiment was done in triplicate. Each error bar represents average of triplicate optical density values from the independent MTT assay experiments done each in triplicate that were plotted in GraphPad Prism 4.0 Software. One-way ANOVA, Newman-Keuls test was used for statistical analyses, and the value of $P < 0.05$ was considered statistically significant.

3.3.3.1 Measuring tumour growth using BLI

Bone metastases were generated by the intracardiac injection of the MDA-MB-231/EGFP-Luc2 cells. Mice were then treated with GDC-0941 and vehicle control daily from day 14-21 post-injection and bioluminescence measured from both groups (Fig 3.3-4). BLI was collected and quantified for the knee and the whole body to evaluate tumour growth rates (Fig 3.3-5B, 6B). Knee BLI measurements from both GDC-0941 treated mice and vehicle control mice did not show any significant difference (Fig 3.3-5 A). Whole body BLI measurements from both GDC-0941 treated mice and vehicle control mice also did not show any significant difference (Fig 3.3-6A).

3.3.3.2 Studying the effects of GDC-0941 on bone osteolysis

Even though GDC-0941 did not show any effect on tumour growth (anticipated due to the low basal levels of PI3K pathway activity in MBA-MB-231/EGFP-LUC2 cells), we evaluated the effect of this drug on osteolysis using μCT in order to quantify tumour-induced bone loss. The purpose of this experiment was to see if GDC-0941 had the potential to inhibit osteoclast activation and differentiation, cells responsible for tumour-mediated osteolysis. Measurements of trabecular and cortical bone volume and thickness, bone mineral density, connectivity and void measurement technique for both the tibia and femur were carried out to assess bone destruction. Trabecular bone volume, for both the tibia and femur, was measure as total trabecular bone volume over total bone volume (BV/TV), as represented in figure 3.3-7.

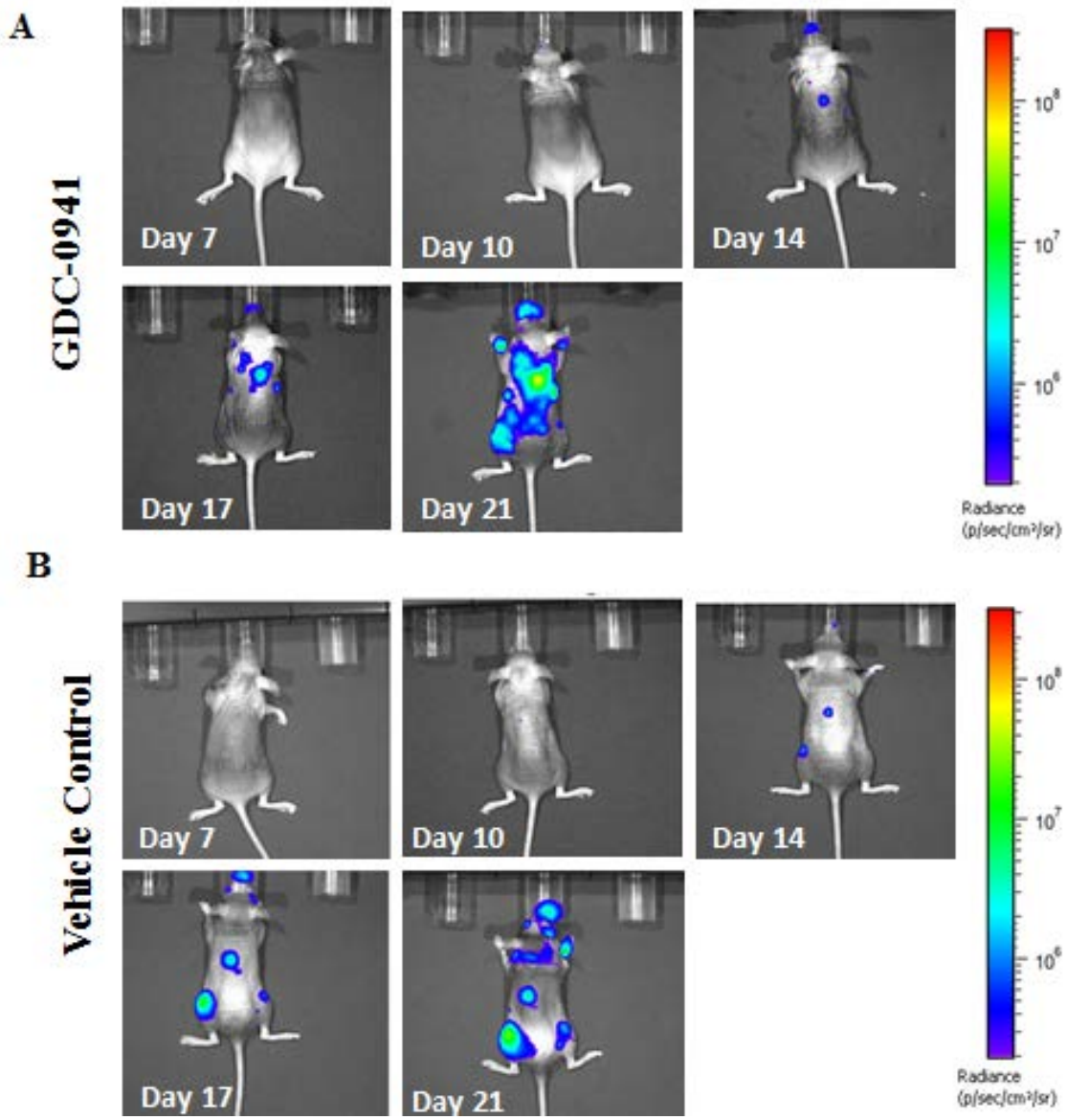

Figure 3.3-4 Measuring the growth of MDA-MB-231/EGFP-Luc2 tumours *in vivo* using BLI.

Bioluminescence imaging was performed on days 7, 10, 14, 17, and 21 after intracardiac injection of MDA-MB-231/EGFP-Luc2. Representative dorsal images of a GDC-0941 treated mouse (A) and a vehicle control treated mouse (B). Scales bars are in photon/s/cm^2. Whole body bioluminescence, a measure of tumour burden, is presented in this representative set of images to show the location of the tumours and the relative growth rates of the lesions in for both GDC-0941 and vehicle control treated mice.

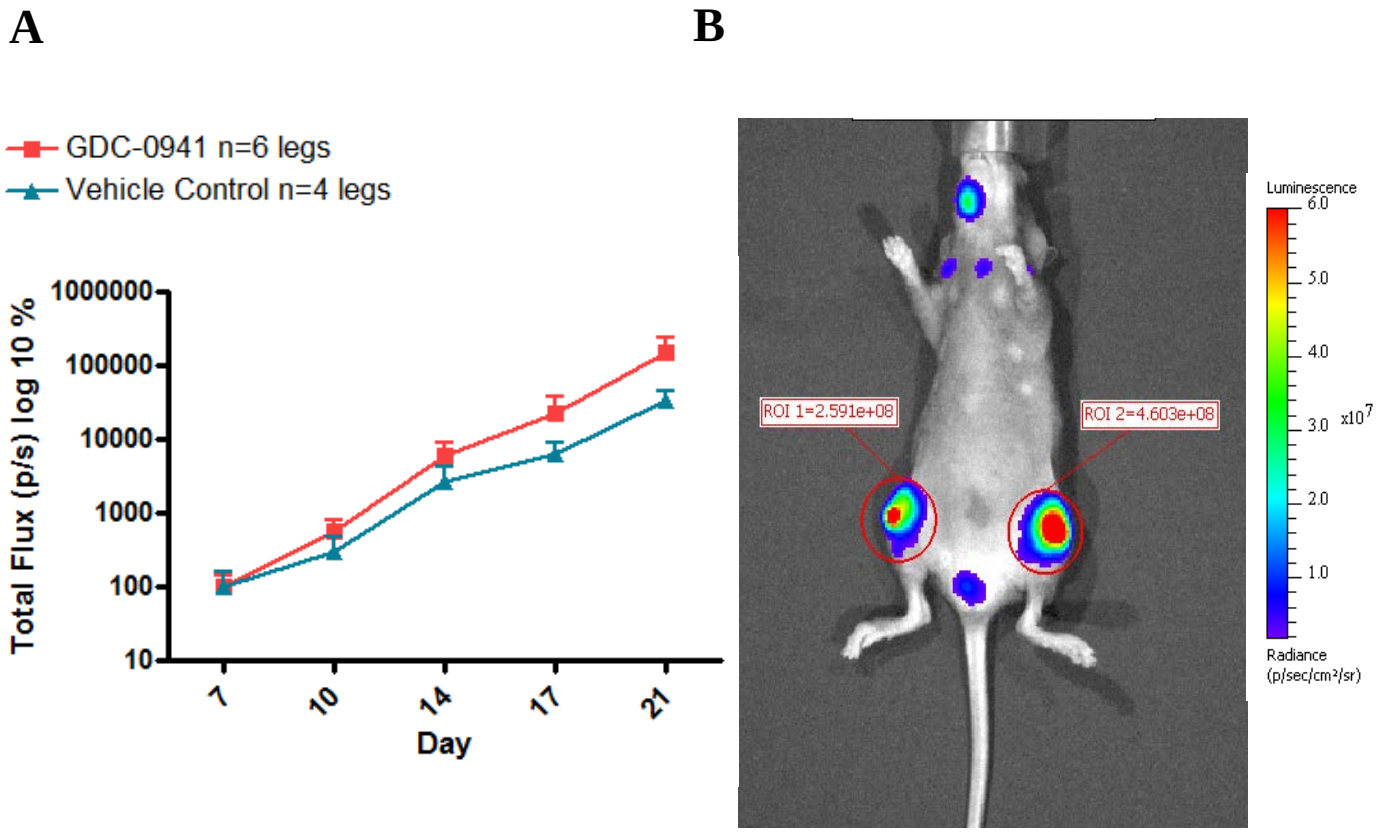

Figure 3.3-5 Quantification of knee bioluminescence of GDC-0941 and vehicle control treated mice.

(A) Photon emission rates from the knees of GDC-0941 and vehicle treated mice measured from days 7-21. To measure knee bioluminescence, the region of interest (ROI) with width of 25 (pix) and height of 25 (pix) was selected for each knee in the ventral position. Knee bioluminescence were quantified as a mean photon/s ± SEM. The error bars represent bioluminescence intensities of 6 knees (n=6) collected from GDC-0941 treated mice and the bioluminescence intensities of 4 knees (n=4) collected from vehicle control mice. Total flux values representing bioluminescence intensities were baseline corrected and graphed using the GraphPad Prism 4.0 Software. Statistical analyses were performed using two-way ANOVA in GraphPad Prism and values of $P < 0.05$ were considered statistically significant. (B) A representative image of a mouse in a ventral position showing the ROI used to evaluate the growth rate of the osteolytic metastases.

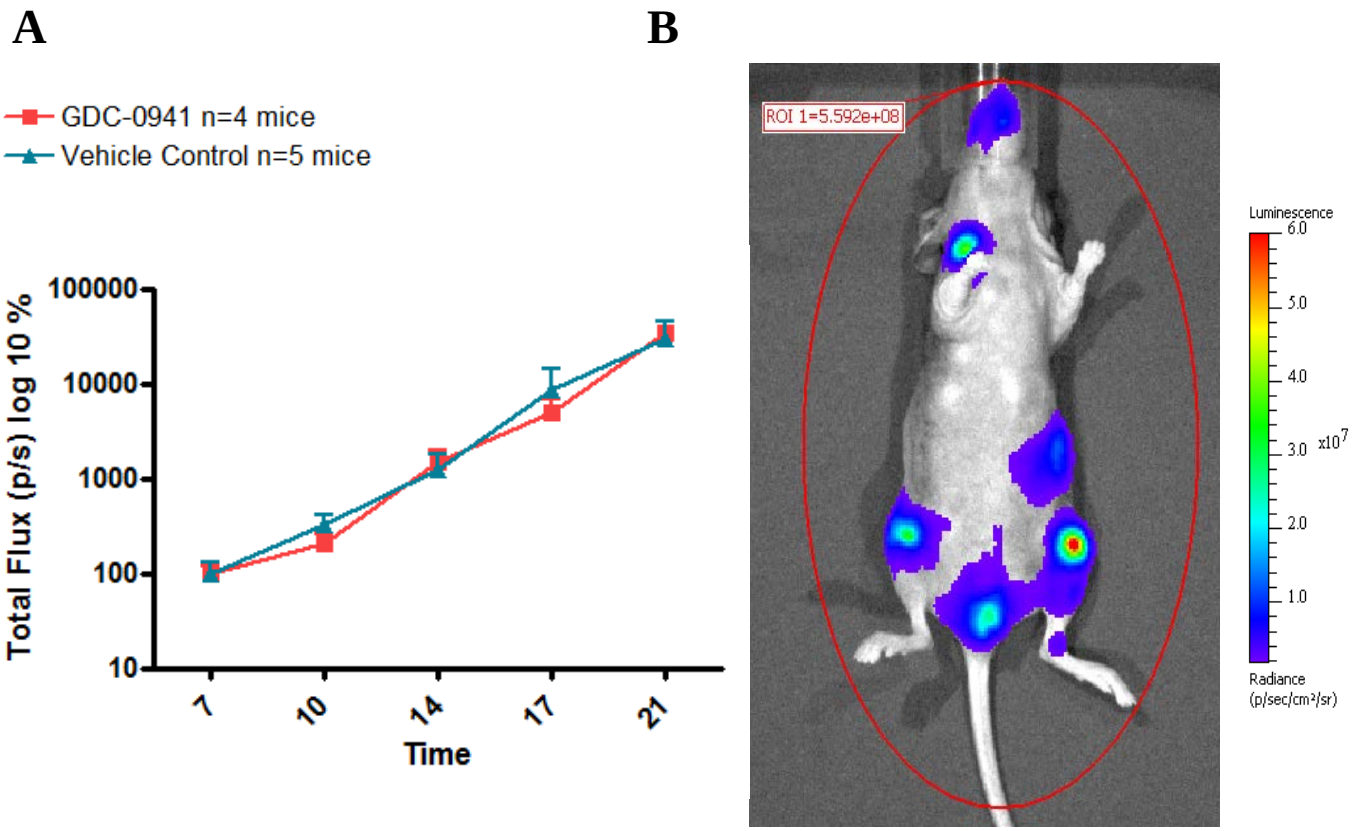

Figure 3.3-6 Quantification of the whole body bioluminescence intensities of GDC-0941 and vehicle control treated mice.

(A) Whole body bioluminescence signals from GDC-0941 and vehicle treated mice were measured from days 7-21. The region of interest (ROI) with width of 100 (pix) and height of 200 (pix) was measured for the whole body in the ventral and dorsal positions, and was quantified as a mean photon/s ± SEM. The error bars represent whole body bioluminescence intensities of 4 GDC-0941 treated mice (n=4) and 5 vehicle control mice (n=5). Total flux values representing bioluminescence intensities were baseline corrected and graphed using GraphPad Prism 4.0 Software. Statistical analyses were performed using two-way ANOVA in GraphPad Prism, values of $P < 0.05$ were considered statistically significant. (B) A representative image of a mouse in a ventral position showing the ROI method used to evaluate the whole body bioluminescence intensity.

Lower BV/TV compared to the controls demonstrates a decrease in the amount of trabecular bone present, likely as a result of damage caused by the tumour. Effects of the drug on cortical bone volume, for both the tibia and femur, were measured as cortical bone porosity (Fig 3.3-8). Cortical bone porosity represents the void area within the bone that could be due to presence of a tumour. Thus, the higher the percentage of cortical bone porosity the more damage and void area present within the bone. Bone mineral density was also measured to determine if the tumour presence within the bone would affect the bone mineral level (Fig 3.3-9 A). Standard deviation (SD) of bone separation was measured for both tibia and femur in order to determine the level of bone connectivity (Fig 3.3-9 C). Higher SD bone separation represents lower bone connectivity possibly due to damage caused by the tumour. Trabecular and cortical bone thickness were measured for both tibia and femur in order to determine if the tumour was causing any damage to the bone and rendering the bone thinner (Fig 3.3-9 B and D). Measurements were completed on healthy mice, and mice with osteolytic metastases treated either with vehicle control, or GDC-0941. There was no significant difference in femur trabecular bone volume among all the groups (healthy, vehicle treated, and drug treated) (Fig 3.3-7 A). However, there was a significant decrease in tibial trabecular bone volume in the GDC-0941-treated, but not vehicle-treated osteolytic metastases as compared to the healthy mice (Fig 3.3-7 A). A significant increase in femur cortical bone porosity was also observed in the drug treated osteolytic metastases when compared to both the healthy and vehicle control mice (Fig 3.3-8 A). However, drug treated osteolytic metastases only showed slightly smaller, yet significant, increases in their tibial cortical

bone porosity when compared to healthy mice, likely reflective of smaller tumours in the tibias as compared to the femurs (Fig 3.3-8 A). A number of other parameters were also used as measures of the amount of bone destruction (Fig 3.3-9). No significant difference was observed in the femur and tibia bone mineral density (Fig 3.3-9 A), trabecular bone thickness (Fig 3.3-9 B), or cortical bone thickness (Fig 3.3-9 D) among all groups. However, for femurs, a marginally significant increase in bone separation was observed with drug treated osteolytic metastases compared as to healthy mice (Fig 3.3-9 C). Lastly, there was no significant difference in bone separation of tibia among all groups (Fig 3.3-9 C).

In addition to these parameters, μCT void measurement technique within the bone was completed to try to better evaluate the amount of tumour-induced bone destruction. This method measures the amount of empty space within the bone, which correlates with the amount of bone destruction present within the bone. In the μCT void measurement technique numerous spheres start expanding from point sources until they interact with obstacles such as trabeculae. Once spheres hit an obstacle they stop expanding, and hence their size distribution provides a measure of empty space within the bone. For example, the ends of the healthy bone have a very limited repertoire empty spaces for spheres to expand into. Therefore, in this analysis healthy bone demonstrate a much higher number of small spheres. However, in the presence of osteolytic metastases, the damage to trabecular bone creates large spaces that can be filled by the spheres. Thus, we observed much higher numbers of large spheres within bone containing osteolytic metastases (Fig 3.3-10 B). In addition, the μCT void measurement technique showed a greater number of larger spheres in the drug treated group in both femurs and tibias as compared to the

vehicle treated mice (Fig 3.3-10 A). This unexpected result suggests that GDC-0941 was somehow acting to promote bone loss. This possibility must be tempered by the fact that group numbers were relatively small.

3.3.3.3 Tumour morphological analysis

Trichrome staining was used to analyze the morphology of the osteolytic metastases of both GDC-0941 treated and vehicle control mice. Tissue stained blue or green in the trichrome stain represent bone or bone cells, red stained regions represent cartilage, and the pink stained cells having a disorganized pattern represent the tumour (Fig 3.3-11). Large tumours were visible in the trichrome stains from both GDC-0941 and vehicle control knees (Fig 3.3-11 A and B). Metastatic lesions from both treated and non-treated mice exhibited a similar overall morphology (Fig 3.3-11 A and B).

A **B**

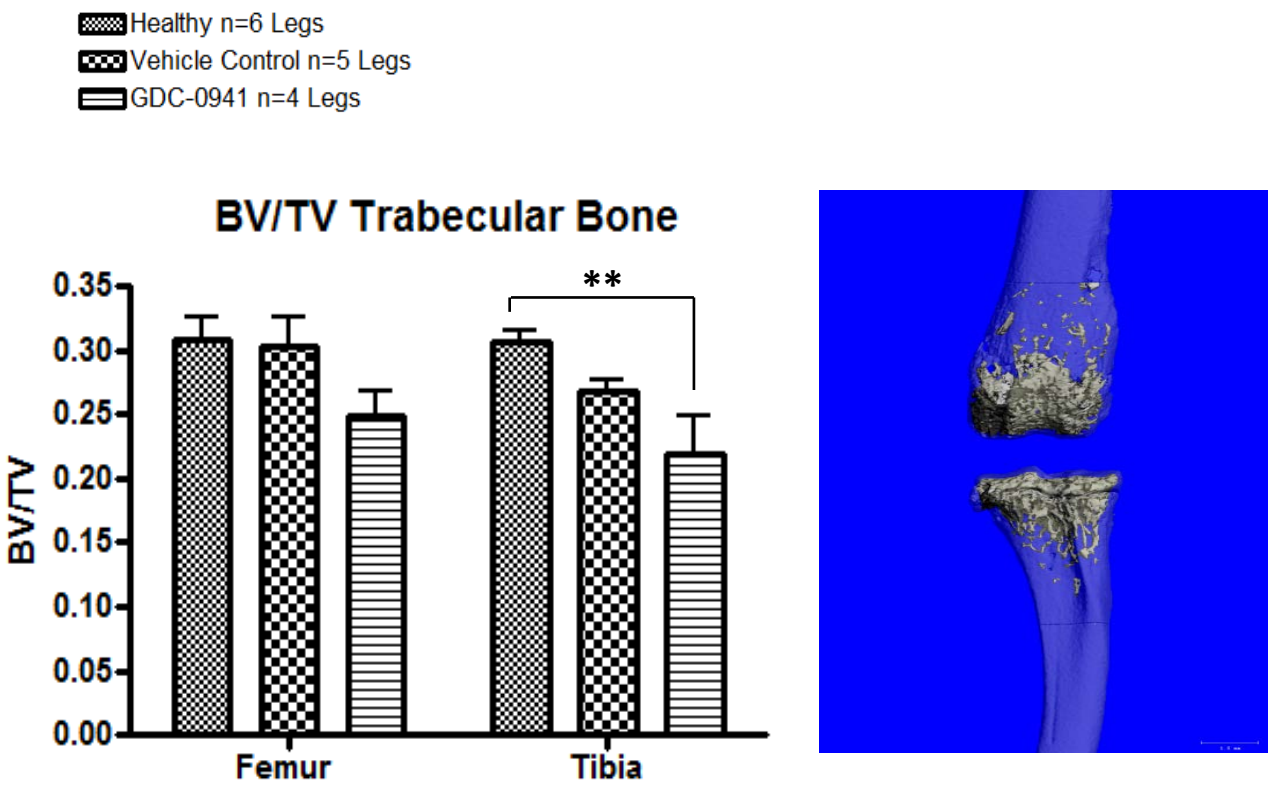

Figure 3.3-7 Quantification of trabecular bone volume for femurs and tibias using µCT.

Mice undergoing GDC-0941 and vehicle control treatment were sacrificed on day 21 after intracardiac injection of MDA-MB-231/EGFP-Luc2 cells, and their limbs examined by µCT. Limbs from healthy mice were also examined by µCT as a control. 3D reconstructed images and analyses were completed on a 2.5 mm region of the distal femur growth plate and the proximal tibia growth plate. (A) Evaluation of trabecular bone volume/ total bone volume (BV/TV). Statistical analyses were performed using two-way ANOVA in GraphPad Prism, and value of $P < 0.05$ were considered statistically significant. **p<0.01. (B) A representative 3D image of the trabecular bone for both the femur and tibia of mouse with osteolytic metastases that was treated with GDC-0941.

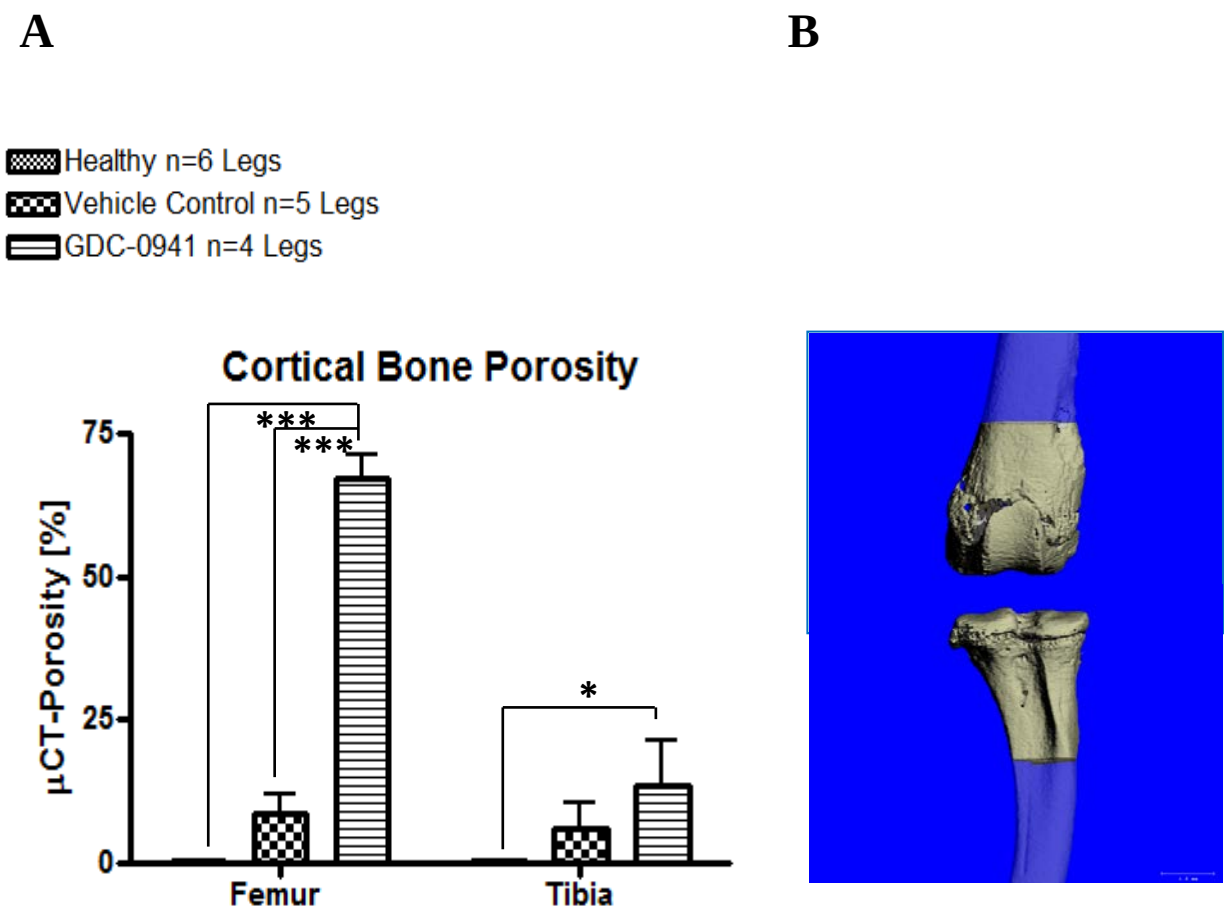

Figure 3.3-8 Quantification of cortical bone porosity for femur and tibia using µCT.

Refer to image 3.3-7 for a more detailed description. (A) Evaluation of the percentage of cortical bone porosity. Statistical analyses were performed using two-way ANOVA in GraphPad Prism, and values of $P < 0.05$ were considered statistically significant. * $p < 0.05$ and ***$p < 0.001$. (B) A representative 3D image of the surface femur and tibia of mouse with osteolytic metastases that was treated with GDC-0941.

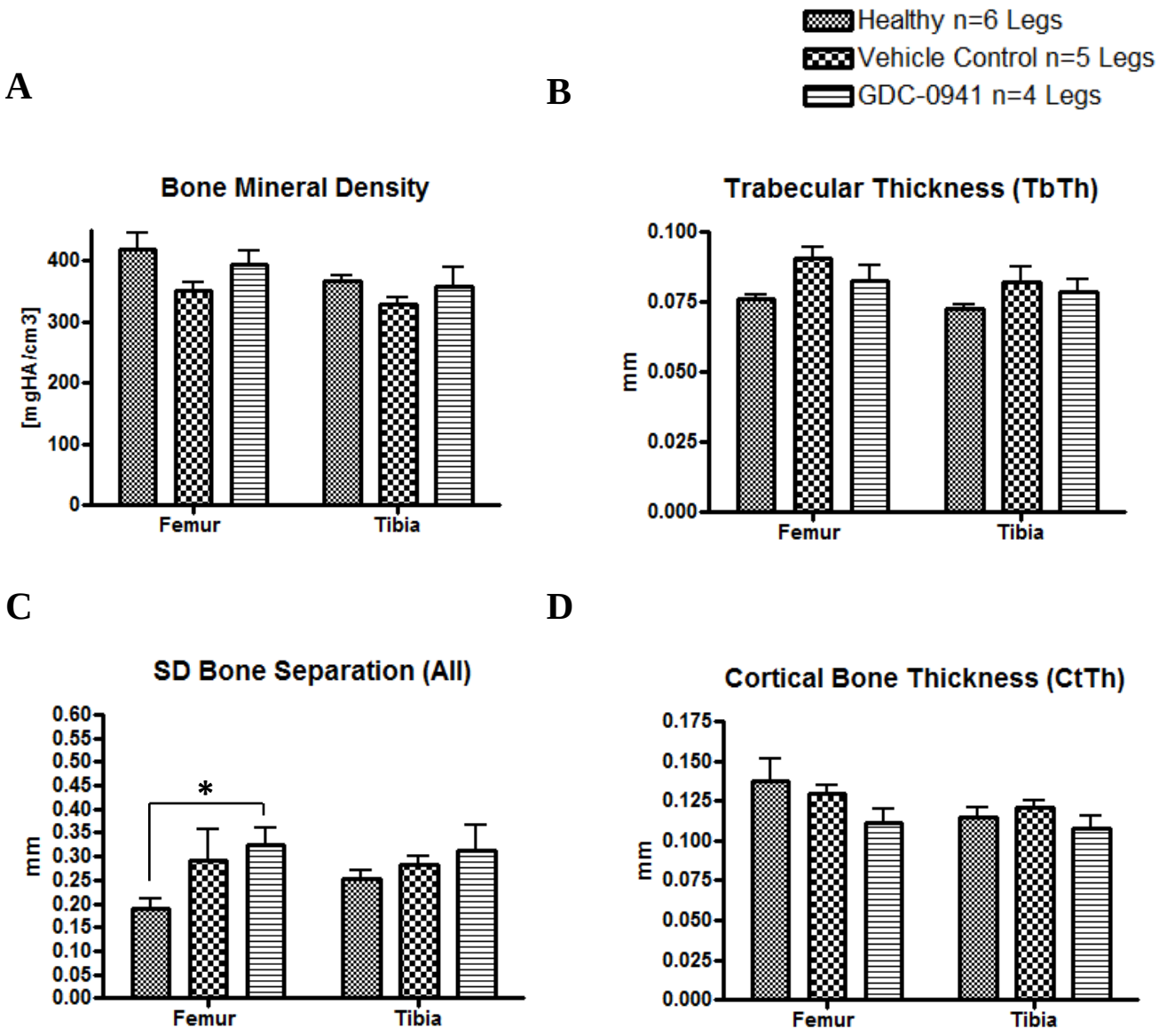

Figure 3.3-9 µCT parameters for femur and tibia.

Refer to image 3.3-7 for a more detailed description. (A) A representative of bone mineral density analysis for legs collected from healthy mice, mice with osteolytic metastases that were treated with GDC-0941, and control mice with osteolytic metastases. (B) A trabecular bone thickness analysis of femurs and tibias. (C) A standard deviation analysis for the femur and tibia bone separation. (D) A cortical bone thickness analysis of the femur and tibia. Statistical analyses were performed using two-way ANOVA in GraphPad Prism, and the value of $P < 0.05$ were considered statistically significant. * $p < 0.05$.

A

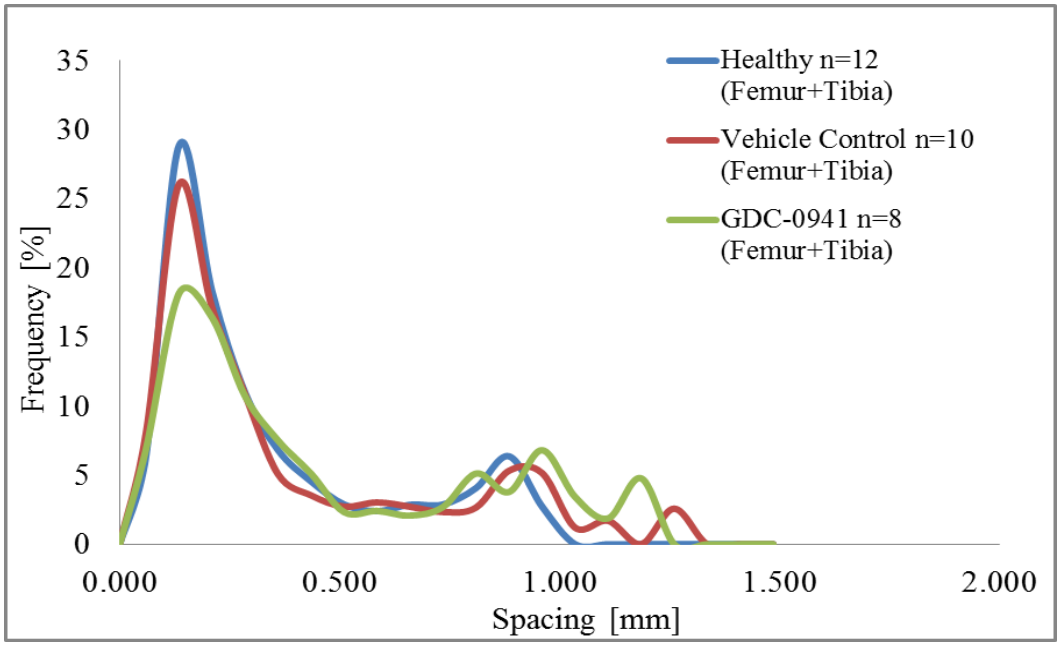

B

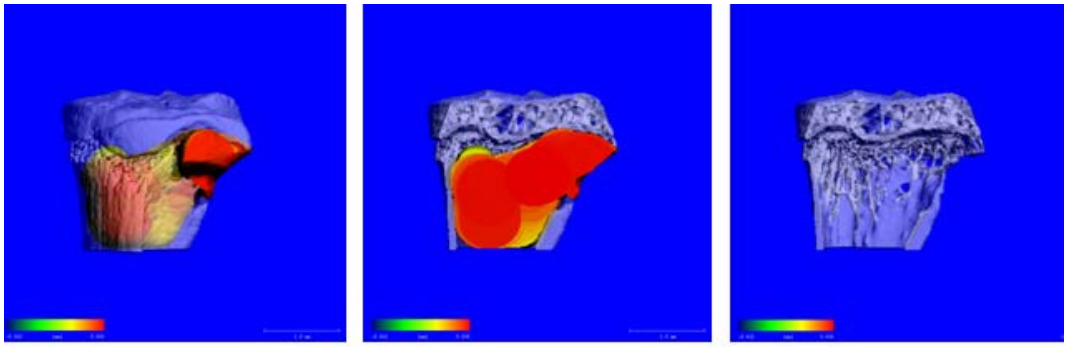

Figure 3.3-10 µCT void measurement analysis within the bone.

Refer to image 3.3-7 for a detailed description. Spheres were measured within the bone for both the femurs and tibias. (A) A representative graph for frequency of spheres with different spacing for tibias and femurs collected from healthy mice, mice with osteolytic metastases that were treated with GDC-0941, or vehicle control mice with metastases. (B) Representative image of a tibia from drug treated group subjected to the sphere analysis. The color scale represents the size of the sphere. Red spheres represent large spaces and blue spheres represent small spaces.

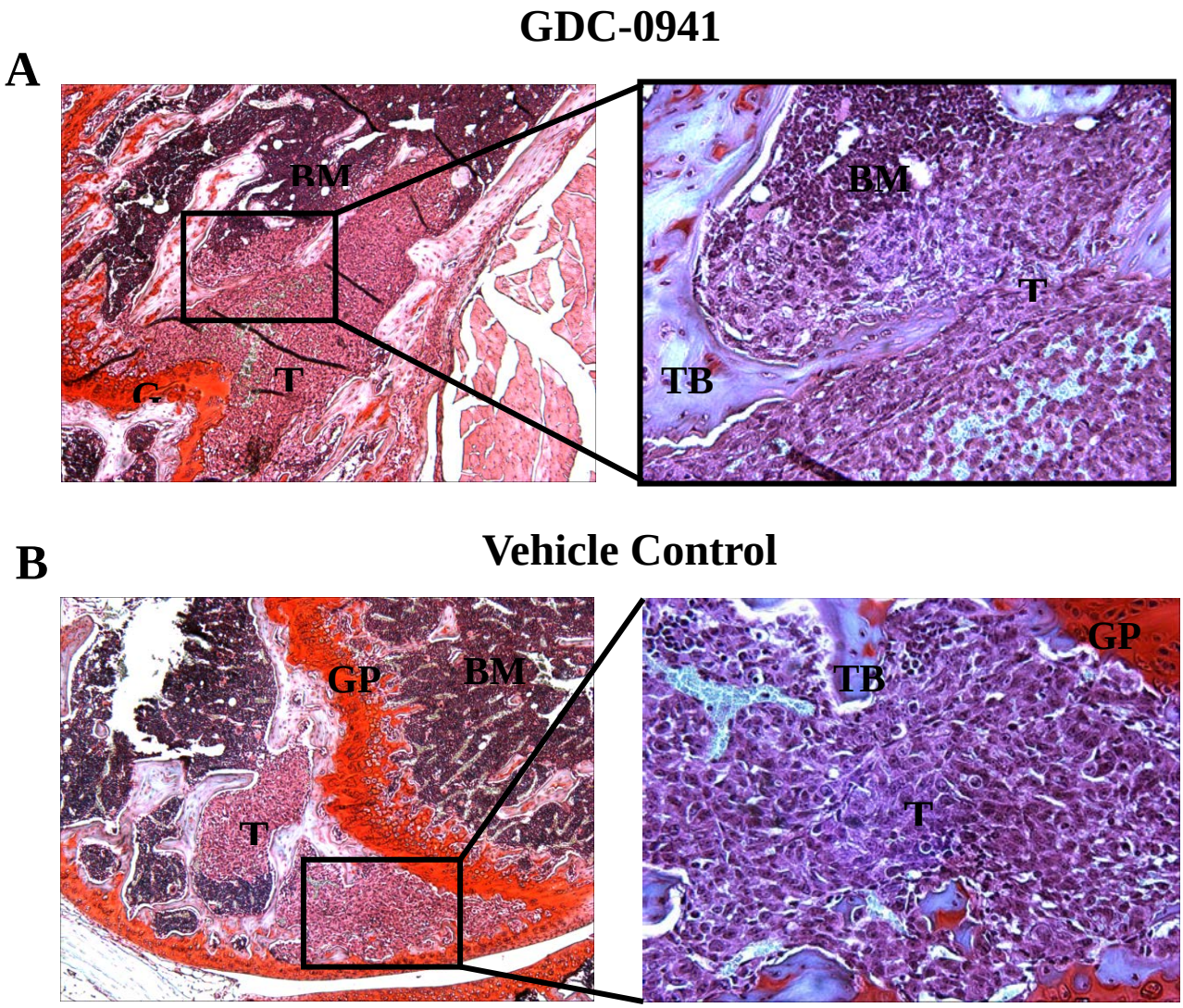

Figure 3.3-11 Trichrome stain of osteolytic metastases from GDC-0941 treated and vehicle control mouse bones.

Mice with bone lesions treated with GDC-0941 or vehicle control from day 14-21. Image A and B represent the trichrome stained sections of a representative knees from vehicle control and GDC-0941 treated mice, respectively. Growth plate (GP), trabecular bone (TB), bone marrow (BM), and tumour area (T). Images on the left were taken at 5x magnification and images on the right were taken at 20x magnification.

3.4 Discussion

Here we found no evidence that GDC-0941 was able to inhibit the growth of MDA-MB-231/EGFP-Luc2 osteolytic metastases. *In vitro* and *in vivo* western blot analyses confirmed that GDC-0941 was able to inhibit the PI3K pathway as shown by its ability to prevent the phosphorylation of AKT (Fig 3.3-1 and 3.3-2). In H1299 tumours, the level of phospho-AKT was significantly lowered for drug treated mice compared to vehicle control treated mice. These results confirm that the GDC-0941, at the concentration used *in vivo*, was able to inhibit the PI3K/AKT pathway. In keeping with this result, GDC-0941 did not show any detectable effect on MDA-MB-231/EGFP-Luc2 cell proliferation in the MTT asssay (Fig 3.3-3). The *in vitro* results obtained with the MTT assay were consistant with the BLI data that also showed that GDC-0941 did not have an inhibitory effect on the growth of bone metastases (Fig 3.3-4, 5, and 6). This was expected considering that MDA-MB-231/EGFP-Luc2 show very low basal levels of PI3K/AKT pathway activity *in vitro*. Even though GDC-0941 had no effect on the tumour growth, the potential effect of this drug on osteoclasts was further indirectly evaluated by µCT since osteoclasts are responsible for osteolytic metastatic lesions. Overall, most µCT bone parameters did not show any difference between GDC-0941 and vehicle control treated mice. Indeed, a significant difference was seen not between vehicle control and healthy mice despite the presence of osteolytic metastases in the vehicle treated mice, thus attesting to the relative insensitivity of the µCT assay methods used. The one significant difference observed (Fig 3.3-7) may was likely due to the presence of larger tumours in the bone of GDC-0941 treated mice as compared to the vehicle treated mice. This was

also supported by the finding that mice with treated osteolytic metastases had a significant increased level of femur cortical bone porosity compared to vehicle controls (Fig 3.3-8). Although we hypothesized that GDC-0941 would inhibit osteoclast activation/differentiation and lead to less osteolytic metastatic lesions, our results did not bear this out. Furthermore according to the μCT void measurement technique there were much larger spheres present in the femur and tibia of GDC-0941 treated osteolytic metastases mice as compared to vehicle treated mice (Fig 3.3-10). This indicated that there were larger empty spaces corresponding to regions of bone destruction present within the bone of GDC-0941-treated animals. Thus, the possibility existed that GDC-0941 was actually promoting bone destruction or inhibiting osteoblastic activity, or a combination of the two.

3.5 Conclusions

In summary, GDC-0941 had no effect on the growth of either MDA-MB-231/EGFP-Luc2 cells *in vitro* or bone metastases. This conclusion was drawn from MTT assay and BLI studies. μCT, on the other hand, suggested that GDC-0941 may have actually augmented bone loss in the presence of osteolytic metastases. The reasons for this unexpected effect is unclear, however, it is possible that GDC-0941 was ineffective at decreasing osteoclast function, while at the same time exerting an inhibitory effect on osteoblast-activating bone formation and/or survival. The tumour environment provides a variety of osteoclast-activity factors (IL-11, IL-8, RANKL, PTHrP, PGE-2), and hence interruption of a single signaling pathway such as that downstream of PI3K, may be

insufficient to block osteolysis. The observed ineffectiveness of GDC-0941 against osteolysis prompted a change in research direction.

Chapter Four: Comparing the therapeutic effect of DMXAA on MDA-MB-231/EGFP-Luc2 derived osteolytic metastases and subcutaneous tumours.

4.1 Aim

This chapter describes a study of the therapeutic effect of the vascular disrupting agent, DMXAA, on MDA-MB-231/EGFP-luc2 derived osteolytic metastases and subcutaneous tumours.

4.2 Background

The ability to recruit and expand new blood vessels is an essential component of tumour growth [39]. Because the growth and survival of tumours is crucially dependent on a functional blood supply, strategies that specifically target the vasculature to deprive the tumours vital nutrients provide an attractive approach for cancer therapy [44]. The vascular disrupting approach is one of the methods used to target endothelial cells within tumours [45-48]. Vascular disrupting agents (VDAs) supress tumour growth through the induction of vasculature collapse, leading in turn to hypoxia and tumour necrosis [53]. DMXAA is one of the most advanced vascular disrupting agents (VDA) in clinical trials and is now in phase III clinical trials for non-small cell lung cancer (NSCLC) [53, 58]. This agent has shown promising effects in preclinical *in vivo* studies where it was shown to produce hemorrhagic necrosis and growth delay of many different tumour types [59, 60]. DMXAA has also shown an ability to enhance tumour cell death by 10-500 fold when given in combination with chemotherapy drugs such as cisplatin or

cyclophosphamide (CP) as compared to chemotherapy alone in rodent tumour models of human breast and ovarian cancers [61]. However, despite positive results observed in preclinical studies, this drug has not lived up to its potential in human clinical studies [58, 79]. For example, a large Phase III clinical trail for advanced non-small-cell lung cancer showed that the addition of DMXAA to standard chemotherapeutic drug treatments failed to improve survival [79]. Recently, it was also shown that DMXAA failed to improve overall survival of patients with advanced NSCLC when given both as first-line and second-line therapy [58]. Thus there are conflicting results between pre-clinical findings with DMXAA and later clinical trails. Interestingly, our results (see DMXAA-treated osteolytic metastases, chapter 5) were also conflict with previously published pre-clinical studies using DMXAA [58, 79]. Using BLI as a measure of tumour damage we found that osteolytic metastases responded poorly to DMXAA treatment, raising the question as to why there was such a discrepancy between our results (chapter 5) and the DMXAA results previously reported in the literature [58]. Answering this question could potentially explain the negative results obtained in the human clinical trials.

Since the majority of the DMXAA pre-clinical studies used mouse models with subcutaneous or orthotopic tumours, we decided to compare DMXAA responses of MDA-MB-231/EGFP-Luc2-derived subcutaneous tumours and osteolytic metastases [60, 80, 81]. The main goal of this study was to determine whether there would be a difference in the therapeutic effect of DMXAA on MDA-MB-231/EGFP-Luc2 osteolytic metastases versus subcutaneous tumours. We hypothesized that osteolytic metastases would respond differently to DMXAA treatment compared to the subcutaneous tumours.

4.3 Results

4.3.1 Studying the effect of DMXAA on subcutaneous and metastatic tumours using bioluminescence imaging

In order to compare the effects of DMXAA in different *xenografted* tumours, both bone metastases and subcutaneous tumours were generated. MDA-MB-231/EGFP-Luc2 cells were injected into 5 wk-old NIH-III athymic (nude/beige) mice either subcutaneously, or by intracardiac (IC) injection to obtain bone lesions. After tumours had developed, mice were treated with 25 mg/kg DMXAA (as a single dose given on day 21) to study the effects of this agent on the tumours. In accordance with previous studies using DMXAA [48, 59, 67], the subcutaneous tumours showed a strong response to the administration of DMXAA. This was indicated by a marked decrease in bioluminescence signals at both 6 and 24 hours post-injection (Fig 4.3-1, 2). The bioluminescene signals decreased by 2 logs after 6 hrs of DMXAA treatment (Fig 4.3-2 A). Alternatively, when DMXAA was administered to mice with established bone metastases, there was no statistically significant decrease in the bioluminescent signals (Fig 4.3-3, 4) indicating that the drug was not as effective on these tumours. Thus, DMXAA exhibited a discordant effect on MDA-MB-231/EGFP-Luc2 osteolytic metastases versus subcutaneous tumours (Fig 4.3-5), with established bone metastases showing very poor responses to DMXAA according to the BLI quantification (Fig 4.3-6).

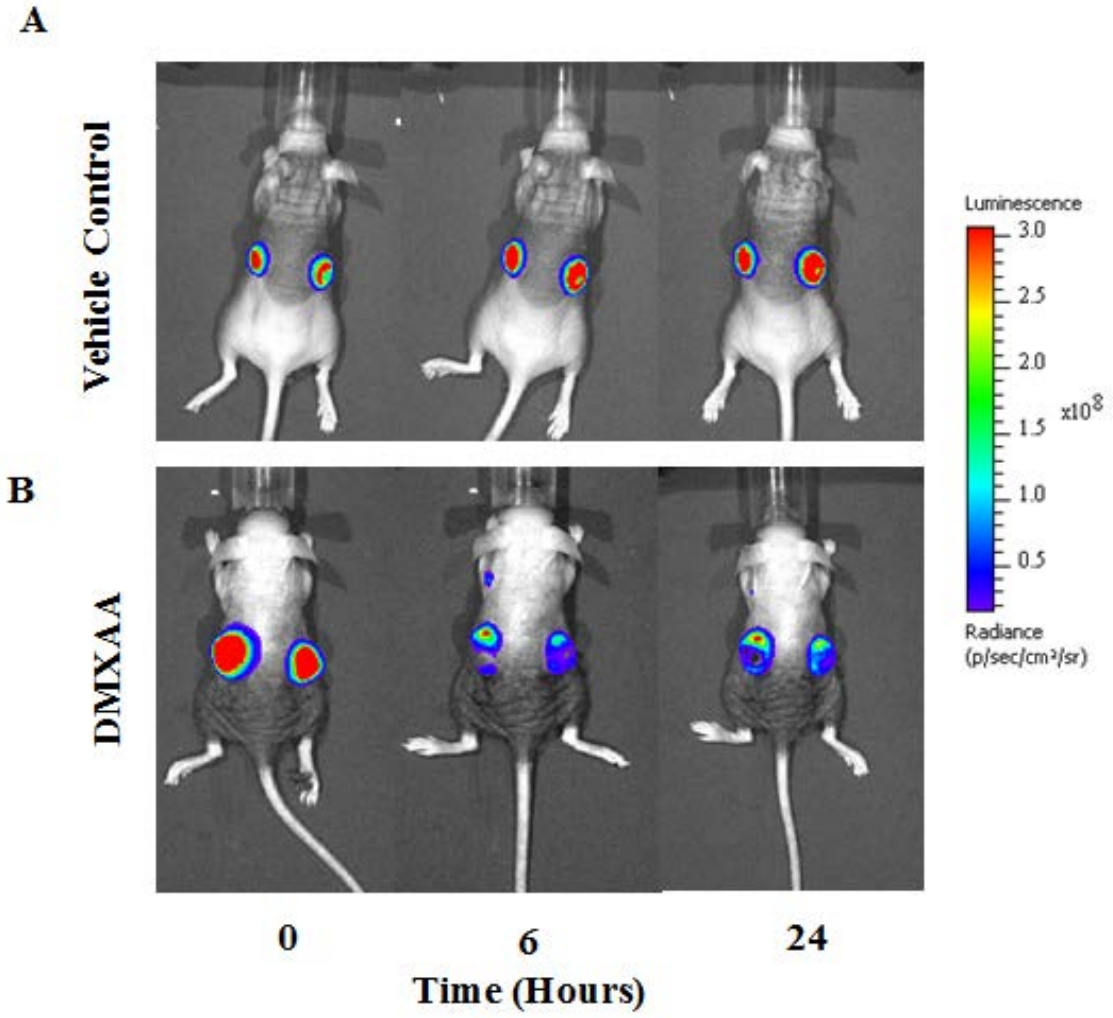

Figure 4.3-1 Subcutaneous tumour growth *in vivo* measured using BLI.

BLI was performed after subcutaneous injection of MDA-MB-231/EGFP-Luc2. Mice were then treated one time with DMXAA or vehicle control on day 21 and bioluminescence measured at the indicated time points. Representative dorsal images of a vehicle control treated mouse (A) and DMXAA treated mouse (B) 0, 6, and 24 hrs post-treatment. Scales are in photon /s /cm^2.

A **B**

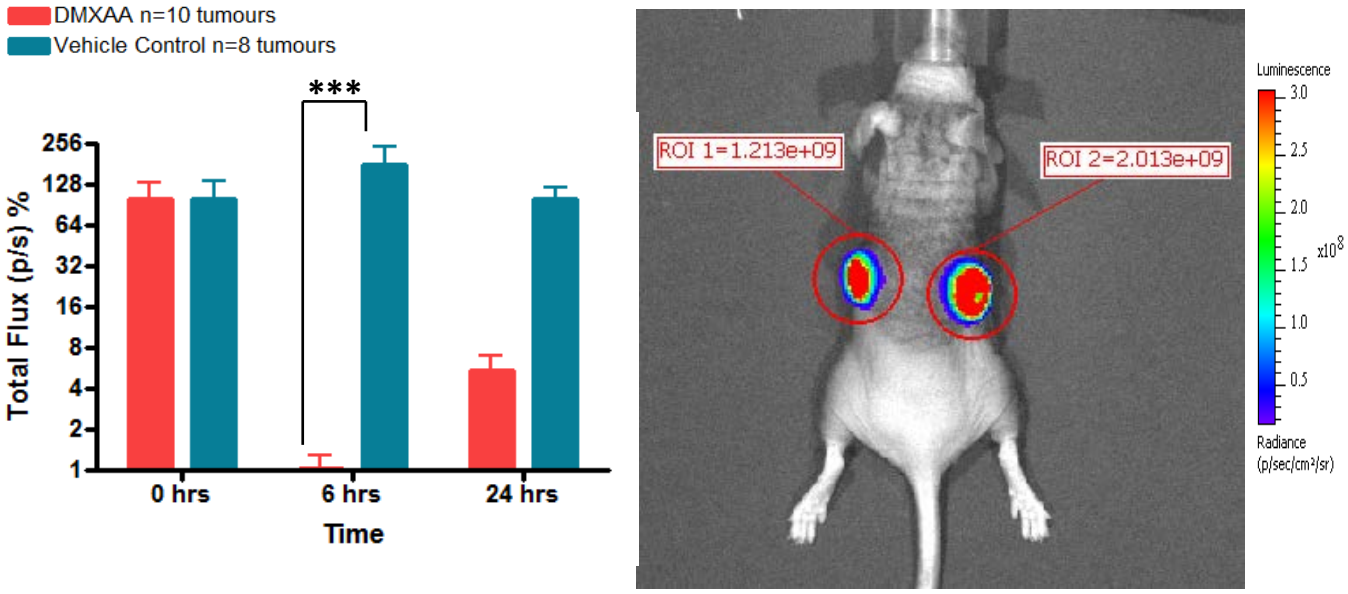

Figure 4.3-2 Quantification of the subcutaneous tumour bioluminescence intensities of DMXAA and vehicle control treated mice.

(A) Bioluminescence intensities of subcutaneous tumours from DMXAA treated and vehicle control mice measured 0, 6 and 24 hrs post-treatment. To measure the tumour's bioluminescence, the region of interest (ROI) with width of 30 (pix) and height of 30 (pix) were measured for each tumour in the dorsal position. Tumour bioluminescence was quantified as a mean photon/s ± SEM. The error bars represent bioluminescence intensities of 10 tumours (n=10) from DMXAA treated mice and bioluminescence intensities of 8 tumours (n=8) from vehicle control mice. Total flux values representing bioluminescence were baseline corrected and graphed using GraphPad Prism 4.0 Software. Statistical analyses were performed using two-way ANOVA in GraphPad Prism and a value of $P<0.05$ was considered statistically significant, ***$p<0.001$. (B) A representative image of a mouse in the dorsal position showing the ROI used to evaluate the growth rate of the subcutaneous tumour illustrated.

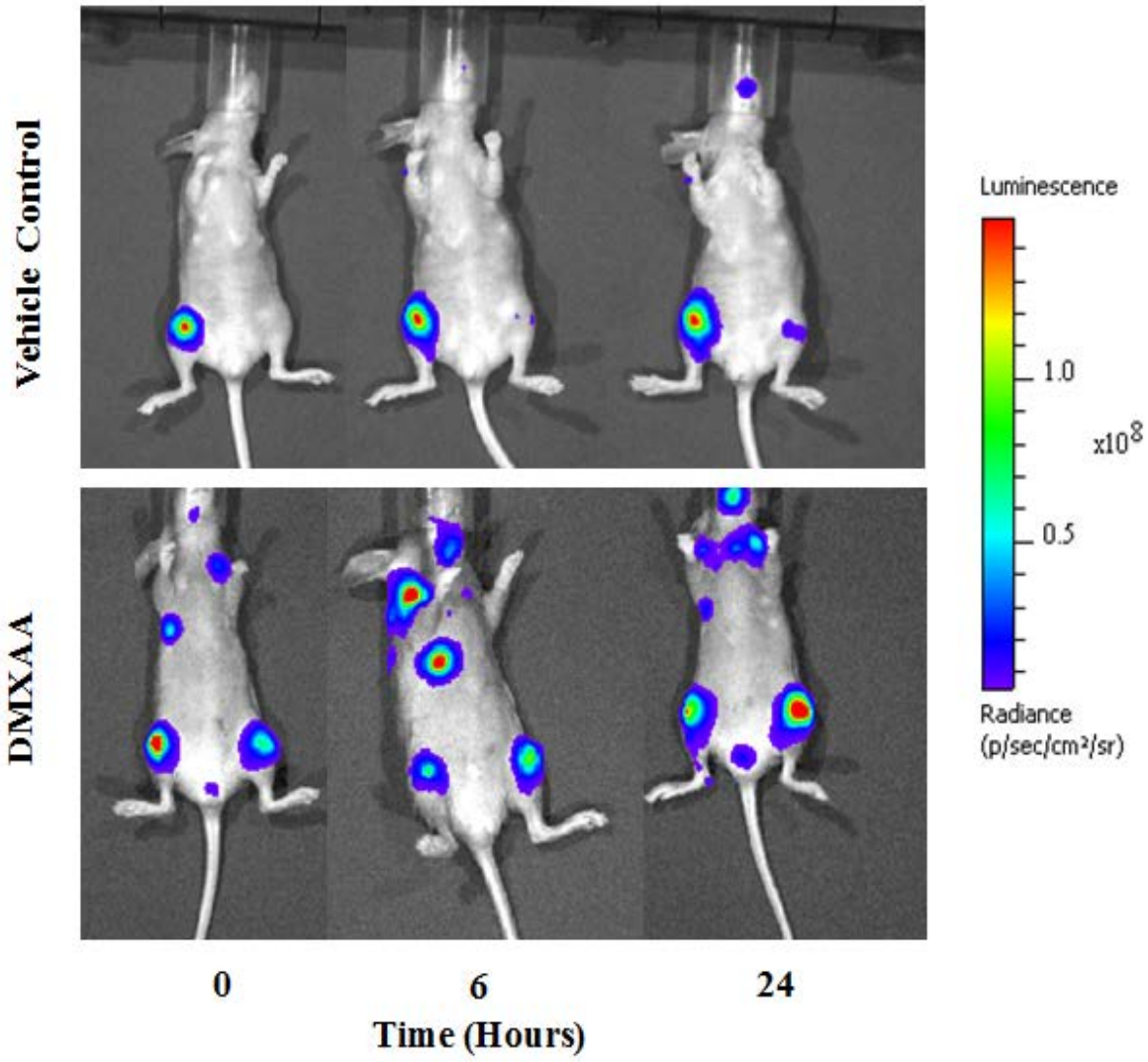

Figure 4.3-3 Measuring the growth of osteolytic metastases *in vivo* using BLI.

Bone metastases were generated via intracardiac injection of the MDA-MB-231/GFP-Luc2 cells. Mice were then treated one time with DMXAA or vehicle control on day 21 and bioluminescence measured at the indicated time points. Representative images of mice in ventral position from the vehicle control-treated group (A) and DMXAA-treated group (B) 0, 6, and 24 hrs post-treatment. Scales are in photon /s /cm^2. Tumour bioluminescence, a measure of tumour burden, is presented in this image to show the location of the tumour and the growth rate for both a DMXAA treated and a vehicle control mouse.

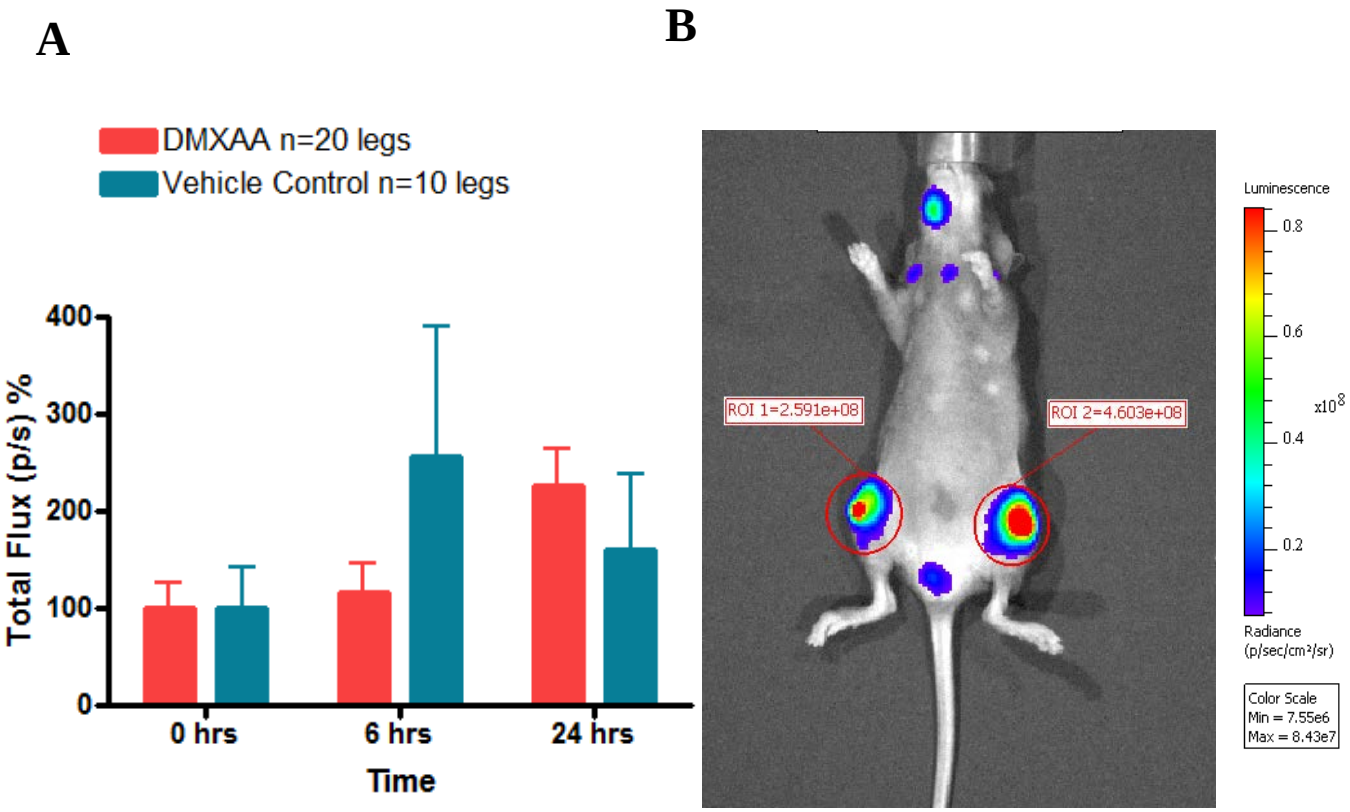

Figure 4.3-4 Quantification of the osteolytic metastases bioluminescence of DMXAA and vehicle control treated mice.

(A) Bioluminescence of knee metastases from DMXAA and vehicle treated mice measured at days 6 and 24 hours following DMXAA treatment. To measure tumour bioluminescence, the regions of interest (ROI) with width of 25 (pix) and height of 25 (pix) were measured for each from osteolytic tumour in the ventral position. Tumour bioluminescence was quantified as a mean photon/s ± SEM. BLI values were used to evaluate tumour growth rates. The error bars represent bioluminescence intensities of 20 knees (n=20) from DMXAA-treated mice and 10 knees (n=10) from vehicle control mice. Total flux values representing bioluminescence intensities were baseline corrected and graphed using GraphPad Prism 4.0 Software. Statistical analyses were performed using two-way ANOVA in GraphPad Prism and value of $P<0.05$ was considered statistically significant. (B) A representative image of a mouse in a ventral position showing the ROIs used to evaluate the growth rate of two osteolytic metastases.

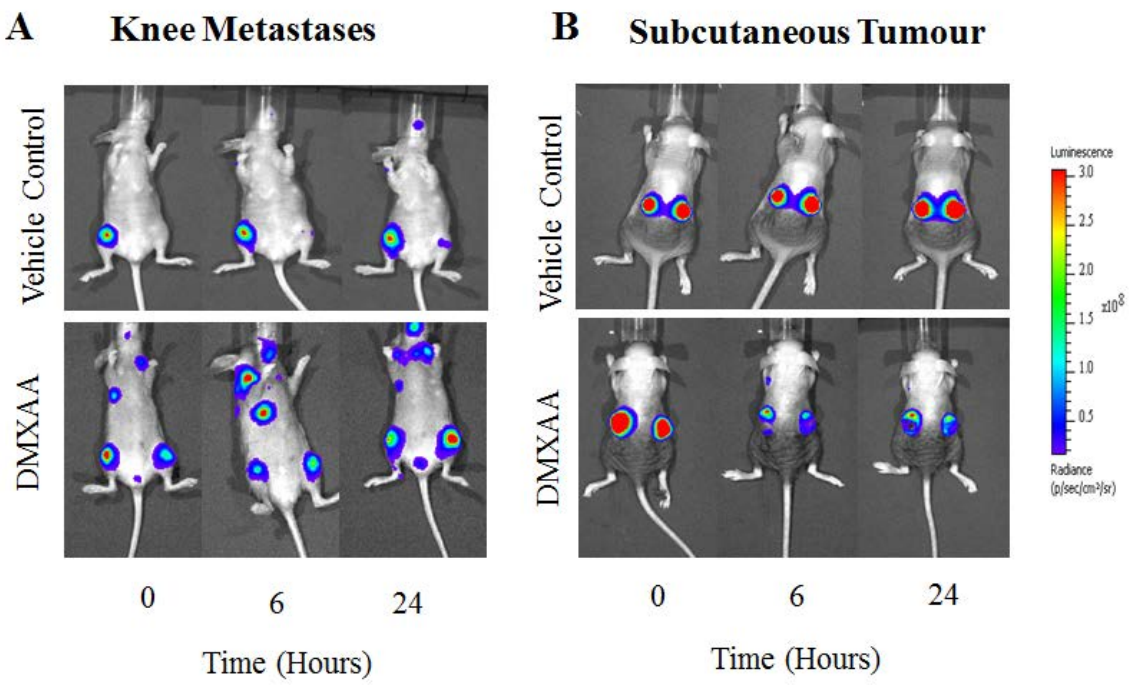

Figure 4.3-5 Comparing BLI of MDA-MB-231/EGFP-Luc2 breast cancer cell line-dervied osteolytic metastases and subcutaneous tumours in response to DMXAA treatment.

Bone metastases and subcutaneous tumours were generated as was explained in Figures 5.3-2 and 4. (A) Representative images in the ventral position of vehicle control and DMXAA-treated bone metastases at 0, 6, and 24 hrs post-treatment. (B) Representative images in the dorsal position of vehicle control and DMXAA-treated subcutaneous tumours at 0, 6, and 24 hrs post-treatment. Scale bar are in photon /s /cm^2.

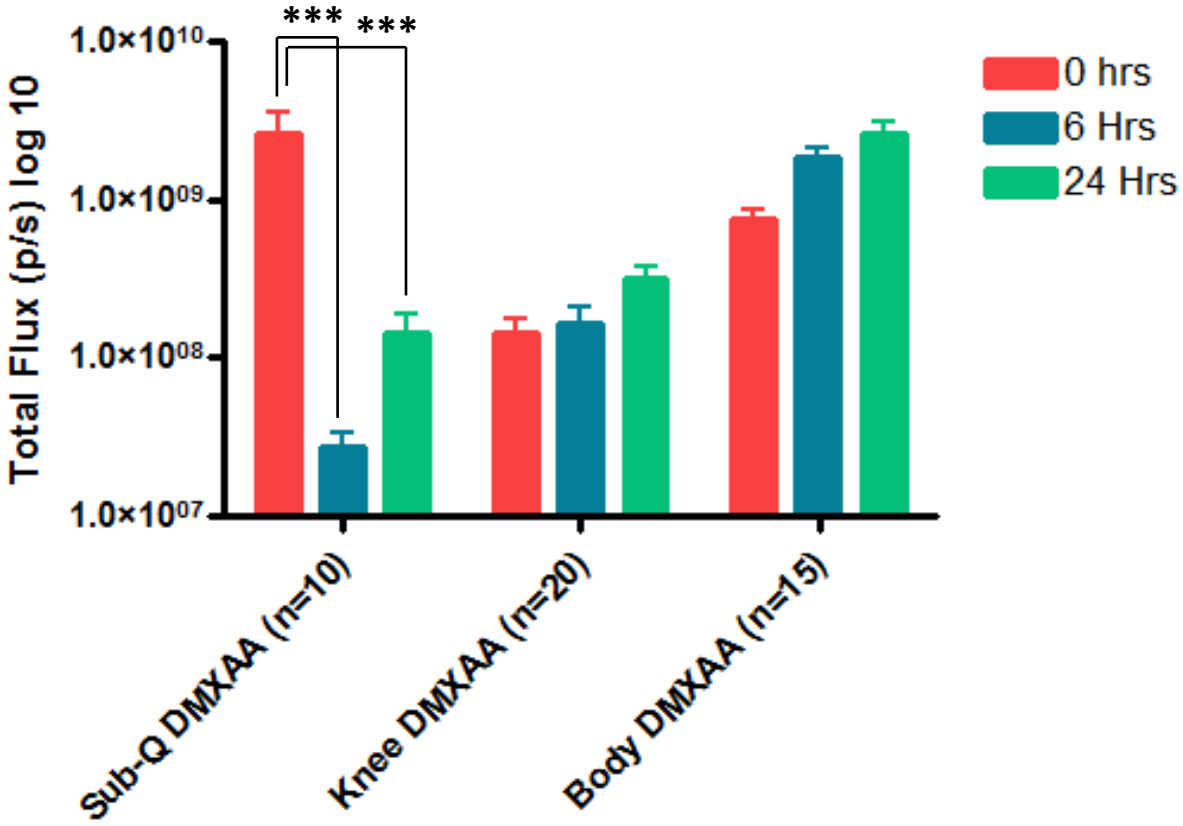

Figure 4.3-6 Comparing BLI quantification for MDA-MB-231/EGFP-Luc2 breast cancer cell line-induced osteolytic metastases and subcutaneous tumours after DMXAA treatment.

Bone metastases and subcutaneous tumours were generated as described in for Figures 5.3-2 and 4. This figure shows BLI measurments for both models, subcutaneous and osteolytic tumours, and whole-body from osteolytic metastasis mouse model at 0, 6, and 24 hrs post-treatment with DMXAA. Total flux values representing bioluminescence intensities were graphed using GraphPad Prism 4.0 Software. One-way ANOVA, Newman-Keuls test was used for statistical analyses and a value of $P<0.05$ was considered statistically significant. ***$p<0.001$.

4.3.2 Subcutaneous tumour histological analysis

Subcutaneous tumour histological examination at 24 hrs post DMXAA treatment demostrated a strong induction of the characteristic hemorrhagic necrosis that left only a thin rim of viable tumour cells (Fig 4.3-7 B). In contrast, the osteolytic metastases after 24 hrs post-DMXAA treatment revealed variable response to this drug. Thus, in the 4 samples analyzed, there were regions of necrosis and hemorrhages were present, but these varied considerably (labelled as N and H in Fig 4.3-8 B, C). Some areas of the tumour were unaffected, while other area showed a substantial rim of viable cells. The latter likely accounted for the relative preservation of bioluminescence post-DMXAA treatment. Thus, in contrast to the dramatic responses seen in DMXAA-treated subcutaneous tumours (Fig 4.3-7), the bone metastases were relatively refractory, suggesting that DMXAA was not as effective on the metastatic tumours.

4.4 Discussion

Using BLI, we compared the responses of subcutaneous and metastatic tumours to DMXAA and found that this drug causes massive necrosis in the subcutaneous tumours. In contrast, DMXAA showed no significant effect of bone metastasis. This was confirmed by histological analysis that showed a massive generalized increase in necrosis in DMXAA-treated subcutaneous tumours. Hemorrhagic necrosis was also seen within the H&E stains for osteolytic metastases after DMXAA treatment, but the effect of this drug was not nearly as dramatic as that seen in the subcutaneous tumours. In summary,

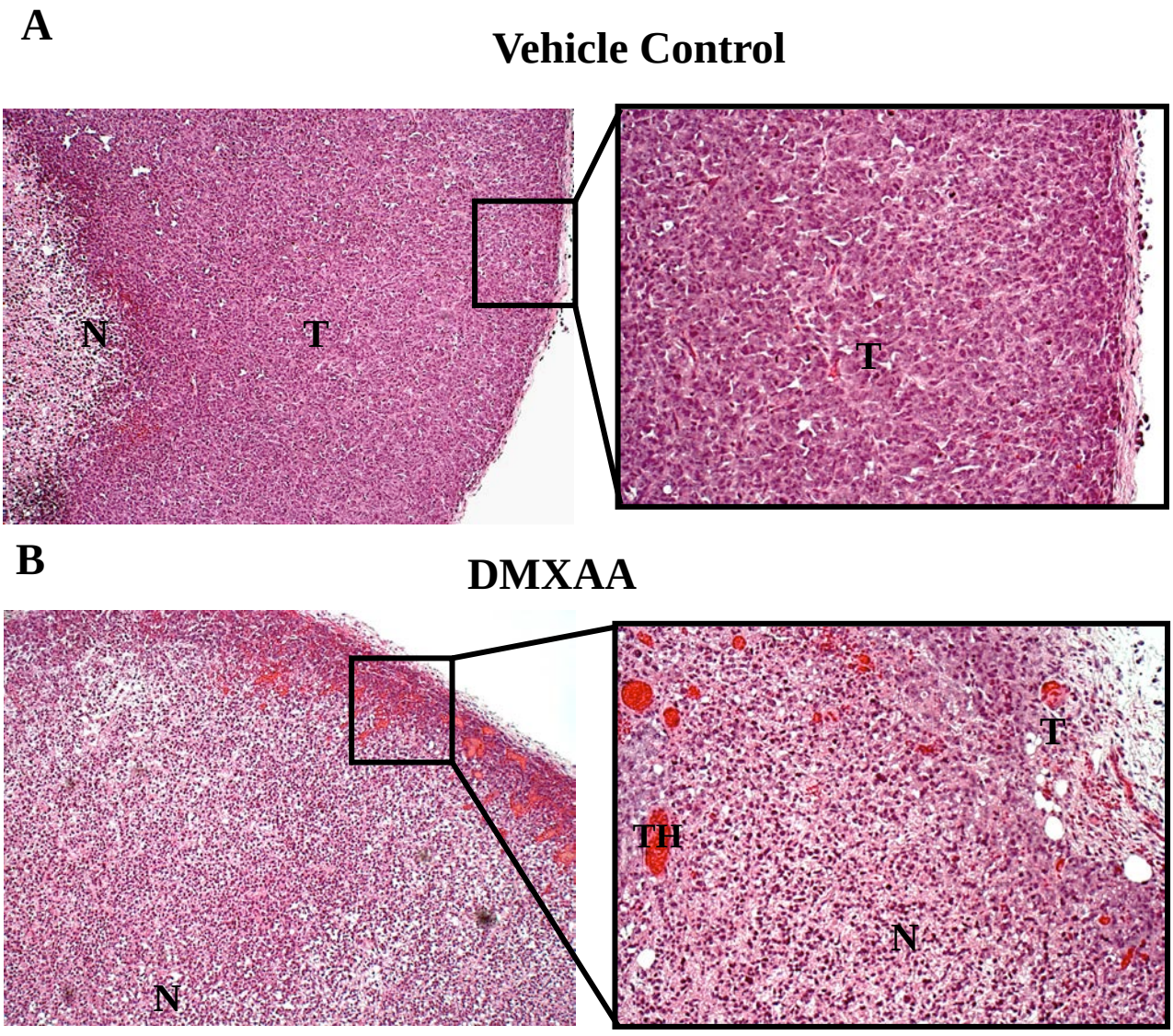

Figure 4.3-7 H&E staining of subcutaneous tumours treated with DMXAA or the vehicle control.

Mice with established MDA-MB-231/EGFP-Luc2 derived subcutaneous tumours were treated with a single dose of DMXAA, or vehicle control, and sacrificed 24 hrs later for histological analysis. (A & B) Representative H&E stained sections of tumours from vehicle control and DMXAA treated mice, respectively. Tumour area (T), necrosis (N), and vessel thrombosis. Images on the left were taken at 5x and images on the right were at 20x magnification.

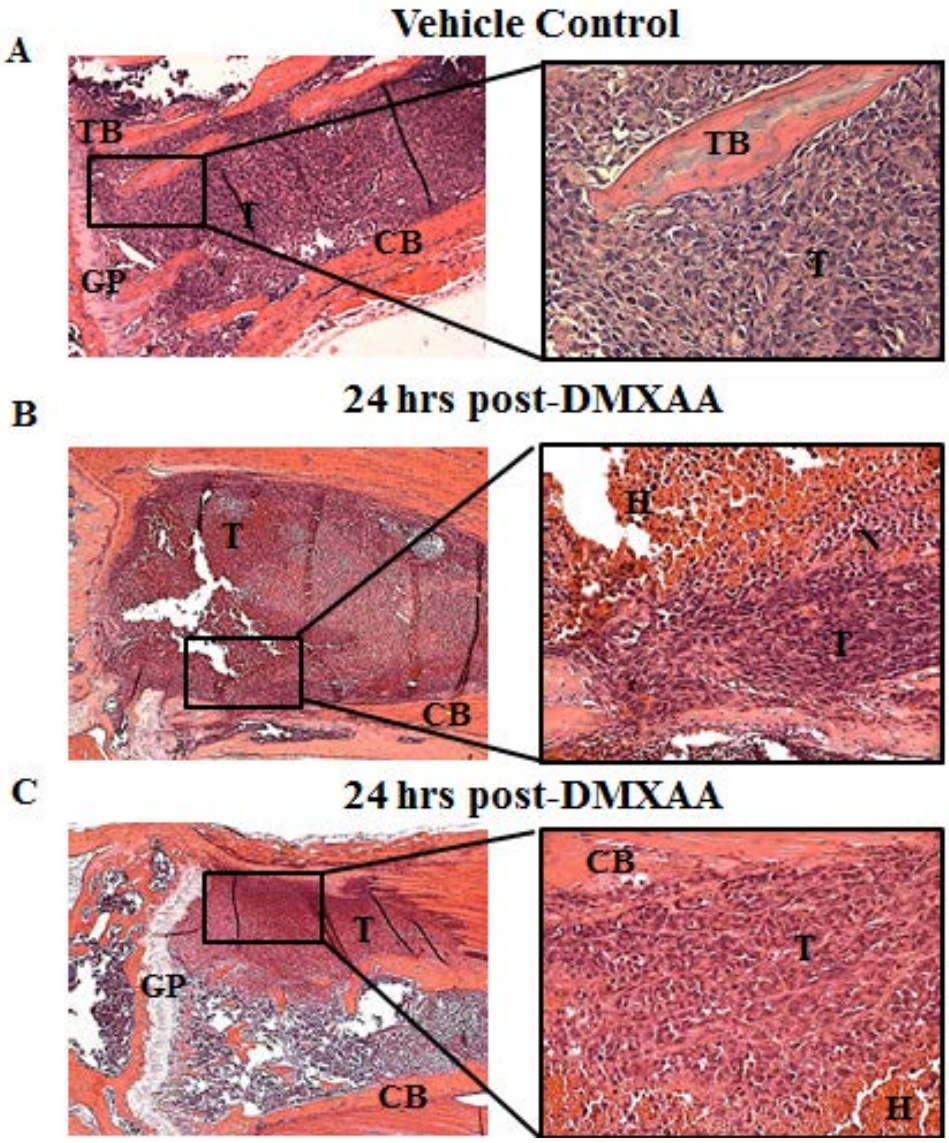

Figure 4.3-8 H&E staining of subcutaneous tumours treated with DMXAA or the vehicle control at 24hrs post-drug administration.

Mice with day 21 post MDA-MB-231/EGFP-Luc2 injection osteolytic metastases were treated with one-time dose DMXAA, or vehicle control, and sacrificed 24 hrs later to collect limbs for histology. A representative image of H&E stains section of vehicle control (A) and 24 hrs post-DMXAA treated (B &C). Tumour area (T), necrosis (N), hemorrhage (H), growth plate (GP), cortical bone (CB). Images on the left were taken at 50x magnification, images on the right were taken 200x. The osteolytic metastases after 24 hrs post-DMXAA treatment revealed variable response to this drug. There were regions of necrosis and hemorrhages were present, but these varied considerably.

BLI results obtained thus far confirmed that DMXAA promoted necrosis MDA-MB-231/EGFP-Luc2 subcutaneous tumours but not of osteolytic metastases. This finding may be in keeping with the discordance between the pre-clinical findings and later clinical trials in human. The discordant effects may be due to a difference between the vessels within subcutaneous and metastatic tumours which may affect responses to DMXAA (see chapter 6 for possible reasons for this discordance).

4.5 Conclusion

DMXAA shows relatively discordant effects on MDA-MB-231/EGFP-Luc2 breast cancer cell line-induced osteolytic metastases when compared with subcutaneous tumours.

Chapter Five: Investigating the ability of a PI3K inhibitor to augment the effect of DMXAA on bone metastases.

5.1 Aim

This chapter concerns a study of the effect of the vascular disrupting agent, DMXAA, either alone, or in combination with the pan-PI3K inhibitor, GDC-0941, on the growth of established osteolytic metastases. We hypothesized that PI3K inhibition would augment the vascular disrupting effects of DMXAA.

5.2 Background

In this study we used DMXAA either alone, or in combination with GDC-0941, to treat osteolytic metastases. It was expected that targeting the tumour vasculature with the vascular disrupting agent, DMXAA, would damage the tumour vasculature and lead to a decrease in tumour viability. Interestingly, the VDA we used was shown to be primarily effective against poorly vascularized tumour centers, and this is why DMXAA leads to necrosis within the center of tumours, often leaving a surviving rim of viable cells [53]. DMXAA showed a greatly reduced effect on bone metastasis when compared with subcutaneous tumours (chapter 4). Thus, in order to try to enhance DMXAA's effect on osteolytic metastases, we introduced combinational treatment with a drug, GDC-0941, targetting PI3K, a major survival pathway.

A strong rationale exists for combining a VDA, such as DMXAA, with a PI3K inhibitor, such as GDC-0941. Previous studies showed that activation of the PI3K/AKT pathway is

necessary for cells to tolerate the absence of nutrients and oxygen when angiogenesis has been inhibited [82]. In addition, this pathway plays a major role in counteracting the therapeutic efficacy of drugs that target tumour angiogenesis [82]. Thus, blocking the PI3K/AKT pathway with GDC-0941 during angiogenic inhibition would theoretically enhance the effect of DMXAA on the tumour vasculature. The PI3K/AKT pathway has also been shown to increase cell survival, growth, and proliferation of endothelial cells. Thus, inhibiting the PI3K/AKT pathway, a major anti-apoptotic pathway, with GDC-0941 could decrease endothelial cell survival, possibly enhancing the anti-vascular effects of DMXAA within bone metastasis.

5.3 Results

5.3.1 Studying the effect of DMXAA in vivo

BLI was carried out to monitor the *in vivo* effects of DMXAA on metastases.

5.3.1.1 Measuring the effect of DMXAA on tumours using bioluminescence imaging

We wanted to determine whether DMXAA on its own was able to reduce the growth of bone metastases by its effects on the tumour vasculature. Bone metastases were generated by intracardiac injection of MDA-MB-231/EGFP-Luc2 cells. Mice were then treated with a one-time dose of DMXAA or vehicle control on day 21 and BLI was performed from 6-120 hrs post-treatment (Fig 5.3-1). Images were collected and quantified for the knee and the whole-body bioluminescence to evaluate effect of DMXAA on photon

emission rates. Knee BLI measurements of mice post-treatment of DMXAA or vehicle control, did not show any detectable significant difference during the time-course (Fig 5.3-2). This was the same for the whole-body BLI measurements (Fig 5.3-3). BLI measurements for the knee and the whole body increased for both control and drug treated mice over time indicating DMXAA produced no significant effect on the growth of either bone or total metastases (Fig 5.3-2, 3).

5.3.1.2 Tumour morphological analysis

H&E staining of tissue sections was carried out to analyze the morphology of the osteolytic metastases post-DMXAA and vehicle control treatments at 120 hrs. Tumour area (T), necrosis (N), hemorrhage (H), growth plate (GP), trabecular bone (TB), and cortical bone (CB) were visualized (Fig 5.3-4). In the 8 samples analyzed, representative examples show that regions of necrosis were present (labelled as N in Fig 5.3-4) within the bone metastases tumours of a DMXAA treated mouse as compared to the vehicle treated control. However, some tumours lacked necrosis, while others with necrotic center still had thick viable tumour rims. These results explain why there was only a non-significant documented trend in BLI of DMXAA-treated bone metastases.

5.3.2 Studying the effect of GDC-0941 and DMXAA combinational treatment in vivo

BLI was carried out to monitor sites of soft tissue metastases and bone metastases following *in vivo* DMXAA and GDC-0941 combinational treatment. H&E stains were

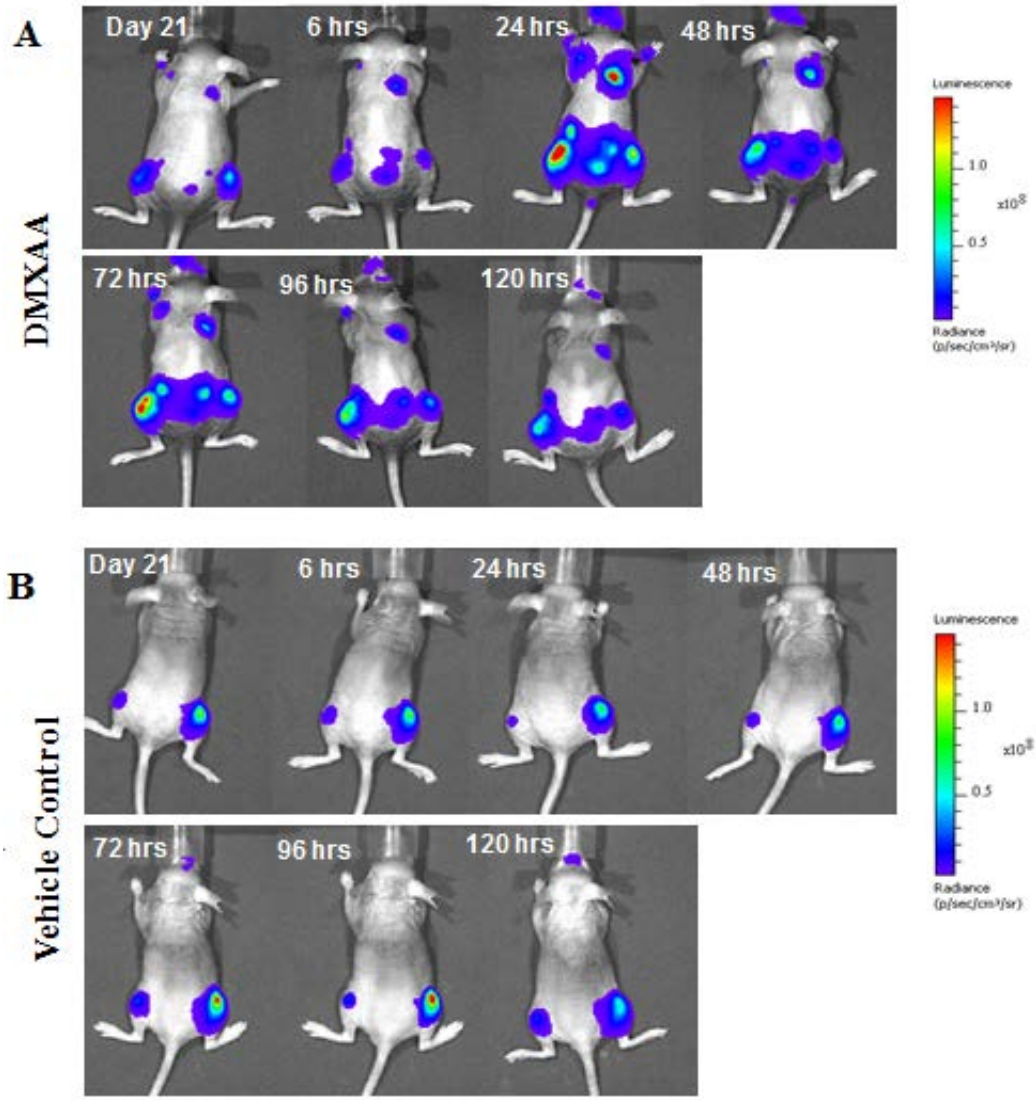

Figure 5.3-1 Measuring tumour growth *in vivo* using bioluminescence imaging.

Bone metastases were generated via intracardiac injection of the MDA-MB-231/EGFP-Luc2cells. Mice were then treated with a one-time DMXAA or vehicle control on day 21, and BLI measured from 6-120 hrs post-treatment. A representative dorsal image of a DMXAA treated mouse (A) and a vehicle control treated mouse (B) are shown starting from day 21 post interacardiac injection, until 120 hrs post-drug treatment. Scales are in photon /s /cm^2. Whole-body bioluminescence, a measure of tumour burden, is presented in this image to show the location of the tumours and the growth rate for both DMXAA treated and vehicle control mice.

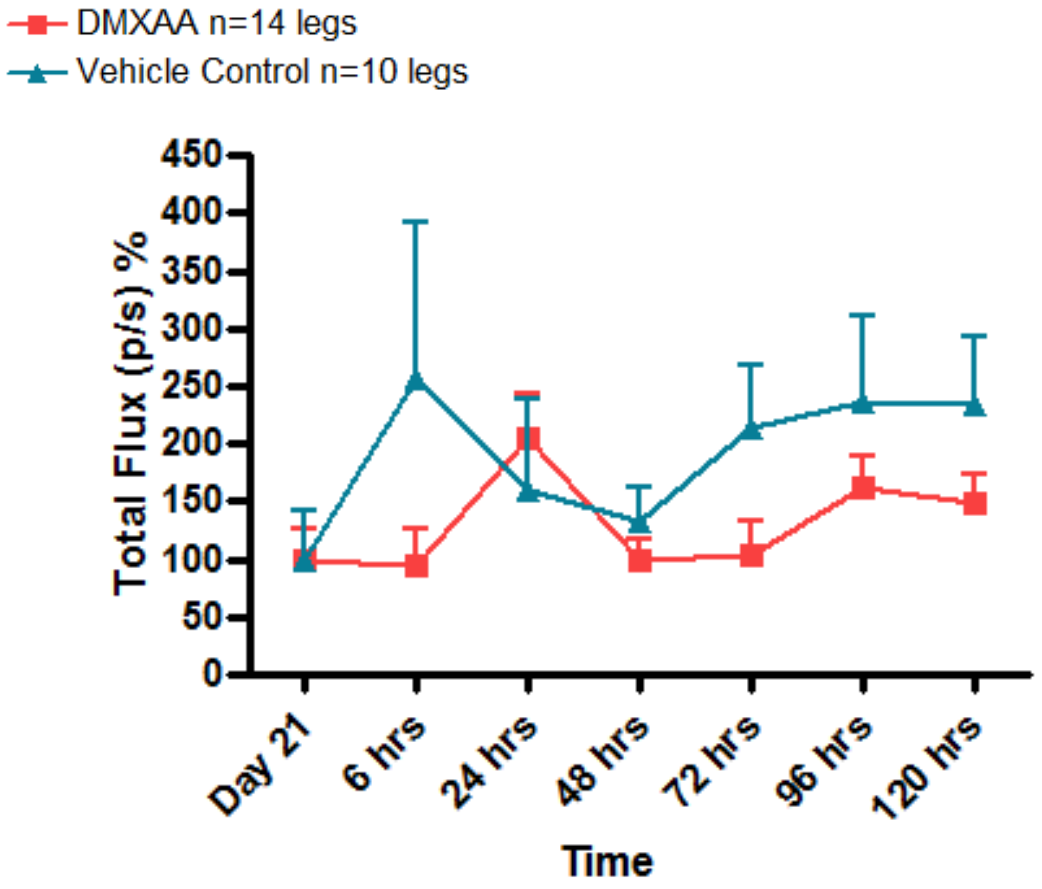

Figure 5.3-2 Quantifying knee bioluminescence intensities of DMXAA treated and vehicle control mice.

Bioluminescence intensity of the knee from DMXAA and vehicle treated mice measured from day 21 post interacardiac injection and up to 120 hrs post-drug treatment. To measure knee bioluminescence, a region of interest (ROI) with a width of 25 (pix) and a height of 25 (pix) was selected in the ventral position. Knee bioluminescence was quantified as a mean photon/s ± SEM. Error bars represent the bioluminescence intensity of 14 knees (n=14) collected from DMXAA treated mice, and 10 knees (n=10) collected from vehicle control mice. Total flux values representing bioluminescence intensity were baseline corrected and graphed using GraphPad Prism 4.0 Software. Statistical analyses were performed using two-way ANOVA in GraphPad Prism and a value of $P<0.05$ was considered statistically significant.

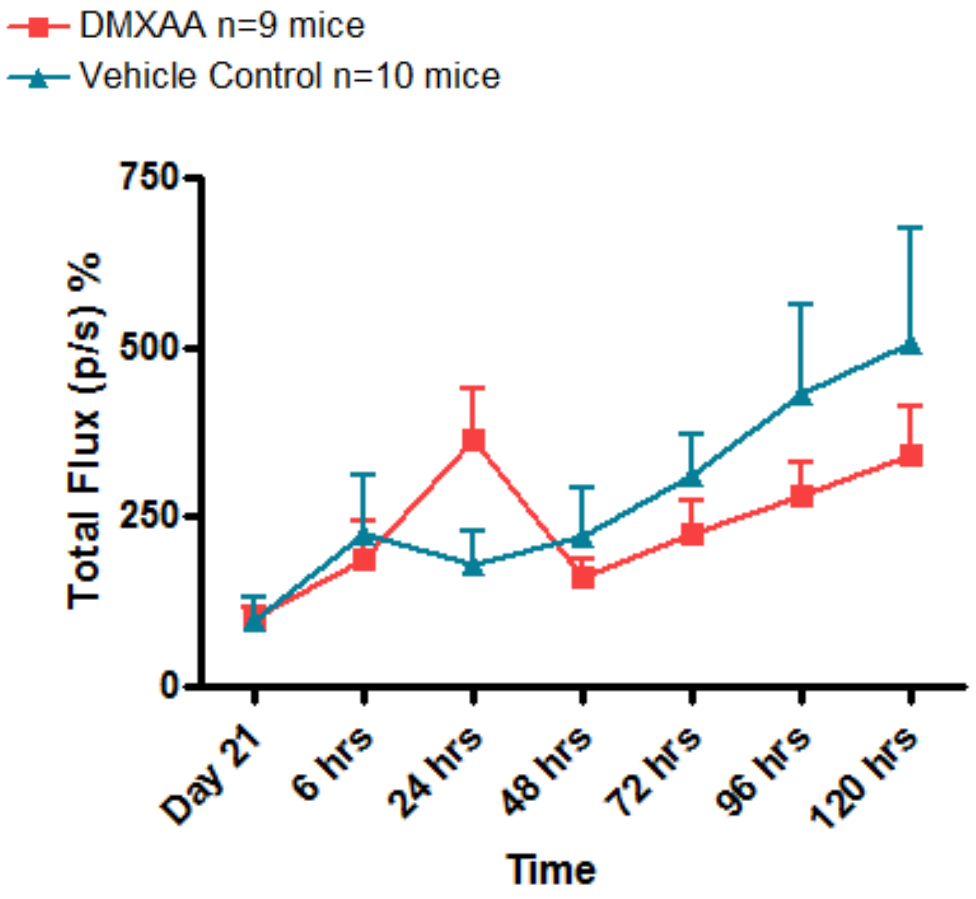

Figure 5.3-3 Quantifying whole-body bioluminescence intensities of DMXAA treated and vehicle control mice.

Whole-body bioluminescence intensities of DMXAA treated and vehicle control mice measured from day 21 post-interacardiac injection up to 120 hrs post-drug treatment. To measure whole body bioluminescence, a region of interest (ROI) with a width of 100 (pix) and a height of 200 (pix) was measured in ventral and dorsal positions. Whole body bioluminescence was quantified as a mean photon/s ± SEM. The error bars represent whole body bioluminescence intensities of 9 DMXAA treated mice (n=9) and 10 vehicle control mice (n=10). Total flux values representing bioluminescence intensities were baseline corrected and graphed using GraphPad Prism 4.0 Software. Statistical analyses were performed using two-way ANOVA in GraphPad Prism and a value of $P<0.05$ was considered statistically significant.

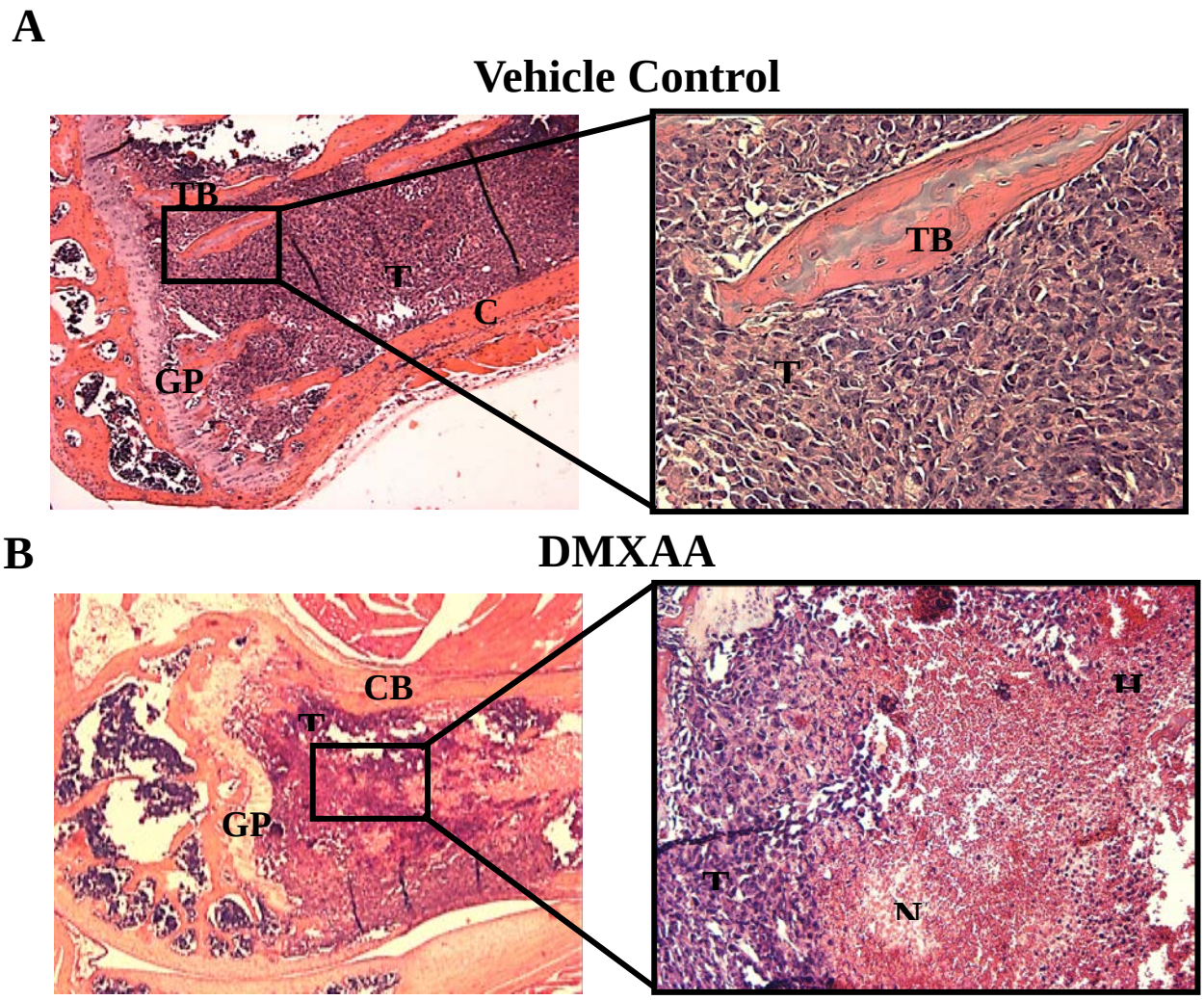

Figure 5.3-4 H&E staining of osteolytic metastases treated with DMXAA or vehicle control at 120 hrs post-drug administration.

Mice with day 21 post MDA-MB-231/EGFP-Luc2 injection osteolytic metastases were treated with a one-time dose DMXAA or vehicle control and sacrificed to collect the limbs for histology. (A & B) H&E stained sections of the limbs from vehicle control and DMXAA treated mice, respectively. Tumour area (T), necrosis (N), hemorrhage (H), growth plate (GP), trabecular bone (TB), cortical bone (CB). Images on the left were taken at 25x magnification, image on the upper right was taken at 200x, and image on the lower right was taken at 100x.

also carried out to study the effects of the combinational treatment on tumour morphology.

5.3.2.1 Measuring tumour growth using bioluminescence imaging

The effect of DMXAA treatment in combination with GDC-0941 on bone metastases was investigated. Mice were divided into two groups: group one was treated with GDC-0941 from day 19-25 along with a one-time dose of DMXAA on day 21; group two was treated with vehicle control from day 19-25. BLI was carried out from 6-120 hrs post-treatment (Fig 5.3-5). Images were collected and quantified for the knees as well as the whole-body to evaluate tumour growth rates. Knee BLI measurements from 6-120 hrs post-treatment for combinational treated mice and vehicle control mice did not show any significant difference (Fig 5.3-6). Whole BLI measurements from 6-120 hrs post-treatment for combinational treated mice and vehicle control mice also did not show any significant difference (Fig 5.3-7). Despite again showing evidence of a downward trend in photon emission rates, combinational treatment did not significantly affect the increase in bioluminescence over time, indicating that the drug combination did not have a major impact on either bone and/or total metastases burden (Fig 5.3-6, 7).

5.3.2.2 Tumour histological analysis

Tumours were visualized in the H&E stain of knee sections from both DMXAA+GDC-0941 treated and vehicle control mice. In the 8 samples analyzed there were regions of necrosis (labelled as N in Fig 5.3-8). Qualitatively, these appeared similar to the necrotic regions observed within the DMXAA alone treated mice at 120 hrs (Fig 5.3-4).

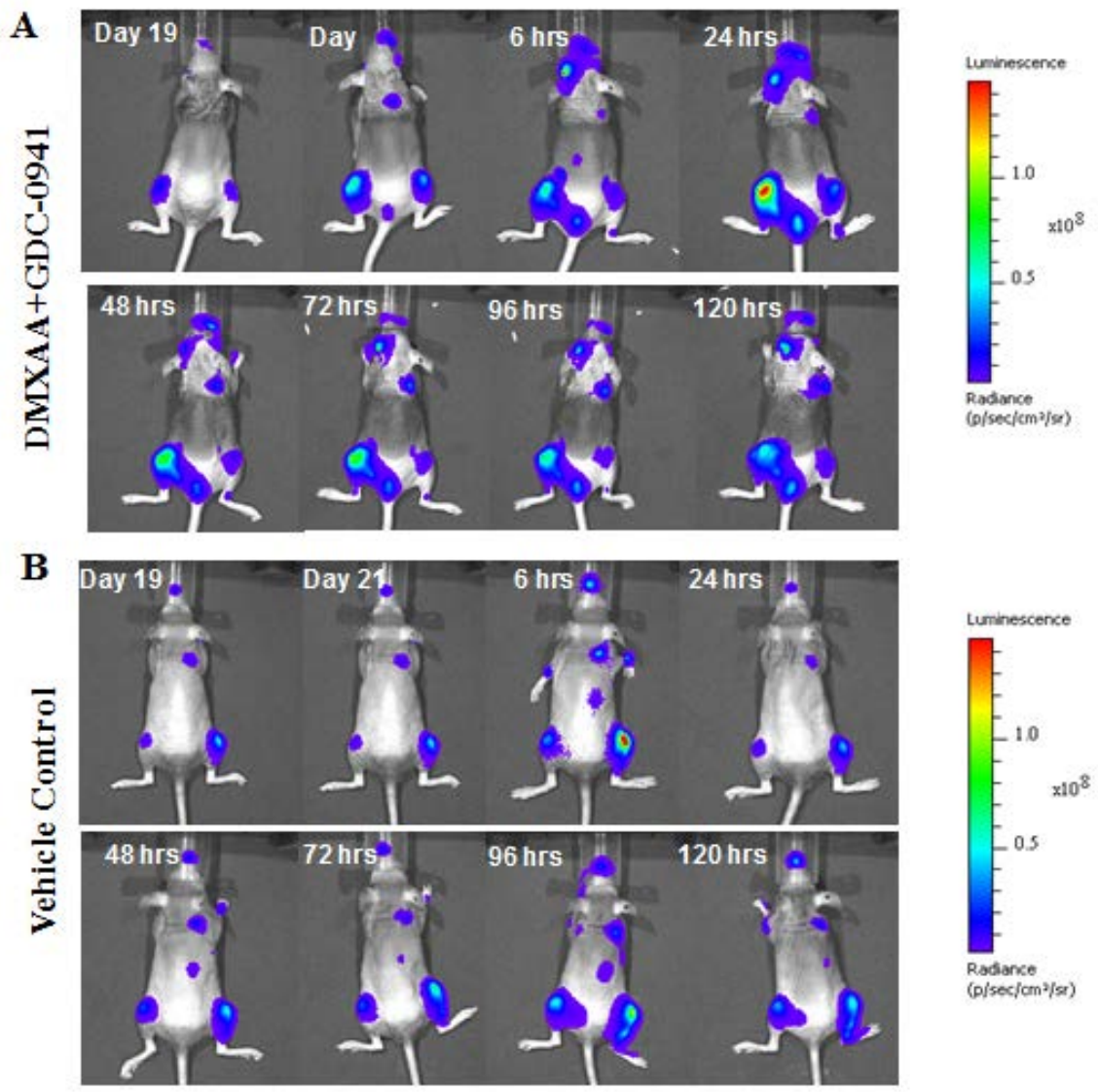

Figure 5.3-5 Measuring tumour growth *in vivo* using bioluminescence imaging.

Bone metastases were generated via intracardiac injection of MDA-MB-231/EGFP-Luc2 cells. Mice were then treated with vehicle control or GDC-0941from day 19-25, and a one-time I.P injection of DMXAA on day 21. A representative dorsal image of a DMXAA and GDC-0941 combinational treated mouse (A) and vehicle control treated mouse (B) starting from day 19 post-interacardiac injection until 120 hrs post-DMXAA treatments. Scales are in photon/s/cm^2. Whole-body luminescence, a measure of tumour burden, shows the location of the tumours and the growth rate for both DMXAA treated and vehicle control mice.

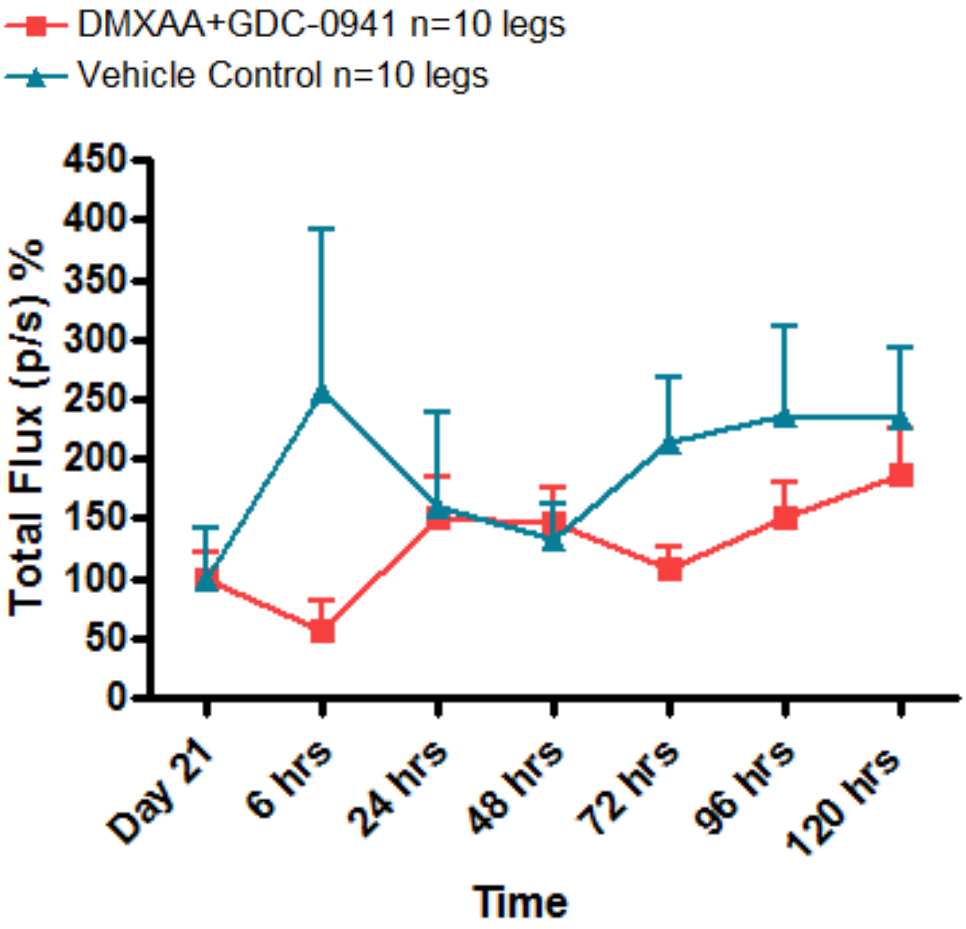

Figure 5.3-6 Quantifying knee bioluminescence intensity of combinational DMXAA+GDC-0941 treated, and vehicle control mice.

Bioluminescence intensity of knees from combinational DMXAA+GDC-0941 and vehicle treated mice measured from day 19 post intracardiac injection and GDC-0941 treatment up to 120 hrs post-DMXAA treatment. To measure knee bioluminescence, a region of interest (ROI) with a width of 25 (pix) and a height of 25 (pix) was selected in the ventral position. Knee bioluminescence was quantified as a mean photon/s ± SEM. Error bars represent bioluminescence intensity of 10 knees (n=10) collected from combinational DMXAA+GDC-0941 treated mice, and 10 knees (n=10) collected from vehicle control mice. Total flux values representing bioluminescence intensity were baseline corrected and graphed using GraphPad Prism 4.0 Software. Statistical analyses were performed using two-way ANOVA in GraphPad Prism and a values of $P<0.05$ was considered statistically significant.

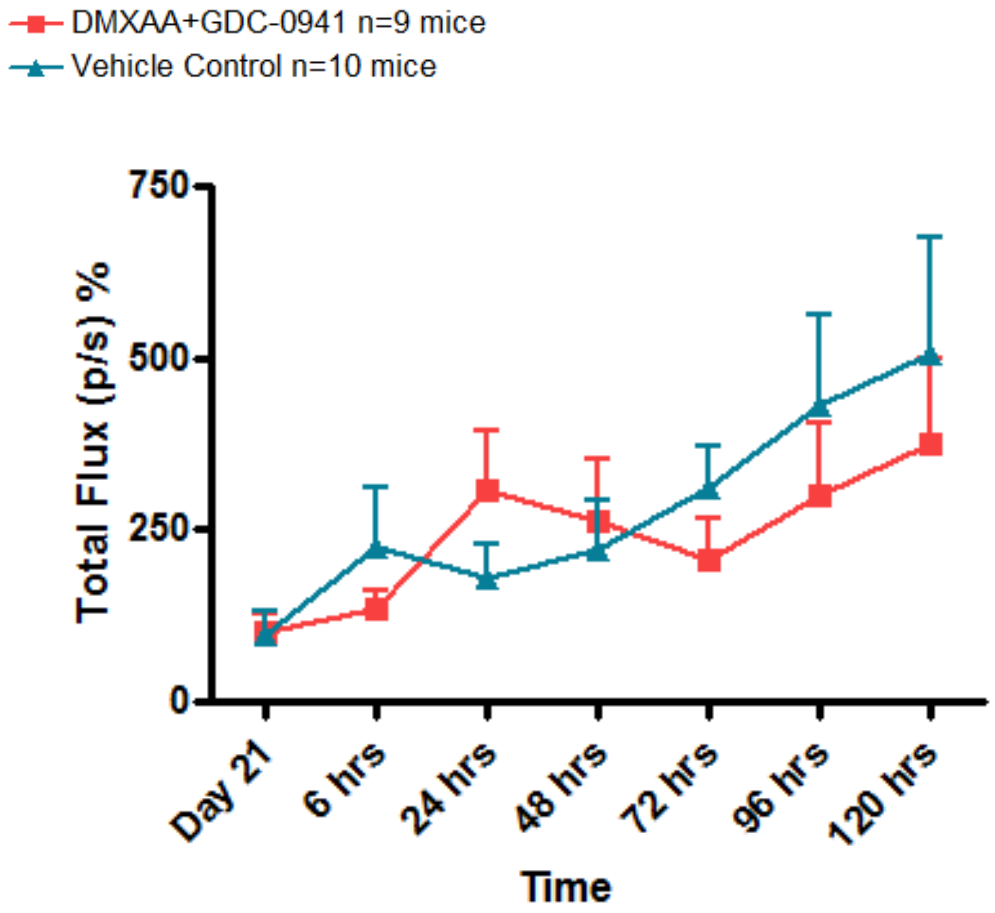

Figure 5.3-7 Quantifying of the whole body bioluminescence intensities of combinational DMXAA+GDC-0941 treated and vehicle control mice.

Whole-body bioluminescence intensities of combinational DMXAA+GDC-0941 treated and vehicle control mice measured from day 19 post-interacardiac injection and GDC-0941 treatment was introduced until 120 hrs post DMXAA treatment. To measure whole body bioluminescence, a region of interest (ROI) with a width of 100 (pix) and a height of 200 (pix) was measured in the ventral and dorsal positions. Whole body bioluminescence was quantified as a mean photon/s ± SEM. The error bars represent whole body bioluminescence intensity of 9 combinational DMXAA+GDC-0941 treated micee (n=9) and 10 vehicle control treated mice (n=10). Total flux values representing bioluminescence intensities were baseline corrected and graphed using GraphPad Prism 4.0 Software. Statistical analyses were performed using two-way ANOVA in GraphPad Prism and a value of $P<0.05$ was considered statistically significant.

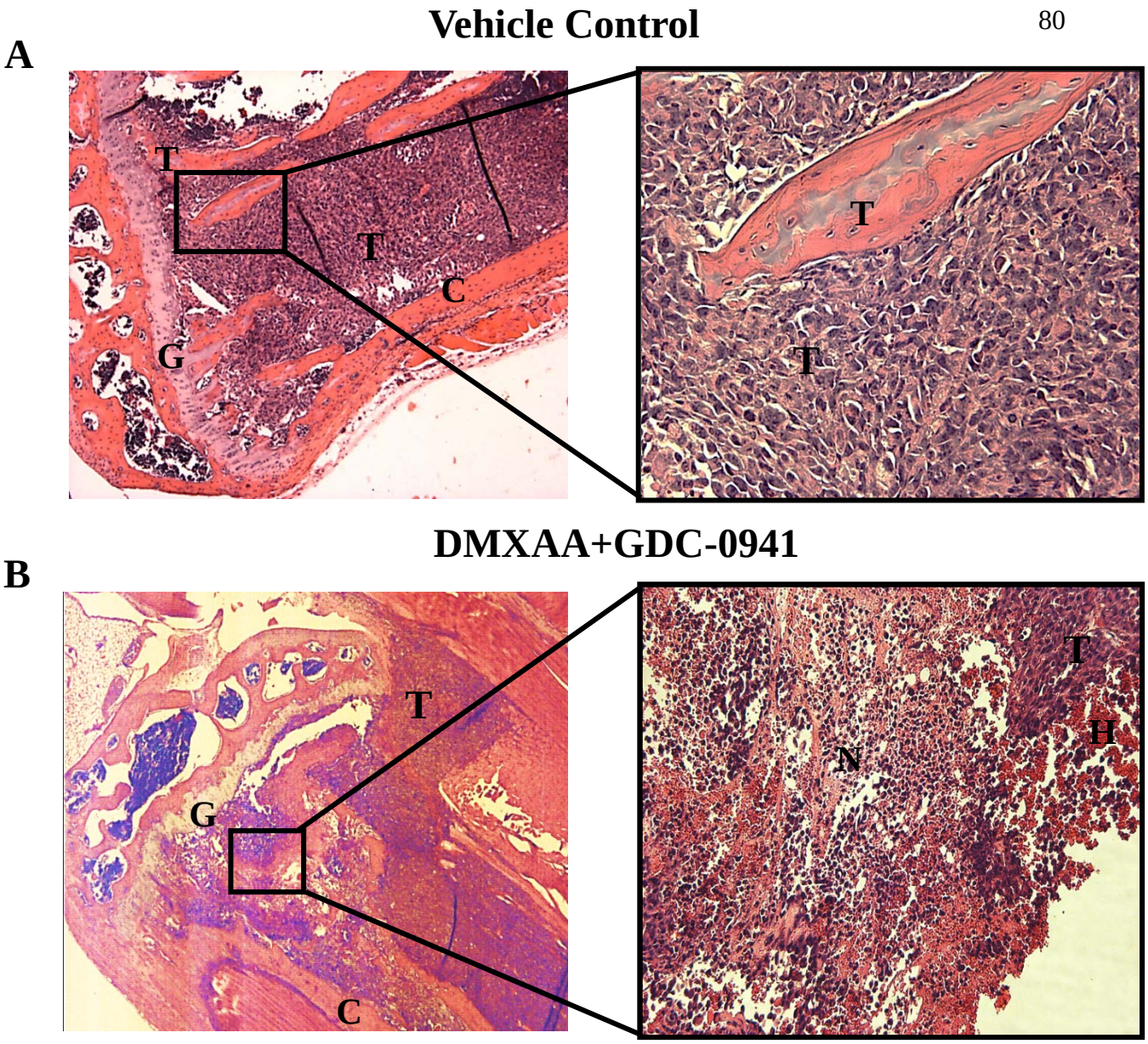

Figure 5.3-8 H&E staining of osteolytic metastases treated with DMXAA+GDC-0941 or vehicle control.

Mice with MDA-MB-231/EGFP-Luc2 derived osteolytic metastases were treated with the combination of DMXAA plus GDC-0941, or vehicle control, and were sacrificed to collect the limbs for histology. (A & B) H&E stained sections of limbs from vehicle control and DMXAA+GDC-0941 treated mice, respectively. Tumour area (T), necrosis (N), hemorrhage (H), growth plate (GP), trabecular bone (TB), cortical bone (CB). Images on the left were taken at 25x magnification, and the image on the upper right was taken at 200x magnification, with the image on the lower right being taken at 100x magnification.

5.4 Discussion

DMXAA has shown promising effects in preclinical *in vivo* studies when evaluating the induction of hemorrhagic necrosis and growth delay [59, 60]. However, contrary to what we expected, DMXAA, either alone, or in combination with GDC-0941, had no statistically significant on bioluminescence of established MDA-MB-231/EGFP-Luc2 metastases. Histological analysis, however, did show evidence of some hemorrhagic necrosis in the bone tumours of mice 120 hrs post-DMXAA treatment when compared to the control. Similar necrosis regions were also evident in DMXAA and GDC-0941 combinational treated mice at 120 hrs. These results may explain that BLI of bone metastases may not be a sensitive way to detect the presence of necrotic regions that are developed after DMXAA treatment. The surviving rim of tumour cells post-DMXAA treatment is responsible for most of the bioluminescence seen. Thus, even though some necrosis does occur within the bone metastases, (and this was seen at 24 hrs) it cannot be detected via BLI likely due to the presence of thick rim of surviving live tumour cells emitting photons. Significant drops in BLI may only occur when only a very thin rim remains, as was the case for DMXAA-treated subcutaneous tumours. Overall, while immediate effects, such as seen in the DMXAA-treated subcutaneous tumours (Chapter 4), were not as marked in the bone metastases, DMXAA was still able to induce some level of central necrosis. Also, the BLI data appeared show a trend in this direction, although result did not achieve statistical significance. BLI did not support the notion that GDC-0941 would be able to enhance the effect of DMXAA on the endothelium. In fact, recent studies have suggested that PI3K inhibition can lead to vessel normalization, an

effect that would, of anything, decrease sensitivity of DMXAA [83]. This is because VDA acts on destabilized vessels.

5.5 Conclusion

The addition of GDC-0941 does not appear to enhance the vascular disrupting effect of DMXAA on bone metastases.

Chapter Six: Conclusions and future directions

6.1 Summary of results

In this study we confirmed that the pan-PI3K inhibitor, GDC-0941, does not have the potential to either prevent the growth MDA-MB-231/EGFP-Luc2 induced osteolytic metastases or to limit bone damage. Indeed GDC-0941 had no effect on MDA-MB-231/EGFP-Luc2 cell *in vitro* proliferation or viability, and if anything, led to a worsening of bone destruction in response to metastases (Chapter 3). We felt that this data, as preliminary as it was, convincing enough for us to conclude that inhibiting the PI3K pathway did not have a beneficial therapeutic effect on bone metastases derived from the intra-cardiac injection of MDA-MB-231/EGFP-Luc2 breast cancer cells.

DMXAA had promising effects in preclinical *in vivo* studies as shown by its ability to induce hemorrhagic necrosis and growth delay in various tumour types tumours [59, 60]. In contrast, DMXAA did not exhibit a pronounced effect on MDA-MB-231/EGFP-Luc2 breast cancer cell line-induced osteolytic metastases when compared with subcutaneous tumours, as was clearly evident by BLI (Chapter 4). Histological examination of subcutaneous tumours post-DMXAA treatment also confirmed that the subcutaneous tumours had undergone massive necrosis similar to that previously reported in the literature [58, 79]. However, hemorrhagic necrosis seen upon H&E staining of osteolytic metastases after DMXAA treatment was not nearly as dramatic as was seen in subcutaneous tumours.

Contrary to what we hypothesized, DMXAA, either alone or in combination with GDC-0941 had no statistically significant effect on the growth rate of either bone or total body metastases (Chapter 5). Specifically, BLI did not support the notion that GDC-0941 would be able to enhance the effect of DMXAA on the endothelium. Histological analysis, however, revealed that DMXAA treated knee metastases did exhibited limited variable and level of hemorrhagic necrosis.

6.2 Conclusions and future experiments

The PI3K inhibitor, GDC-0941, had no effect on MDA-MB-231/EGFP-Luc2-derived bone metastases. This may be due to the presence of a parallel signalling pathway in which mammalian target of rapamycin complex 2 (mTORC2) might be able to counteract the therapeutic efficacy of GDC-0941 (Fig 6.2-1). It is known that the mammalian target of rapamycin (mTOR) and PI3K signalling pathways are subjected to complex crosstalk and feedback interactions in both cancer and normal cells [84]. mTOR exists in two different complex known as mTORC1 and mTORC2 [85]. As part of mTORC2 complexes, mTOR is also known to activate AKT, a protein kinase located downstream of the PI3K pathway, that is involved regulating cell growth, motility, survival and metabolism [86, 87]. Thus, dual targeting of PI3K and mTORC2 may be advantageous. Future experiments could consist of evaluating the effect of dual PI3K/mTORC2 inhibition on the growth of osteolytic metastases. Currently, there are several mTOR inhibitors (such as the ATP binding site competitive inhibitor, OSI-027, INK128, and AZD8055), or dual PI3K/mTOR inhibitors (such as NVP-BEZ235, GDC-0980 and

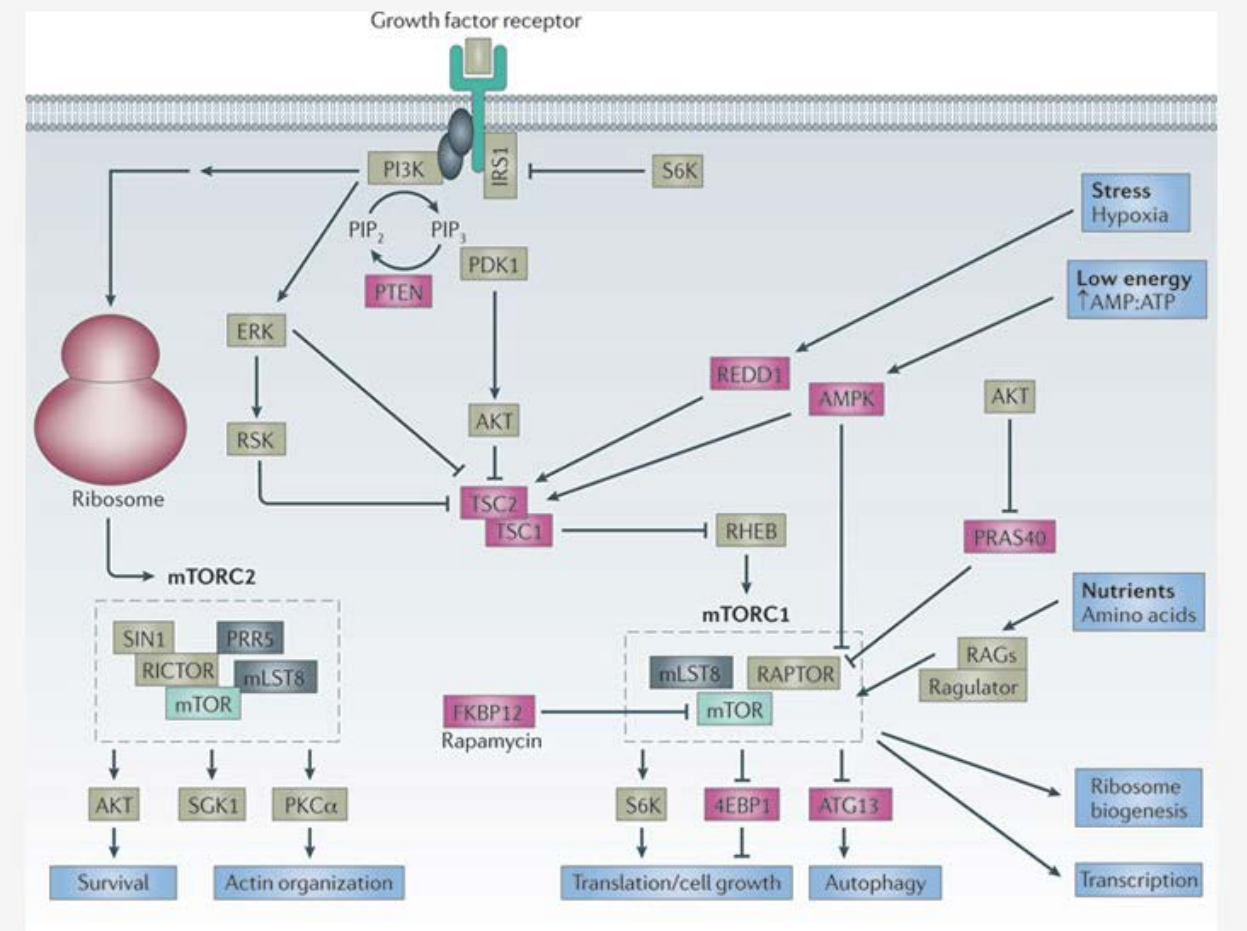

Figure 6.2-1 Signalling cascade downstream of PI3K.

This figure was printed from (Benjamin D, Colombi M, Moroni C, Hall MN, 2011), with permission from Nature Review Drug Discovery.

XL675) available for cancer therapy [84, 85, 88]. Some of these inhibitors are in clinical trials. The mTOR inhibitor, AZD8055, for example, is currently in phase I clinical trials for solid tumours and advanced solid malignancies (clinicaltrails.gov). The dual PI3K/mTOR inhibitor GDC-0980 and XL675 are both in several phase I clinical trials [84], and the dual PI3K/mTOR (mTORC1) inhibitor NVP-BEZ235 is currently in several Phase I/II clinical trials for advanced metastatic breast cancer [89]. Future experiments might include studying the effect of GDC-0941 with AZD8055 (an mTORC2 inhibitor), or the dual PI3K/mTOR inhibitor NVP-BEZ235 on the growth of osteolytic metastases. In addition, we could also study effect of GDC-0941 with RANKL inhibitor since this protein primarily derives osteoclast differentiation from osteoclast-precursors, and activates and prolongs the survival of mature osteoclasts [90]. Denosumab is a RANKL inhibitor that is currently in phase II clinical trials for bone tumours [90]. In future experiments, it would be of interest to evaluate the effect of combining GDC-0941 with Denosumab to see what effect this might have on tumour osteolysis. We expect that dual inhibition of osteoclast activity and survival through inhibition of PI3K and RANKL would decrease osteolytic mediated damage by these cells.

While DMXX-treated MDA-MB-231/EGFP-Luc2 osteolytic tumours responded poorly to DMXAA, subcutaneous tumours derived from these cells demonstrated a profound response to this drug. What features of the two tumours sites might account for this differential response? There are number of potential possibilities: For example, the type of vasculature present in the subcutaneous tumours verses metastases might differ. Thus, osteolytic metastases may be resistant to DMXAA treatment owing to a greater degree of

vessel stabilization. DMXAA targets the tumour vasculature owing to the distinctive properties of the latter, such as a disorganized structure, increased vascular permeability and intermittent blood flow, as compared to normal vasculature [48, 63]. Thus, tumours with a greater degree of vessel stabilization may not exhibit the distinctive properties needed for targeting by DMXAA. Secondly, the vasculature of different tissues may have different capacities to respond to angiogenic signals. Dermal vessels may differ from bone metastases vessels. Furthermore, the region below the growth plate, the site of tumour cell growth in bone, is already an area of active normal angiogenesis and these vessels may be relatively resistant to DMXAA. Thirdly, bone metastases start with only one or few cells and hence develop slowly, allowing angiogenesis to keep pace with tumour growth. On the other hand, subcutaneous tumours start with a very much larger number of cells and their rapid growth may outstrip the tissue's ability to provide vessels. This may lead to ischemia as a result of inadequate and unstable vessels that are readily targeted by DMXAA. It is also possible that subcutaneous tumours have higher concentrations of activated macrophages as compared to osteolytic metastases. This might be predicted because the major contributor of the "indirect effect" of DMXAA appears to be TNF-± mediated, whereby TNF-± is released by activated macrophages [63]. Thus, if increased levels of macrophages were a feature of subcutaneous tumours, as compared to osteolytic metastases, it would explain why the former show so much better responses to DMXAA. Lastly, the presence of regions of ischaemia and necrosis that are typically seen in MDA-MB-231/EGFP-Luc2 subcutaneous tumours, but not in osteolytic metastases, may have played a role in the differential response to DMXAA. Ischaemia and necrosis are associated with the elevated release of damage associated molecular

pattern molecules (DAMPs), such as the high mobility group protein B1 (HMGB1) [91]. Via stimulation of Toll-like receptor 4 (TLR4), HMGB1 has been shown to activate macrophages to release cytokines such as TNF-± [91]. Thus, subcutaneous tumours, that already show region of necrosis, and hence ischemia, may have much higher levels of activated macrophages capable of releasing TNF-± in response to DMXAA. In contrast, the osteolytic metastases, which lack areas of necrosis, are less responsive to DMXAA treatment. These are some potential avenues further investigation will be required.

To look at tumour-associated macrophages in more detail, future experiments include doing ionized calcium binding adaptor molecule 1 (Iba1) immunohistochemistry for both subcutaneous tumours and osteolytic metastases. Iba1 is a calcium-binding protein specific to macrophages/microglia that is involved in membrane ruffling and phagocytosis [92]. Iba1 immunohistochemistry would allow us to determine whether the level of the macrophages present in the tumour might account for the conflicting responses to DMXAA. It would also be important to find out what types of macrophages are predominantly present in subcutaneous tumours versus the osteolytic metastases. This is because M1 macrophages are the main producers of TNF-± and nitric oxide (NO) which mediates the “indirect effects” of DMXAA [93]. We could evaluate this by immunohistochemistry using antibodies against inducible nitric oxide synthase (iNOS), and arginase-1, to identify M1, and M2 macrophages, respectively. As an additional experiment it would be of interest to do immunohistochemistry using an antibody against HMGB1 to determine whether this molecule is present in the interstitial spaces within necrotic regions. It would also be of interest to examine RNA from both subcutaneous

tumours and osteolytic metastases by real time reverse transcriptase-polymerase chain reaction (PCR) to directly examine TNF-± transcript levels in both types of tumours before and after DMXAA treatment.

Overall, these studies could give us potential insight into the differences in the vascular environments between subcutaneous and metastatic tumours. There is a need for further investigation as to why osteolytic metastases respond more poorly to DMXAA as compared to subcutaneous tumours. This is important especially in view of the poor results obtained in the human clinical trials with DMXAA [94].

Reference

1. Jemal, A., et al., *Global cancer statistics.* CA Cancer J Clin, 2011. **61**(2): p. 69-90.
2. Hammer, C., A. Fanning, and J. Crowe, *Overview of breast cancer staging and surgical treatment options.* Cleve Clin J Med, 2008. **75 Suppl 1**: p. S10-6.
3. Sorlie, T., et al., *Repeated observation of breast tumor subtypes in independent gene expression data sets.* Proc Natl Acad Sci U S A, 2003. **100**(14): p. 8418-23.
4. Bartlett, J.M., et al., *Estrogen receptor and progesterone receptor as predictive biomarkers of response to endocrine therapy: a prospectively powered pathology study in the Tamoxifen and Exemestane Adjuvant Multinational trial.* J Clin Oncol, 2011. **29**(12): p. 1531-8.
5. Perou, C.M., et al., *Molecular portraits of human breast tumours.* Nature, 2000. **406**(6797): p. 747-52.
6. Bertos, N.R. and M. Park, *Breast cancer - one term, many entities?* J Clin Invest, 2011. **121**(10): p. 3789-96.
7. Calza, S., et al., *Intrinsic molecular signature of breast cancer in a population-based cohort of 412 patients.* Breast Cancer Res, 2006. **8**(4): p. R34.
8. Turner, N.C. and J.S. Reis-Filho, *Basal-like breast cancer and the BRCA1 phenotype.* Oncogene, 2006. **25**(43): p. 5846-53.
9. Dawood, S., et al., *Defining breast cancer prognosis based on molecular phenotypes: results from a large cohort study.* Breast Cancer Res Treat, 2011. **126**(1): p. 185-92.
10. Hannemann, J., et al., *Changes in gene expression associated with response to neoadjuvant chemotherapy in breast cancer.* J Clin Oncol, 2005. **23**(15): p. 3331-42.
11. Fost, C., et al., *Targeted chemotherapy for triple-negative breast cancers via LHRH receptor.* Oncol Rep, 2011. **25**(5): p. 1481-7.
12. Anders, C. and L.A. Carey, *Understanding and treating triple-negative breast cancer.* Oncology (Williston Park), 2008. **22**(11): p. 1233-9; discussion 1239-40, 1243.
13. Constantinidou, A., R.L. Jones, and J.S. Reis-Filho, *Beyond triple-negative breast cancer: the need to define new subtypes.* Expert Rev Anticancer Ther, 2010. **10**(8): p. 1197-213.
14. Minn, A.J., et al., *Distinct organ-specific metastatic potential of individual breast cancer cells and primary tumors.* J Clin Invest, 2005. **115**(1): p. 44-55.
15. Rove, K.O. and E.D. Crawford, *Evolution of treatment options for patients with CRPC and bone metastases: bone-targeted agents that go beyond palliation of symptoms to improve overall survival.* Oncology (Williston Park), 2011. **25**(14): p. 1362-70, 1375-81, 1387.
16. Kingsley, L.A., et al., *Molecular biology of bone metastasis.* Mol Cancer Ther, 2007. **6**(10): p. 2609-17.
17. Coleman, R.E., *Skeletal complications of malignancy.* Cancer, 1997. **80**(8 Suppl): p. 1588-94.

18. Mundy, G.R., *Metastasis to bone: causes, consequences and therapeutic opportunities.* Nat Rev Cancer, 2002. **2**(8): p. 584-93.
19. Ford, J.A., G. Mowatt, and R. Jones, *Assessing pharmacological interventions for bone metastases: the need for more patient-centered outcomes.* Expert Rev Clin Pharmacol, 2012. **5**(3): p. 271-9.
20. Figueroa-Magalhaes, M.C. and R.S. Miller, *Bone-modifying agents as adjuvant therapy for early-stage breast cancer.* Oncology (Williston Park), 2012. **26**(10): p. 955-62.
21. Lerner, U.H., *Bone remodeling in post-menopausal osteoporosis.* J Dent Res, 2006. **85**(7): p. 584-95.
22. Chen, Y.C., D.M. Sosnoski, and A.M. Mastro, *Breast cancer metastasis to the bone: mechanisms of bone loss.* Breast Cancer Res, 2010. **12**(6): p. 215.
23. Theriault, R.L. and R.L. Theriault, *Biology of bone metastases.* Cancer Control, 2012. **19**(2): p. 92-101.
24. Novack, D.V. and S.L. Teitelbaum, *The osteoclast: friend or foe?* Annu Rev Pathol, 2008. **3**: p. 457-84.
25. Insogna, K.L., et al., *Colony-stimulating factor-1 induces cytoskeletal reorganization and c-src-dependent tyrosine phosphorylation of selected cellular proteins in rodent osteoclasts.* J Clin Invest, 1997. **100**(10): p. 2476-85.
26. Teitelbaum, S.L. and F.P. Ross, *Genetic regulation of osteoclast development and function.* Nat Rev Genet, 2003. **4**(8): p. 638-49.
27. Suva, L.J., et al., *Bone metastasis: mechanisms and therapeutic opportunities.* Nat Rev Endocrinol, 2011. **7**(4): p. 208-18.
28. Asagiri, M. and H. Takayanagi, *The molecular understanding of osteoclast differentiation.* Bone, 2007. **40**(2): p. 251-64.
29. Laurino, L., et al., *PI3K activation by IGF-1 is essential for the regulation of membrane expansion at the nerve growth cone.* J Cell Sci, 2005. **118**(Pt 16): p. 3653-62.
30. Huang, Y., et al., *Activation of the PI3K/AKT pathway mediates FSH-stimulated VEGF expression in ovarian serous cystadenocarcinoma.* Cell Res, 2008. **18**(7): p. 780-91.
31. Lappano, R. and M. Maggiolini, *G protein-coupled receptors: novel targets for drug discovery in cancer.* Nat Rev Drug Discov, 2011. **10**(1): p. 47-60.
32. Yang, L., et al., *Interleukin-6 differentially regulates androgen receptor transactivation via PI3K-Akt, STAT3, and MAPK, three distinct signal pathways in prostate cancer cells.* Biochem Biophys Res Commun, 2003. **305**(3): p. 462-9.
33. Salphati, L., et al., *Pharmacokinetic-pharmacodynamic modeling of tumor growth inhibition and biomarker modulation by the novel phosphatidylinositol 3-kinase inhibitor GDC-0941.* Drug Metab Dispos, 2010. **38**(9): p. 1436-42.
34. Wymann, M.P., M. Zvelebil, and M. Laffargue, *Phosphoinositide 3-kinase signalling--which way to target?* Trends Pharmacol Sci, 2003. **24**(7): p. 366-76.
35. Zhao, L. and P.K. Vogt, *Class I PI3K in oncogenic cellular transformation.* Oncogene, 2008. **27**(41): p. 5486-96.
36. Bowles, D.W. and A. Jimeno, *New phosphatidylinositol 3-kinase inhibitors for cancer.* Expert Opin Investig Drugs, 2011. **20**(4): p. 507-18.

37. Kong, D., et al., *Inhibition profiles of phosphatidylinositol 3-kinase inhibitors against PI3K superfamily and human cancer cell line panel JFCR39.* Eur J Cancer, 2010. **46**(6): p. 1111-21.
38. Shojaei, F., *Anti-angiogenesis therapy in cancer: current challenges and future perspectives.* Cancer Lett, 2012. **320**(2): p. 130-7.
39. Hanahan, D. and R.A. Weinberg, *Hallmarks of cancer: the next generation.* Cell, 2011. **144**(5): p. 646-74.
40. Bergers, G. and L.E. Benjamin, *Tumorigenesis and the angiogenic switch.* Nat Rev Cancer, 2003. **3**(6): p. 401-10.
41. Konno, H., M. Yamamoto, and M. Ohta, *Recent concepts of antiangiogenic therapy.* Surg Today, 2010. **40**(6): p. 494-500.
42. O'Reilly, M.S., et al., *Endostatin: an endogenous inhibitor of angiogenesis and tumor growth.* Cell, 1997. **88**(2): p. 277-85.
43. Jain, R.K., *Normalization of tumor vasculature: an emerging concept in antiangiogenic therapy.* Science, 2005. **307**(5706): p. 58-62.
44. Ribatti, D., et al., *The history of the angiogenic switch concept.* Leukemia, 2007. **21**(1): p. 44-52.
45. Mabuchi, S., et al., *Maintenance treatment with bevacizumab prolongs survival in an in vivo ovarian cancer model.* Clin Cancer Res, 2008. **14**(23): p. 7781-9.
46. Vosseler, S., et al., *Angiogenesis inhibition by vascular endothelial growth factor receptor-2 blockade reduces stromal matrix metalloproteinase expression, normalizes stromal tissue, and reverts epithelial tumor phenotype in surface heterotransplants.* Cancer Res, 2005. **65**(4): p. 1294-305.
47. Rini, B.I. and E.J. Small, *Biology and clinical development of vascular endothelial growth factor-targeted therapy in renal cell carcinoma.* J Clin Oncol, 2005. **23**(5): p. 1028-43.
48. McKeage, M.J. and B.C. Baguley, *Disrupting established tumor blood vessels: an emerging therapeutic strategy for cancer.* Cancer, 2010. **116**(8): p. 1859-71.
49. Hicklin, D.J. and L.M. Ellis, *Role of the vascular endothelial growth factor pathway in tumor growth and angiogenesis.* J Clin Oncol, 2005. **23**(5): p. 1011-27.
50. Ellis, L.M. and D.J. Hicklin, *VEGF-targeted therapy: mechanisms of anti-tumour activity.* Nat Rev Cancer, 2008. **8**(8): p. 579-91.
51. Jiang, B.H. and L.Z. Liu, *PI3K/PTEN signaling in angiogenesis and tumorigenesis.* Adv Cancer Res, 2009. **102**: p. 19-65.
52. Ebos, J.M. and R.S. Kerbel, *Antiangiogenic therapy: impact on invasion, disease progression, and metastasis.* Nat Rev Clin Oncol, 2011. **8**(4): p. 210-21.
53. McKeage, M.J., *Clinical trials of vascular disrupting agents in advanced non--small-cell lung cancer.* Clin Lung Cancer, 2011. **12**(3): p. 143-7.
54. Gridelli, C., et al., *Vascular disrupting agents: a novel mechanism of action in the battle against non-small cell lung cancer.* Oncologist, 2009. **14**(6): p. 612-20.
55. Tozer, G.M., C. Kanthou, and B.C. Baguley, *Disrupting tumour blood vessels.* Nat Rev Cancer, 2005. **5**(6): p. 423-35.

56. Hande, K.R., et al., *The pharmacokinetics and safety of ABT-751, a novel, orally bioavailable sulfonamide antimitotic agent: results of a phase 1 study.* Clin Cancer Res, 2006. **12**(9): p. 2834-40.
57. Bertelsen, L.B., et al., *Vascular effects of plinabulin (NPI-2358) and the influence on tumour response when given alone or combined with radiation.* Int J Radiat Biol, 2011. **87**(11): p. 1126-34.
58. Lorusso, P.M., S.A. Boerner, and S. Hunsberger, *Clinical development of vascular disrupting agents: what lessons can we learn from ASA404?* J Clin Oncol, 2011. **29**(22): p. 2952-5.
59. Ching, L.M., W.R. Joseph, and B.C. Baguley, *Antitumour responses to flavone-8-acetic acid and 5,6-dimethylxanthenone-4-acetic acid in immune deficient mice.* Br J Cancer, 1992. **66**(1): p. 128-30.
60. Seshadri, M. and K. Toth, *Acute vascular disruption by 5,6-dimethylxanthenone-4-acetic Acid in an orthotopic model of human head and neck cancer.* Transl Oncol, 2009. **2**(3): p. 121-7.
61. Siemann, D.W., et al., *Vascular targeting agents enhance chemotherapeutic agent activities in solid tumor therapy.* Int J Cancer, 2002. **99**(1): p. 1-6.
62. Chung, F., et al., *Consequences of increased vascular permeability induced by treatment of mice with 5,6-dimethylxanthenone-4-acetic acid (DMXAA) and thalidomide.* Cancer Chemother Pharmacol, 2008. **61**(3): p. 497-502.
63. Jameson, M.B. and M. Head, *Pharmacokinetic evaluation of vadimezan (ASA404, 5,6-dimethylxanthenone-4-acetic acid, DMXAA).* Expert Opin Drug Metab Toxicol, 2011. **7**(10): p. 1315-26.
64. Jassar, A.S., et al., *Activation of tumor-associated macrophages by the vascular disrupting agent 5,6-dimethylxanthenone-4-acetic acid induces an effective CD8+ T-cell-mediated antitumor immune response in murine models of lung cancer and mesothelioma.* Cancer Res, 2005. **65**(24): p. 11752-61.
65. Roberts, Z.J., L.M. Ching, and S.N. Vogel, *IFN-beta-dependent inhibition of tumor growth by the vascular disrupting agent 5,6-dimethylxanthenone-4-acetic acid (DMXAA).* J Interferon Cytokine Res, 2008. **28**(3): p. 133-9.
66. Cao, Z., B.C. Baguley, and L.M. Ching, *Interferon-inducible protein 10 induction and inhibition of angiogenesis in vivo by the antitumor agent 5,6-dimethylxanthenone-4-acetic acid (DMXAA).* Cancer Res, 2001. **61**(4): p. 1517-21.
67. Baguley, B.C. and D.W. Siemann, *Temporal aspects of the action of ASA404 (vadimezan; DMXAA).* Expert Opin Investig Drugs, 2010. **19**(11): p. 1413-25.
68. Zhao, L., et al., *Mechanisms of tumor vascular shutdown induced by 5,6-dimethylxanthenone-4-acetic acid (DMXAA): Increased tumor vascular permeability.* Int J Cancer, 2005. **116**(2): p. 322-6.
69. Watts, M.E., S. Arnold, and D.J. Chaplin, *Changes in coagulation and permeability properties of human endothelial cells in vitro induced by TNF-alpha or 5,6 MeXAA.* Br J Cancer Suppl, 1996. **27**: p. S164-7.
70. Seshadri, M., et al., *Activity of the vascular-disrupting agent 5,6-dimethylxanthenone-4-acetic acid against human head and neck carcinoma xenografts.* Neoplasia, 2006. **8**(7): p. 534-42.

71. Bondareva, A., et al., *The lysyl oxidase inhibitor, beta-aminopropionitrile, diminishes the metastatic colonization potential of circulating breast cancer cells.* PLoS One, 2009. **4**(5): p. e5620.
72. Zheng, X., et al., *ADAM17 promotes breast cancer cell malignant phenotype through EGFR-PI3K-AKT activation.* Cancer Biol Ther, 2009. **8**(11): p. 1045-54.
73. Grey, A., et al., *Evidence for a role for the p110-alpha isoform of PI3K in skeletal function.* Biochem Biophys Res Commun, 2010. **391**(1): p. 564-9.
74. Pilkington, M.F., S.M. Sims, and S.J. Dixon, *Wortmannin inhibits spreading and chemotaxis of rat osteoclasts in vitro.* J Bone Miner Res, 1998. **13**(4): p. 688-94.
75. Gingery, A., et al., *Phosphatidylinositol 3-kinase coordinately activates the MEK/ERK and AKT/NFkappaB pathways to maintain osteoclast survival.* J Cell Biochem, 2003. **89**(1): p. 165-79.
76. Bartholomeusz, C. and A.M. Gonzalez-Angulo, *Targeting the PI3K signaling pathway in cancer therapy.* Expert Opin Ther Targets, 2012. **16**(1): p. 121-30.
77. Torbett, N.E., et al., *A chemical screen in diverse breast cancer cell lines reveals genetic enhancers and suppressors of sensitivity to PI3K isoform-selective inhibition.* Biochem J, 2008. **415**(1): p. 97-110.
78. Papakonstanti, E.A., A.J. Ridley, and B. Vanhaesebroeck, *The p110delta isoform of PI 3-kinase negatively controls RhoA and PTEN.* EMBO J, 2007. **26**(13): p. 3050-61.
79. Lara, P.N., Jr., et al., *Randomized phase III placebo-controlled trial of carboplatin and paclitaxel with or without the vascular disrupting agent vadimezan (ASA404) in advanced non-small-cell lung cancer.* J Clin Oncol, 2011. **29**(22): p. 2965-71.
80. Laws, A.L., et al., *Preclinical in vitro and in vivo activity of 5,6-dimethylxanthenone-4-acetic acid.* Br J Cancer, 1995. **71**(6): p. 1204-9.
81. Seshadri, M. and M.J. Ciesielski, *MRI-based characterization of vascular disruption by 5,6-dimethylxanthenone-acetic acid in gliomas.* J Cereb Blood Flow Metab, 2009. **29**(8): p. 1373-82.
82. Zhao, Y.W., et al., *Enhanced antitumor efficacy by blocking activation of the phosphatidylinositol 3-kinase/Akt pathway during anti-angiogenesis therapy.* Cancer Sci, 2011. **102**(8): p. 1469-75.
83. Qayum, N., et al., *Modulation of the tumor microvasculature by phosphoinositide-3 kinase inhibition increases doxorubicin delivery in vivo.* Clin Cancer Res, 2012. **18**(1): p. 161-9.
84. Willems, L., et al., *PI3K and mTOR signaling pathways in cancer: new data on targeted therapies.* Curr Oncol Rep, 2012. **14**(2): p. 129-38.
85. Schenone, S., et al., *ATP-competitive inhibitors of mTOR: an update.* Curr Med Chem, 2011. **18**(20): p. 2995-3014.
86. Carnero, A., *The PKB/AKT pathway in cancer.* Curr Pharm Des, 2010. **16**(1): p. 34-44.
87. Laplante, M. and D.M. Sabatini, *mTOR signaling in growth control and disease.* Cell, 2012. **149**(2): p. 274-93.
88. Courtney, K.D., R.B. Corcoran, and J.A. Engelman, *The PI3K pathway as drug target in human cancer.* J Clin Oncol, 2010. **28**(6): p. 1075-83.

89. Benjamin, D., et al., *Rapamycin passes the torch: a new generation of mTOR inhibitors.* Nat Rev Drug Discov, 2011. **10**(11): p. 868-80.
90. Lacey, D.L., et al., *Bench to bedside: elucidation of the OPG-RANK-RANKL pathway and the development of denosumab.* Nat Rev Drug Discov, 2012. **11**(5): p. 401-19.
91. Andersson, U. and K.J. Tracey, *HMGB1 is a therapeutic target for sterile inflammation and infection.* Annu Rev Immunol, 2011. **29**: p. 139-62.
92. Kanazawa, H., et al., *Macrophage/microglia-specific protein Iba1 enhances membrane ruffling and Rac activation via phospholipase C-gamma -dependent pathway.* J Biol Chem, 2002. **277**(22): p. 20026-32.
93. Mantovani, A., A. Sica, and M. Locati, *New vistas on macrophage differentiation and activation.* Eur J Immunol, 2007. **37**(1): p. 14-6.
94. Ching, L.M., et al., *Induction of endothelial cell apoptosis by the antivascular agent 5,6-Dimethylxanthenone-4-acetic acid.* Br J Cancer, 2002. **86**(12): p. 1937-42.